TiO_2–Carbon Nanotube Hybrids for High Efficiency Photocatalysts

Submitted in partial fulfillment of the requirements for
the degree of
Doctor of Philosophy
in
Materials Science and Engineering

Hang-Ah Park

B.S. Materials Science and Engineering, Sungkyunkwan University
M.S. Graduate School of EEWS, Korea Advanced Institute of Science and Technology

Carnegie Mellon University
Pittsburgh, PA

August 2015

Acknowledgements

I would first like to thank my advisors, Greg S. Rohrer and Mohammad F. Islam, for their guidance and great support during course of my Ph.D. work. I would also like to thank the members of my committee, Paul A. Salvador, P. Chris Pistorius, and Rongchao Jin for their efforts and valuable suggestions in guiding the work presented in this document. I must acknowledge Mr. and Mrs. Dowd for their Dowd-ICES fellowship and the NSF through Grants DMR 0645596 and CMMI 1335417 to support the research in this document.

I would also like to acknowledge the members of my research group, Siyuan Liu, Noey Munprom, Jimmy Glickstein, Li Li, Brian Holt, Yeonjoo Jeong, Kyu Hun Kim, Youngseok Oh, Ilha Lee, Patrick Boyer, Evan Wilson-Drolet, Alan Compbell, Julian Brathwaite, Michelle Tsui, Sarah Robb, Stefanie Baker, Maxwell Li, and Yisi Zhu. I'd like to thank some of the other members, Young Jo Kim, Jiwon Park, Jonghan Kwon, Bongjoon Lee. The staffs of the Materials Science and Engineering Department, Adam Wise, Jason Wolf, and Tom Nuhfer, were helpful in my work.

Most importantly, thank you to my family, Geunho Park, Gyeonghee Lim, and Jongmin Park, for their love, support and encouragement. Also sincerely thank you to Byung Han Rhieu for his unconditional support during writing this thesis.

Hang-Ah Park, Pittsburgh, PA August 2015

ABSTRACT

The goal of the research is to develop highly efficient visible light photocatalysts based on composites of TiO_2 and carbon nanotubes (CNTs). Since TiO_2 is a chemically inert and abundant material with electronic energy levels that are appropriately positioned to split water, it is a promising photocatalyst. However, the large bandgap energy (3.2 eV) and fast electron-hole recombination rate limit its utility. It is important to design materials to overcome these barriers. In this thesis, the focus is on TiO_2-carbon nanotube composites. The thesis is divided into two parts. The first part, including chapters 4 and 5, is on nano-photoelectrochemical cells made of TiO_2-carbon nanotube (CNT)-Pt hybrid materials with spatially separated oxidation and reduction channels. The second part, including chapters 6 and 7, is on TiO_2-single walled carbon nanotube (SWCNT) aerogel composites with high surface area and stable networks.

In the first part, photoelectrochemical cells of TiO_2-CNT-Pt were developed with TiO_2 on the outside of a carbon nanotube and Pt nanoparticles on the inside of the carbon nanotube to spatially separate the oxidation and reduction reactions. The photocatalytic activity, measured via photocatalytic degradation of methylene blue under visible-light, showed significant enhancement compared with pristine TiO_2 and CNTs. The results were attributed to fast charge separation resulting in a reduction in recombination of e-h pairs and to an extension of light absorption from the ultraviolet [1] to the visible region. The spatial separation of the oxidation and reduction reactions was verified by photo-oxidation of MnO_x on the outside of the TiO_2-CNT-Pt and photo-reduction of Ag nanoparticles on the inside of the TiO_2-CNT-Pt. Through this experiment, we established that the oxidation reaction occurred on the outside of the TiO_2-CNT-Pt and the reduction reaction occurred on the inside of the TiO_2-CNT-Pt. The photoelectrochemical performance showed a high photocurrent below 1.23 V versus reversible hydrogen electrode (RHE) under both white and visible-light. The applied bias photon-to current efficiency (ABPE) of TiO_2-CNT-Pt represented 1.45 % efficiency under white-light and 0.83 % under visible-light at 0.8 V versus RHE.

The second part involves the properties of TiO_2 supported on a highly porous network of SWCNT aerogels where SWCNT aerogels are three-dimensional porous networks of mostly individual SWCNTs. The microscopic images showed uniform coating of TiO_2 nanoparticles with an average diameter of 9 nm on the nanotube network. The volume fraction of pristine SWCNT aerogels was ~ 0.006 and increased to ~ 0.01 when coated by TiO_2, which yielded a porosity of ≥ 99 %. The TiO_2-SWCNT aerogels have a bandgap of 2.6 eV, which was narrowed by 0.6 eV compared with pristine TiO_2. TiO_2-SWCNT aerogels were structurally stable and showed a smaller volume change compared with pristine SWCNT aerogels when submerged in water. This is in sharp contrast to the rapid structural degradation that SWCNT aerogels undergo when they come into contact with water, which suggests that TiO_2 improves the structural stability of nanotube networks within the aerogels. Photocatalytic degradation of methylene blue with the TiO_2-SWCNT aerogels showed a degradation rate of 25 μmol/g/h under visible light. The enhanced photocatalytic activity of TiO_2-SWCNT aerogels compared with pristine TiO_2 and SWCNT aerogels was attributed to highly porous networks as well as an efficient transfer of charge carriers between TiO_2-SWCNT hetero-junctions. The high photocatalytic activity of the TiO_2-SWCNT aerogels did not depend on the concentration of methylene blue.

The addition of Pt decreased the activity of the TiO_2-SWCNT aerogels, which suggests that the reactivity of SWCNT aerogels is not limited by the cathodic reaction and these materials may be useful hybrid photocatalysts.

Contents

Chapter 2. Background

2.1 Principles of photocatalysis

2.2 Titanium dioxide (TiO_2) as a photocatalyst

2.3 TiO_2-CNT composites

2.4 Improvement in separation of charge carriers, intermediates, and products

Chapter 3. Experimental overview

Chapter 4. TiO_2-CNT-Pt membrane with Spatially Separated Oxidation and Reduction Channels

4.2 Experimental methods

4.3 Results

Chapter 5. Effect of TiO_2 thickness and bondings between TiO_2 and carbon in TiO_2-CNT hybrids on photocatalytic activity

5.2 Experimental methods

5.4 Results: Effect of bondings between TiO_2 and CNT on photocatalytic activity

Chapter 6. TiO_2-Single walled carbon nanotubes aerogels

6.3 Experimental methods

6.4 Results

Chapter 7. Photocatalytic dye degradation of TiO_2-SWCNT aerogels and Pt loaded aerogels

7.2 Experimental methods

Chapter 8. Conclusions

List of Figures

List of Tables

Chapter 1

Introduction

One of the most pivotal issues today is the limited amount of fossil fuels and environmental pollution resulting from the usage of fossil fuels. Thus, developments in alternative renewable energy are necessary. Among various energy sources, hydrogen energy is an ideal fuel to solve the issues since it can be generated from water and also produces water as a byproduct. To produce hydrogen from water, photocatalytic water splitting is an outstanding method since it needs solar energy and water, which are abundant, renewable, and innocuous [3-6]. Hence, it is important to design a photocatalyst that can generate hydrogen from water efficiently. Moreover, to commercialize photocatalytic water splitting, it is necessary to reduce cost by using abundant materials configured in a simple system.

Among various available photocatalysts, TiO_2 is a promising material due to its appropriate potential to split water, chemical inertness, cost effectiveness, and stability against photo-corrosion. However, TiO_2 has several limitations such as a large bandgap energy (3.2 eV) limiting the amount of light it can absorb [7, 8], a fast electron-hole recombination rate, and a low surface area [8, 9]. To improve the visible light absorption of TiO_2, diverse approaches have been developed such as metal or nonmetal ion doping for band gap narrowing [10]. Since the dopant ions create defect sites that increase the recombination rate of electron-hole pairs and reduce photocatalytic activity [11, 12], non-metal ion doping has been getting attention and is widely investigated to improve photocatalytic activity under visible light [2, 13-17]. Khan et al. [13] investigated photocatalytic water splitting under visible light using carbon doped TiO_2 which was synthesized by combusting Titanium. Zhao et al. [12] synthesized carbon-doped TiO_2 by a solvothermal method and it showed a high surface area and photocatalytic activity under visible light.

Another problem of using a single-phase photocatalyst is that it is hard to separate the generated charge carriers, intermediates, and the products of water splitting. The problem not only accelerates recombination of generated charges, but also the reverse reaction of products [18]. To improve the separation of charge carriers, carbon nanotubes (CNTs) have been getting significant attention as a support material in photocatalysis and photoelectrochemical cells. The major advantage of the CNT-photocatalyst composite is that a Schottky barrier of a semiconductor-metal junction can reduce charge carrier recombination [19]. This opens the possibility of developing an efficient system to separate charge carriers, intermediates, and the product of water splitting using an earth-abundant photocatalyst which is active in visible light.

Here, we developed a new photoelectrochemical cell composed of an abundant photocatalyst that can function under visible light and micro-channels for the separation of the products. As a photoanode, TiO_2 was located outside of a large diameter carbon nanotube that acts as a photosensitizer and separator for TiO_2. Platinum co-catalyst particles were located inside the carbon nanotube to promote the cathodic reaction. Carbon nanotubes separated the reduction and oxidation parts of the water splitting reaction so that a higher yield of products from water can be obtained. To realize the structures, anodic aluminum oxide (AAO) was used as a template. The AAO template is one of the widely used ways to synthesize nanotube structures of various materials with a uniform diameter. By using the template, TiO_2 and carbon nanotube co-axial structures with Pt nanoparticles located on the inside of the tubes could be realized. By using the photochemical cell of TiO_2-CNT-Pt, we improved the visible light activity of TiO_2 through it interaction with the CNTs and showed enhanced photocatalytic and photoelectrochemical activity that results from the separation of charge carriers and products to the spatially separated oxidation and reduction sites.

The other approach to enhance photocatalytic activity of TiO_2 is using single walled carbon nanotubes (SWCNTs). The carbon nanotubes synthesized using the AAO templates are multi-walled nanotubes with large diameters [20], whereas the highly purified SWCNTs used for TiO_2-SWCNT composites have the best available properties with respect to carrier transport and surface area. Even though MWCNTs can be more used for many applications due to availability and low cost [21], SWCNTs have higher surface area [22] and higher conductivity [23], which can result in an enhancement of the photocatalytic activity of TiO_2-carbon hybrid materials. However, SWCNTs are hardly used as support materials for photocatalysts because it is hard to disperse individual SWCNT due to van der Waals attractions [21, 24]. Thus it is necessary to make individually dispersed SWCNT networks so that TiO_2 particles can be dispersed on the carbon nanotubes without aggregation.

To overcome the challenges mentioned above, SWCNT aerogels are used for the photocatalysts. SWCNT aerogels are composed of individual SWCNTs in highly porous networks [25]. By using the SWCNT aerogels-TiO_2 hybrids, enhanced photocatalytic activity can be expected because a large surface area creates many reactive sites and a high conductivity can promote effective charge transfer at the SWCNTs-TiO_2 hetero-junction. Moreover, TiO_2 particles can be synthesized with a small enough size to be loaded on SWCNTs when the particles are confined in the SWCNT aerogel networks. In this work, we first realized deposition of TiO_2 nanoparticles on well-dispersed SWCNTs to synthesize TiO_2-SWCNT hybrids. By depositing TiO_2 on SWCNT aerogels, we were able to successfully incorporate TiO_2 nanoparticles on well-dispersed SWCNTs and to demonstrate enhanced photocatalytic activity with a stable network in water. The TiO_2-SWCNT aerogels absorb more visible light than TiO_2 alone, resulting in efficient photocatalytic dye degradation under visible light.

Chapter 2

Background

2.1 Principles of photocatalysis

2.1.1 Photocatalytic water splitting

The development of renewable and sustainable fuels as alternatives to fossil and nuclear fuels is desirable because of the beneficial impact on the environment. Hydrogen has recently been getting increasing attention as a promising energy carrier. To produce hydrogen, photocatalytic water splitting has been developed since Fujishima and Honda decomposed water into hydrogen and oxygen for the first time by in a photoelectrochemical cell that used titania as a photoanode [26]. Splitting water requires a Gibbs free energy of 1.23 eV. The reaction is represented as follows:

$$2H_2O \rightarrow 2H_2 + O_2 \quad (1)$$

$$2H_2O + 4h^+ \rightarrow O_2 + 4H^+ \quad (2)$$

$$2H^+ + 2e^- \rightarrow H_2 \quad (3)$$

Fujishima and Honda [26] used TiO_2 as a photoanode and a Pt cathode connected by an external circuit to demonstrate photoelectrochemical water splitting. Under UV light irradiation, the TiO_2 electrode produced oxygen as a result of water oxidation and hydrogen evolution occurred at the platinum counter electrode. They used an external bias or controlled pH difference between anode and cathode side. Since the finding, thousands of papers have been published about water splitting using semiconductor photocatalysts. After the first development of photoelectrochemical water splitting, particulate photocatalytic water splitting was studied, using photocatalysts with particle sizes ranging from micrometers to nanometers [1, 27, 28]. In this section, photocatalytic water splitting by particulate photocatalysts will be introduced, followed by a discussion of their principles. The photoelectrochemical water splitting by using photoelectrochemical cells will be described at the next section.

Figure 2.1 shows a schematic illustration of photocatalytic water splitting in a single phase photocatalyst with potential vs. normal hydrogen electrode (NHE) at pH = 7 [18]. Briefly, when a photocatalyst absorbs light energy with and energy greater than the bandgap of the photocatalyst, electrons in the valence band of the photocatalyst are excited to the conduction band while holes are left in the valence band. The holes can then migrate to the surface of the photocatalyst to react with water molecules while the electrons can migrate to a reduction site (such as a Pt cocatalyst particle) to produce hydrogen by bonding with protons (H^+) [29].

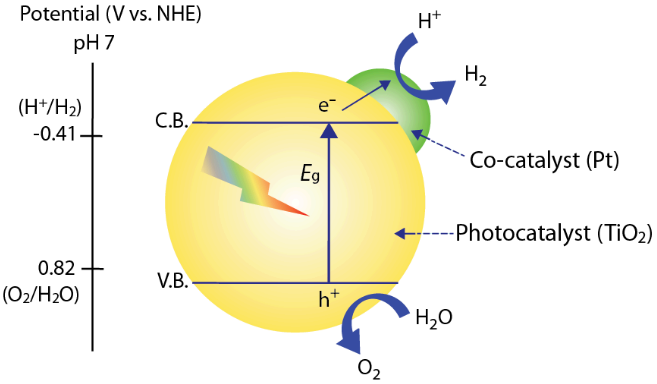

Figure 2.1 Schematic illustration of photocatalytic water splitting [29].

In the first step of the reaction, the catalyst should absorb photons to generate electron and hole pairs [30]. Since most photocatalysts are semiconductors, they have a bandgap between the conduction and valence bands. When incident light has an energy that is greater than the bandgap of the photocatalyst, the photocatalyst can generate electrons-hole pairs [30]. In other words, electrons are excited to the conduction band and holes are generated in the valence band. Then, the holes can split water molecules to oxygen and protons, and electrons in the conduction band can reduce protons to hydrogen. To realize that, the energy levels of the conduction and valence band states must meet with the requirement of water splitting [31].

Splitting water into hydrogen and oxygen requires a Gibbs free energy change of 237 kJ/mol or 1.23 eV and thus, the bandgap of photocatalysts should be higher than 1.23 eV [30]. In addition, the conduction band should be more negative than the reduction potential of H^+/H_2 (0 V vs. NHE, normal hydrogen electrode) to transfer electrons from the conduction band to meet H^+ to produce hydrogen [32]. In the same way, to transfer holes from the valence band to water to produce oxygen, the valence band should be more positive than the oxidation potential of O_2/H_2O (1.23 eV vs. NHE) [29].

Figure 2.2 shows the conduction and valence band energy levels of various semiconductors which can be used for water splitting [18]. From the left side, ZrO_2, $KTaO_3$, $SrTiO_3$, and TiO_2 (colored blue) have sufficiently large bandgaps and appropriately positioned energy levels to split water. CdS has a nearly ideal bandgap and energy levels, but is unsuitable because it degrades by photocorrosion; specifically, S^{2-} ion in CdS is more easily oxidized than water molecules. [30]. WO_3 has low bandgap energy and appropriate valence band to produce oxygen under visible light; however, the position of the conduction band makes it impossible to produce hydrogen.

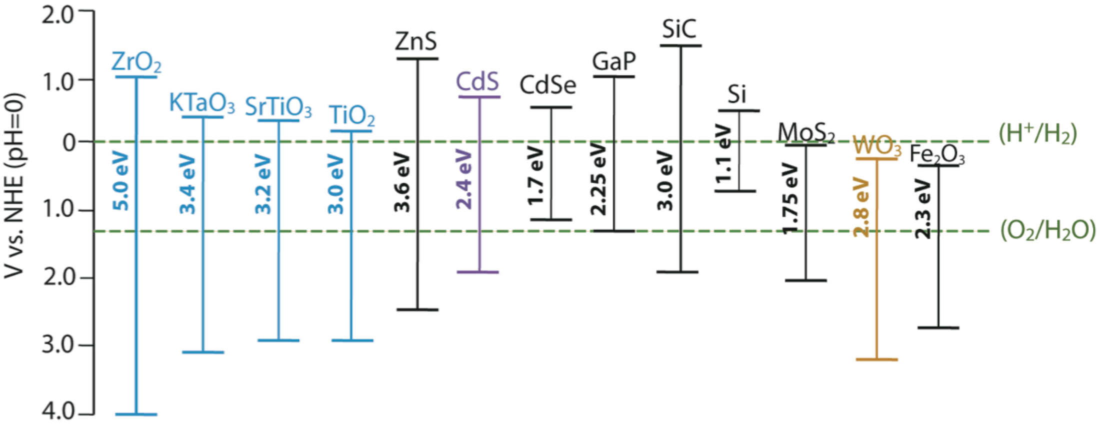

Figure 2.2 Relationship between the band edge energies of selected semiconductors and redox potentials of water splitting [18].

After photocatalysts absorb sufficient light energy and generate electron-hole pairs, the second step is the separation of the charge carriers to the reactive sites [30]. In this step, it is important to make the crystallinity of the materials since defects can act as traps where electron-hole recombination occurs. In addition, if the particle size is too small, the electron–hole pairs can be pinned each other before they move to the reactive sites; on the other hand, if the particle size is too large, the electron–hole pairs can recombine in the bulk, before they migrate to the surface [33]. Thus, it is important to have particles with the appropriate size; this will be dealt with in the chapter 5.

In the third step, the photogenerated charge carriers need to react with the surface species after they arrive at the reactive sites, and it is important to construct reactive surface sites for the photogenerated electrons and holes [30]. The surface area of the photocatalyst is directly related to the number of reactive sites and higher surface area can result in higher photocatalytic activity [31]. In addition to the surface area, highly active reactive sites by using cocatalyst such as noble metals can be also important to enhance photocatalytic activity [34, 35]. The effects of using noble metals will be dealt with later in this chapter. There have been many studies of heterogeneous photocatalysts using noble metal cocatalyst to reduce electron-hole recombination [36-38]. In summary, the three steps of photocatalytic water splitting are described in Figure 2.3.

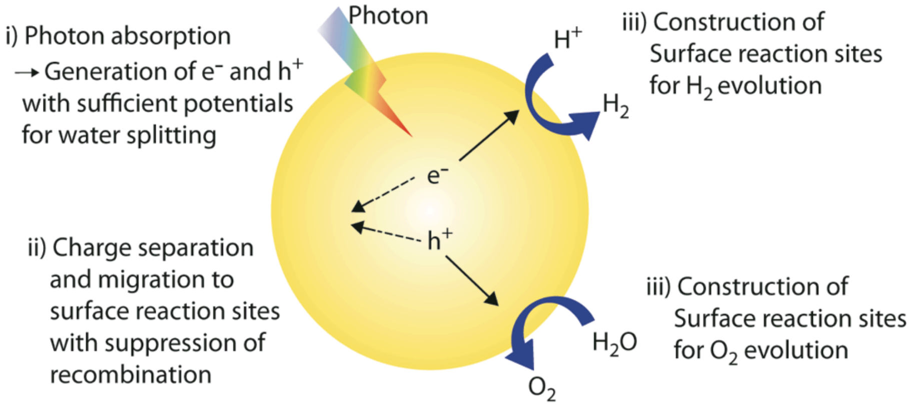

Figure 2.3 Three major steps for photocatalytic water splitting [30].

2.1.2 Photoelectrochemical water splitting

Photoelectrochemical (PEC) cells perform each half reaction at two separated electrodes and have great potential for efficient hydrogen generation [39] while heterogeneous photocatalysts perform both half-reactions of oxidation and reduction [40, 41], Multi-junction semiconductors have efficiencies slightly greater than 10 %; however, they are not stable enough to split water [42-44]. On the other hand, even though metal oxides have relatively lower efficiency, they have higher stability under light and electrolytes [26, 45, 46].

Figure 2.4 is an illustration of photoelectrochemical water splitting showing a semiconductor as a working electrode connected through an external circuit to a counter electrode [32]. During light irradiation, photogenerated holes remain in the photoanode to oxidize water to produce oxygen and photogenerated electrons can reach the cathode through the external circuit to produce hydrogen [32]. As mentioned in the previous section, the required Gibbs free energy to convert water molecules into hydrogen and oxygen is 1.23 eV and the photoanode materials should absorb light to make charge carries have potential differences greater than 1.23 eV [30]. However, because of overpotential losses, in practical operation, the required energy to split water to oxygen and hydrogen is 1.7-1.9 eV [47, 48].

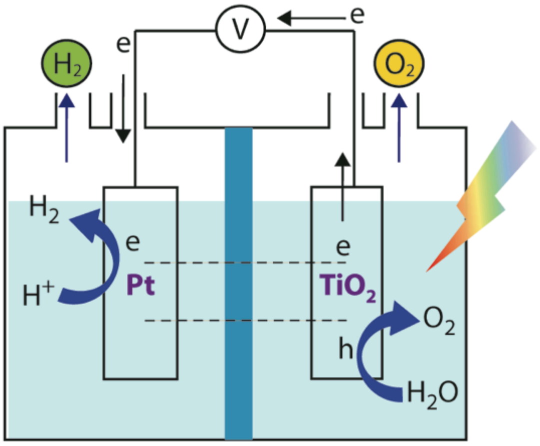

Figure 2.4 Schematic illustration of water splitting in a photoelectrochemical cell [32].

Photoelectrochemical cells for water splitting without using any external electrical circuits have also been developed. Nocera et al. [49] suggested an integrated wireless device composed of an amorphous silicon cell to split water molecules (Figure 2.5). The device with a wire shows an efficiency of 4.7 % and while the wireless device shows an efficiency of 2.5 %. Even though the wireless cell has a lower efficiency than the cell with the wired configuration, the wireless photoelectrochemical cells have potentially lower cost device structures [41].

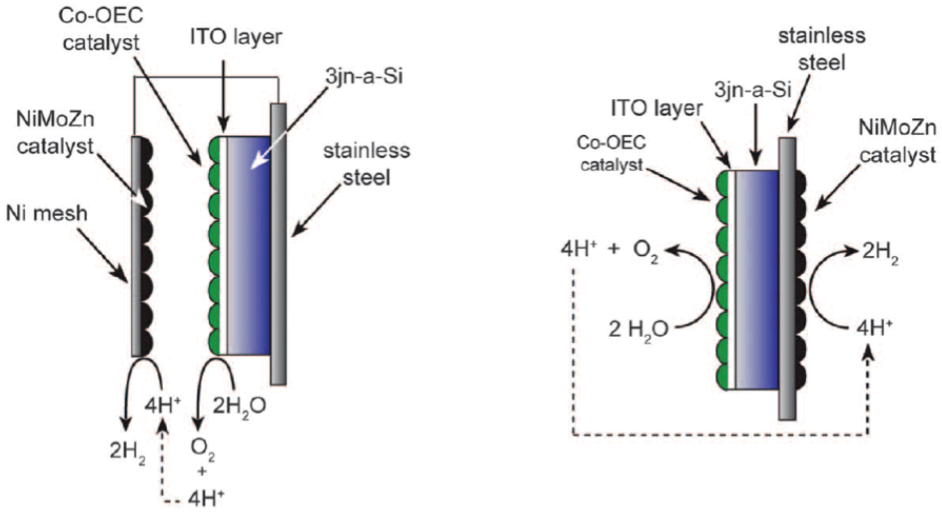

Figure 2.5 Wired (left) and wireless [2] photoelectrochemical cell. [49].

For photoelectrochemical water splitting, photoelectrode materials are important and various photoactive materials have been studied. The requirements for the photoelectrode are visible light harvesting with a narrow bandgap, suitable conduction and valence band energy levels to split water, low cost, and stability [32]. As mentioned above, the first photoanode was TiO_2 which has been developed by Fujishima and Honda in 1972 [26]. After that, many researchers studied photoanode materials to enhance photo-conversion efficiency by increasing surface area and reducing recombination rates [50, 51]. In addition to the photoanode materials, the architecture of the materials is also a crucial factor; specifically, nanotubes or nanowires have been getting attention because they have many advantages such as rapid diffusion due to reduced dimensionality and a high surface area hindering recombination of charge carriers [32]. Mor et al. [52] fabricated TiO_2 nanotubes using the anodization method and found they could split water with 4 % efficiency in UV light. Paulose et al. [53] also synthesized TiO_2 nanotubes by anodization and split water with 16.25 % efficiency under UV light. In addition to TiO_2 nanotubes, mesoporous TiO_2 has also been developed. Hartmann et al. [54] found that mesoporous TiO_2 synthesized by the sol-gel method could enhance the photocatalytic activity to split water ten times more efficiently than TiO_2.

Since TiO_2 has a large bandgap of 3.2 eV, narrow bandgap materials such as WO_3 [55, 56], Fe_2O_3 [57-59], and $BiVO_4$ [55, 60] have been also studied. The bandgap of WO_3 is 2.2 eV and that of Fe_2O_3 is 2.6 eV, which are attractive semiconductors as anode materials to generate oxygen by absorbing visible light [32]. Cristino et al. [61] synthesized mesoporous WO_3, tungsten trioxide, by anodization and conducted photoelectrochemical water splitting under AM 1.5 resulting a photocurrent of 9 mA/cm^2. Su et al. [62] prepared WO_3 nanoflakes that are vertically aligned and obtained a photocurrent of 1.43 mA/cm^2. Fe_2O_3, hematite, has a high chemical stability with low cost and used for photoelectrochemical water splitting. Mohapatra et al. [63] prepared Fe_2O_3 nanotubes using the anodization method and obtained a photocurrent of 1.41 mA/cm^2 and an efficiency of 0.84 % under AM 1.5. However, hematite has the disadvantages of slow kinetics to oxidize water and a short charge carrier diffusion length [64]. In the case of $BiVO_4$, nanowire structures were synthesized and showed 0.4 mA/cm^2 under AM 1.5 [65]. Those low activities were attributed to the poor transport of charge carriers and low chemical stability [32], which implies that strategies to improve the efficiency are necessary and some of the major strategies will be discussed later in this chapter.

2.1.3 Photocatalytic Dye Degradation

In addition to photocatalytic water splitting, to test photocatalytic activity, photocatalytic dye degradation is one of the most widely used methods. From an experimental point of view, the photocatalytic degradation of methylene blue is a relatively easy way to measure photochemical activity because it involves measuring the concentration of the product in aqueous solution using optical spectroscopy. Conversely, in the water splitting experiment, the products must be collected and analyzed in the gas phase. In addition, decomposition of organic pollutants in wastewaters is one of the possible applications of these catalysts [66, 67]. Traditionally, physical techniques using various absorbents have been used [68, 69] to purify waste water; however, chemical decomposition of dye molecules in addition to the physical sorption is also required to prevent secondary pollution [67]. For photochemical decomposition, the key issue is the generation of hydroxyl radicals ($^{\bullet}OH$), which are the reactive species that decompose organic molecules [67]. To realize that, solar energy-assisted catalytic degradation of dye molecules using titanium dioxide (TiO_2) is an emerging technology [70, 71]. Meanwhile, among various dyes, methylene blue, $C_{16}H_{18}N_3SCl$, is generally used [72] to test the photocatalytic activity of materials such as TiO_2.

There have been many publications on the mechanism of photocatalytic dye degradation [66, 73-75]. As in photocatalytic water splitting, when TiO_2 absorbs light with an energy greater than the bandgap of it, 3.2 eV, electrons and holes are generated in the conduction band and the valence band, respectively. The dye molecules can be oxidized by the photogenerated holes while electrons in the conduction band can also reduce dye molecules [67]. In indirect ways, the photogenerated holes react with OH^- or

H_2O and can produce $OH^\bullet$ radicals; the generated $OH^\bullet$ radicals are strongly oxidizing and can react with the dye [67]. Meanwhile, the electrons in conduction band can also produce superoxide radicals, $O_2^{\bullet -}$, which may also decompose dyes and these reactions that may participate in the photodegradation of dyes by TiO_2 are described as follows [66, 67]:

1. Absorption of photons ($h\nu \geq E_g = 3.2$ eV): $(TiO_2) + h\nu \rightarrow e^-_{CB} + h^+_{VB}$
2. Direct oxidation by reaction with holes: $R + h^+ \rightarrow R^+ \rightarrow$ oxidation products
3. Direct reduction by reaction with electrons: $R + e^- \rightarrow R^-$ → reduction products
4. $OH^\bullet$ radicals produced by holes: $(H_2O \Leftrightarrow H^+ + OH^-)_{ads} + h^+_{VB} \rightarrow H^+ + OH^\bullet$
5. Oxidation of the dye molecules by $OH^\bullet$ radicals: $R + OH^\bullet \rightarrow R^\bullet + H_2O$
6. $O_2^{\bullet -}$ radicals produced by electrons: $TiO_2\,(e^-_{CB}) + O_2 \rightarrow TiO_2 + O_2^{\bullet -}$

2.2 Titanium dioxide (TiO_2) as a photocatalyst

2.2.1 TiO_2 as an UV-active photocatalyst

TiO_2 is a promising photocatalyst for water splitting due to its appropriate bandgap and energy levels to split water, stability, and abundance. With these advantages, there have been various approaches to synthesize various shapes of TiO_2 such as nanotubes [8], nanorods [76], nanowires [77], and mesoporous spheres [78], which can be used to enhance photocatalytic activity. Among these structures, TiO_2 nanotube arrays have outstanding photocatalytic properties derived from their one-dimensional geometry that facilitates charge transfer [8, 79]. In addition to morphology, the phase of TiO_2 is also a significant factor for photocatalytic activity [80-84]. Anatase and rutile are the two major phases of TiO_2 [85, 86] and it has recently been reported that a combination of anatase and rutile shows higher photocatalytic activity than anatase alone because the difference in the bandgaps of rutile and anatase creates junctions that hinder charge carrier recombination [87].

TiO_2 has plenty of advantages as mentioned above; however, it also has several limitations such as a wide bandgap (3.2 eV) that lets TiO_2 absorb only ultraviolet light [1]. Because UV light makes up only a small portion (5%) of the energy in the solar spectrum, compared to 50 % for visible light, it is desirable to reduce TiO_2's bandgap so that it absorbs some light in the visible region [12, 88-90]. Moreover, the efficiency of TiO_2 is limited by fast recombination of charge carriers [35, 91]. Thus, structures that have faster charge transfer and thereby hinder charge carrier recombination are also needed for highly efficient photocatalytic water splitting. To extend the absorption range of TiO_2 to the visible part of the spectrum, doping with nonmetallic elements such as carbon [92, 93], nitrogen [94-96], and sulfur [97, 98] has been explored. Transition metal ion doping has also been explored and vanadium [99, 100], chromium [101-103], nickel [104, 105], and iron [106-108] are examples. The details of doped TiO_2 and its enhanced visible light absorption and photocatalytic activity will be described in the following section.

2.2.2 Improvement of visible light harvesting

To overcome the limitation of poor visible light absorption, researchers have explored metal or nonmetal ions doping for band gap narrowing and the formation of heterostructures by combining TiO_2 with other semiconductors or metals [10]. Among the approaches, transition metal ion doping has been extensively studied [11, 109-115]. Choi et al. [11] doped 21 different metal ions into TiO_2 and compared the photocatalytic activity of the doped materials. They demonstrated that Fe, V, Mo, Rh, Ru, and Os could enhance the visible light absorption of TiO_2; specifically, they said metal ion doping can occur on the surface of TiO_2 to transfer charge carriers rather than deep doping within TiO_2.

Peng et al. [116] investigated photocatalytic water splitting to produce hydrogen with Be ion doped TiO_2. The Be doped TiO_2 was 75 % more active than pristine TiO_2. They also found that doping surface sites is beneficial site charge carrier transfer. Metal ion doping could narrow the bandgap of TiO_2, resulting in visible light absorption and enhanced photocatalytic activity. However, there are a few issues such as atom diffusion and thermal stability that must be solved before metal ion doping can be used [11]. In addition, metal ions are defect sites and increase the recombination rate of electron and hole pairs reducing photocatalytic activity [11, 12]. Thus, non-metal doping has been getting attention and investigations using C, N, S, F, and B have also shown improved photocatalytic activity under visible light [2, 13-17].

Non-metal doping of TiO_2 with C, N, S, F, and B have been extensively studied and it is known that these additions extend absorption to the visible part of the spectrum [13, 94, 95, 117-122]. These anions can be more effective than metal ion doping because they do not increase the recombination rate as much. Asahi et al. [94] investigated C, N, S, F, and P doping which are thought to substitute for oxygen. They demonstrated that the bandgap narrowing was attributed to an interaction between the p orbitals of N and the 2p orbitals of O. In the case of S, even though bandgap narrowing was also found, sulfur is too large to be dissolved in TiO_2. Nitrogen doped TiO_2 showed enhanced visible light activity by decomposing methylene blue. Among those anions, carbon doped TiO_2 has received the most attention. Khan et al. [13] investigated photocatalytic water splitting under visible light using carbon doped TiO_2 which was synthesized by combustion of Titanium. Zhao et al. [12] synthesized carbon-doped TiO_2 by a solvothermal method. The C-doped TiO_2 showed a high surface area of 120 m^2/g and photocatalytic activity under visible light. They mentioned that the origin of the enhanced in visible light activity is from optical charge transfer in both TiO_2 and carbon, which cannot occur in physically mixed composites.

2.3 TiO_2-CNT composites

2.3.1 Hetero-junction of TiO_2-carbon materials

Among various methods to enhance visible light absorbance of TiO_2, hybrids with carbon materials have been getting attention because titania's bandgap is narrowed by carbon atomic doping as well as the electronic interaction between TiO_2 and carbon [19]. There are plenty of carbon materials that can support TiO_2, and among them, activated carbon with a large specific surface area has been used to support TiO_2 for photocatalytic degradation [123]. In this system, the Langmuir-Hinshelwood mechanism was used to analyze the photocatalytic degradation requiring molecular absorption and thus, a large surface area of the activated carbon increases the number of adsorbed molecules and their degradation rate [19]. Matos et al. [124] investigated the photocatalytic degradation of phenol using TiO_2 P25 with activated carbon. The activated carbon-supported TiO_2 could adsorb significant amount of phenol and decompose it efficiently.

In addition, hybrids of TiO_2 with carbon materials such as graphene [125], carbon nanotubes (CNT) [126], and graphite-like carbon [127] have gained interest recently to improve charge transfer as shown in Figure 2.6. Yang et al. [125] studied the structure and electronic properties of TiO_2-graphene composites by density functional theory and also showed outstanding performance for the photocatalytic degradation of methylene blue. Cui et al.[127] prepared TiO_2 with carbon nanodots and studied the rational design of carbon based nanostructures. They suggested that carbon nanodots on the TiO_2 surface could serve as electron acceptors resulting in efficient separation of electron-hole pairs. Among the carbon materials, carbon nanotubes (CNTs) have been getting significant attention as a supporting material in photocatalysis and photoelectrochemical cells. The major advantage of the CNT-photocatalyst composite is that Schottky barriers are formed at the semiconductor-metal junctions and they reduce charge carriers recombination [19]. In the semiconductor and metal junction where the metal has a higher work function, photogenerated electrons in the semiconductor can transfer to the metal at the interface and as a result, the semiconductor has excess holes while the metal has excess electrons, which induces charge separation [19]. In addition, the interface can induce a new energy level, reducing the bandgap TiO_2 [9, 128].

2.3.2 Carbon nanotubes

Carbon nanotubes were first discovered by Iijima in 1991[129] and attracted interest because of their outstanding physical and chemical properties [130-137]. The structure of carbon nanotubes can be described with reference to graphene layers. Graphene layers are composed of hexagonal arrangements of carbon bonds and when these graphene layers are rolled into cylinders, carbon nanotubes are formed. There are two types of carbon nanotubes and these are multiwall nanotubes (MWCNTs) and single wall nanotubes (SWCNTs) that result from different synthesis methods. The diameter of a SWCNT is a nanometer and the diameter of a MWCNT is a few nanometers to tens of nanometers [138].

Single Wall Carbon Nanotubes (SWCNTs) were discovered by Iijima and his group at the NEC Laboratory and by Bethune and coworkers at the IBM Almaden laboratory [139]. To understand the structural properties of SWCNTs, they used the chiral vector $\mathbf{C}_h = \mathbf{n}\mathbf{a}_1 + \mathbf{m}\mathbf{a}_2$ connecting two crystallographically equivalent sites on a 2D graphene sheet (Figure 2.6); where (**n, m**) are the chiral vector [140]. By rolling up the graphene sheet, nanotube structures can be generated and when the chiral angles which is between the chiral vector are 0, the nanotubes are called zigzag, and in the case of the chiral angles = 30^{o}, the nanotubes are called armchair nanotubes [140].

There are three classes in SWCNTs based on MOD (2n + m) = 0, 1 or 2 to distinguish whether the SWCNTs are metallic or semiconductor, and when the MOD, (2n + m) can be divided by 3, the SWCNTs are metallic [140]. When MOD = 0, only armchair (n = m) is perfectly metallic because other cases have a small chirality-dependent energy gap, and when MOD = 1 and MOD = 2, these cases are two types of semiconducting SWCNTs [140]. Single walled carbon nanotubes (SWCNTs) have been regarded as promising materials to serve as a substrate and photosensitizer in photoelectrochemical water splitting and photovoltaic devices due to their excellent electron mobility [23]. However, efficiency improvements have not been reported because SWCNTs usually form in bundles that create contacts between them due to van der Walls [21, 24]. It is possible to disperse the SWCNTs using chemical modifications [141] and surfactants [126].

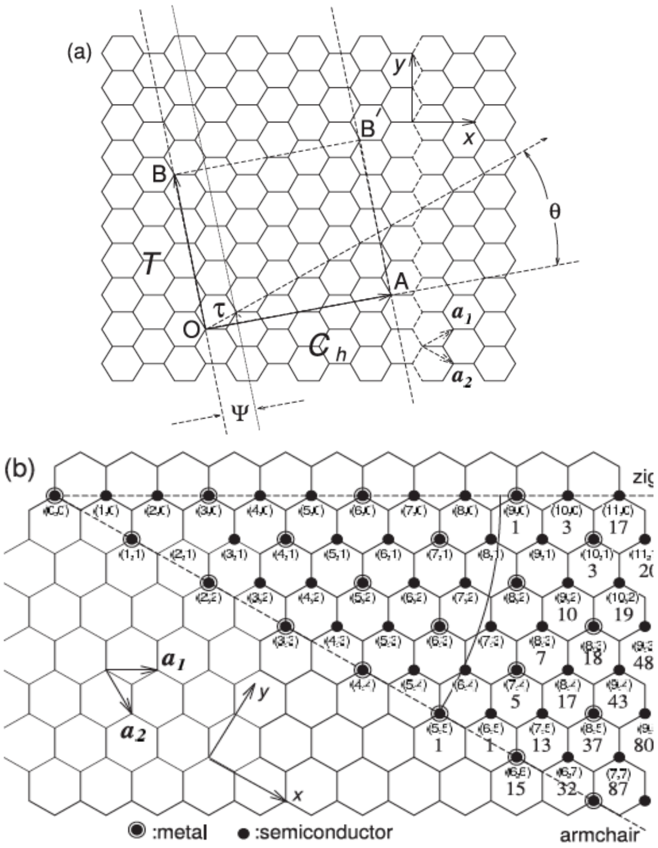

Figure 2.6 (a) Illustration of the chiral vector $C_h = na_1 + ma_2$ with unit vectors of a_1 and a_2. The diagram is in the case of (n, m) = (4, 2). (b) The integers (n, m) to present zigzag, armchair, and chiral nanotubes [140].

2.3.3 TiO_2-CNT composites as photocatalysts

Since CNTs have excellent electrical properties such as a large electron-storage capacity [142], they can accept the electrons transferred from TiO_2 reducing the recombination rates [19]. Hoffmann et al. [71] determined that the chemical interaction between a photocatalyst and adsorbed molecules has a recombination time of $10^{-8} – 10^{-3}$ s while the recombination time of electron and holes is on the order of 10^{-9} s. Thus, the Schottky junction of the TiO_2-CNT composites can help to increase the lifetime of charge carriers. Meanwhile, CNTs have a large surface area which increases the number of reactive surface sites, which is a key factor to enhance the photocatalytic activity of TiO_2 [19]. Wang et al. [143] reported that CNTs can act as a photosensitizer when they are combined with TiO_2 and this leads to an enhancement of the photocatalytic efficiency. Since pristine TiO_2 can only absorb UV light, which is 5 % of all sunlight, extending light absorption to the visible region is critical. In addition to the carbon doping effect, CNTs can exhibit photosensitizing properties that enable the composite to act as a visible light of photocatalyst [143, 144].

There have been reports of TiO_2 coated on MWCNTs or/and SWCNTs, and their application as photocatalysts [19, 145-148]. Woan et al.[19] grew TiO_2 on CNTs dispersed in a liquid medium. They said that the]the precursor is important because the reactivity of the precursor can affect homogeneous or heterogeneous nucleation of TiO_2. Gao et al. [145] developed SWCNT-TiO_2 nano composite film fabricated via sol-gel process of TiO_2 coated on a SWCNT network film (Figure 2.7 (a)-(c)). They showed the flexible nano-composite films could separate both surfactant free and surfactant-stabilized oil-in-water emulsions under UV light irradiation. Dang et al. [146] reported the synthesis of SWCNT–TiO_2 nano-crystal core shell nanocomposites by using a genetically engineered M13 virus as a template (Figure 2.7 (d) and (e)). They demonstrated that carbon nanotubes improve the efficiency of dye-sensitized solar cells by increasing the electron collection efficiency.

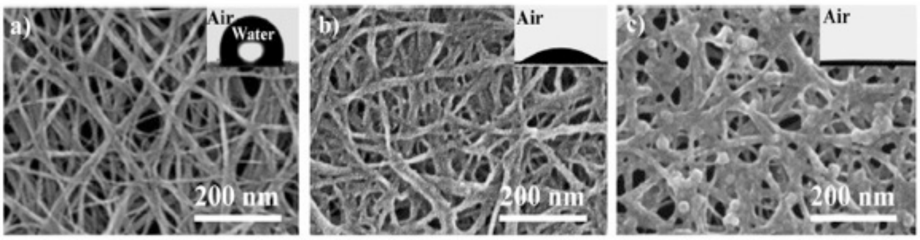

0 mM 0.5 mM 1 mM

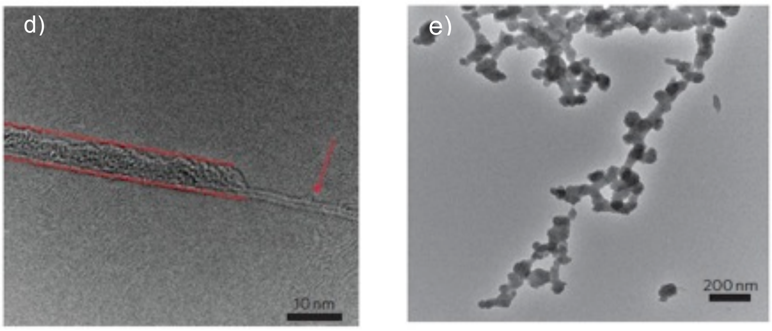

Figure 2.7 (a)-(c) SEM images of SWCNT-TiO_2 nano composites films with the concentrations of TiO2 precursor, TBT, 0, 0.5, 1, respectively [145]. (d)-(e) TEM images of virus/SWCNT/TiO_2 complexes and the arrows in (d) indicates SWCNTs and a virus is indicated by dashed lines. [146].

2.3.4 Synthesis of CNTs by polymerization of glucose

There have been various methods to synthesize carbon nanotubes and the most widely-used techniques are the arc-discharge method [149, 150], chemical vapor deposition (CVD) [151, 152], high pressure decomposition of carbon monoxide (HiPco) [153], the cobalt-molybdenum catalyst method (CoMoCAT) [154], and the Laser Furnace method [155, 156]. Recently, hydrothermal carbonization (HTC) and the pyrolysis by using biomass such as glucose have gained increasing attention due to the prospect of processing waste biomass into valuable carbonaceous materials [157]. In addition, it is easy to use these methods because they require only a Teflon-lined autoclave and a furnace to heat it. Falco et al. [157] investigated the hydrothermal treatment and pyrolysis of glucose, a good model carbohydrate, using solid state ^{13}C NMR. They reported that the hydrothermal treatment of glucose at 180 °C for 12 h, followed by pyrolysis at 750 °C under nitrogen, resulted in materials which are entirely composed of polyaromatic hydrocarbons.

Li and co-workers [20] fabricated aligned carbon nanotube arrays using glucose as a carbon source and an anodic aluminum oxide (AAO) template. They polymerized glucose on an AAO template to form a mixture of organic polymers by a hydrothermal treatment and then pyrolyzed the material at 900 °C, to coat uniformly on the inner surfaces of the AAO templates and to create open ended-carbon nanotubes. Meanwhile, direct pyrolysis without a hydrothermal treatment has been also developed to make graphene. Tour and co-workers [158] used solid carbon sources and synthesized high quality graphene with a controllable thickness at a low temperature of 800 °C. As a carbon source, a spin-coated poly(methyl methacrylate) (PMMA) thin film (~ 100 nm) as a was used, and a Cu film was used as the metal catalyst substrate. They successfully synthesized a single uniform layer of graphene on the substrate at a temperature as low as 800 °C or as high as 1,000 °C and the reaction time was 10 min in a low-pressure reductive gas flow (H_2/Ar). These techniques are applicable to make high quality carbon nanotubes by the pyrolysis of a carbon source.

2.4 Improvement in separation of charge carriers, intermediates, and products

2.4.1 Cocatalysts loading for separation of charge carriers

The separation of charge carriers and products is another key factor affecting photocatalysis and it is important to quickly transfer the photo-generated charge carriers to the reaction site, avoiding charge recombination to enhance the reaction rate of photocatalysts [32]. Among various methods to realize efficient transfer of charge carriers to reactive sites before recombination, cocatalysts such as Pt, Au, Pd, Ag, Ni, Cu, and Rh are used and generally lead to improved photocatalysis [36-38, 159-165]. These noble metals have lower Fermi levels than TiO_2 and thus, photo-excited electrons in the conduction band of TiO_2 can transfer to the noble metals, reducing the recombination of electron-hole pairs [35].

Platinum is one of the most efficient catalysts and widely used as a cocatalyst with photocatalysts in the form of supported nanoparticles [34]. It is also used as a photocathode in photoelectrochemical cells in the form of a wire or sheet [26, 166]. In the case of photocatalytic water splitting or dye degradation, if Pt nanoparticles are deposited on the surface of photocatalyst, the photocatalytic reaction rate can be enhanced as photo-generated electrons are collected by the Pt nanoparticles, and this prevents recombination [35]. Many researchers have studied the effect of Pt cocatalysts on photocatalytic activity of TiO_2 or other photocatalysts. Anpo et al. [34] investigated electron transfer from TiO_2 to Pt nanoparticles by using Electron Spin Resonance (ESR) signals. In the Pt coated TiO_2 system, the Fermi level of Pt was shifted closer to the conduction band of TiO_2 [38, 162, 167], which is beneficial to produce hydrogen from water. The electrons transferred from TiO_2 to the noble metal can react with adsorbed protons and reduce them to hydrogen. To compare the activities of Pt and Au, Bamwenda et al. [159] prepared Pt and Au-loaded titania and investigated photocatalytic hydrogen production from a water-ethanol solution. As a result, Pt loaded TiO_2 showed higher photocatalytic activity than Au-loaded TiO_2. In addition, various deposition methods such as traditional impregnation, precipitation, and photodeposition were used to determine if the photocatalytic activity depended on the preparation method and they found that photodeposition shows better performance than others due to better contact between the metals and TiO_2. Meanwhile, Sakthivel et al. [168] studied the effect of the amount of added metal on photocatalytic activity. They found that light absorption in TiO_2 was reduced when TiO_2 is covered by too many metal particles and this resulted in lower reactivity.

2.4.2 Separation of intermediates and products

Hydrogen (H_2) and oxygen (O_2) can be generated by photocatalytic water splitting; however, they are always mixed in a particulate photocatalysis system. Thus, the development of a new device to produce H_2 and O_2 separately is one of the great challenges [169, 170]. Selli et al. [166] employed a new two-compartment cell, which allows water to be split separately into H_2 and O_2 on a photoactive Ti and Pt electrode as displayed in Figure 2.8 (a).

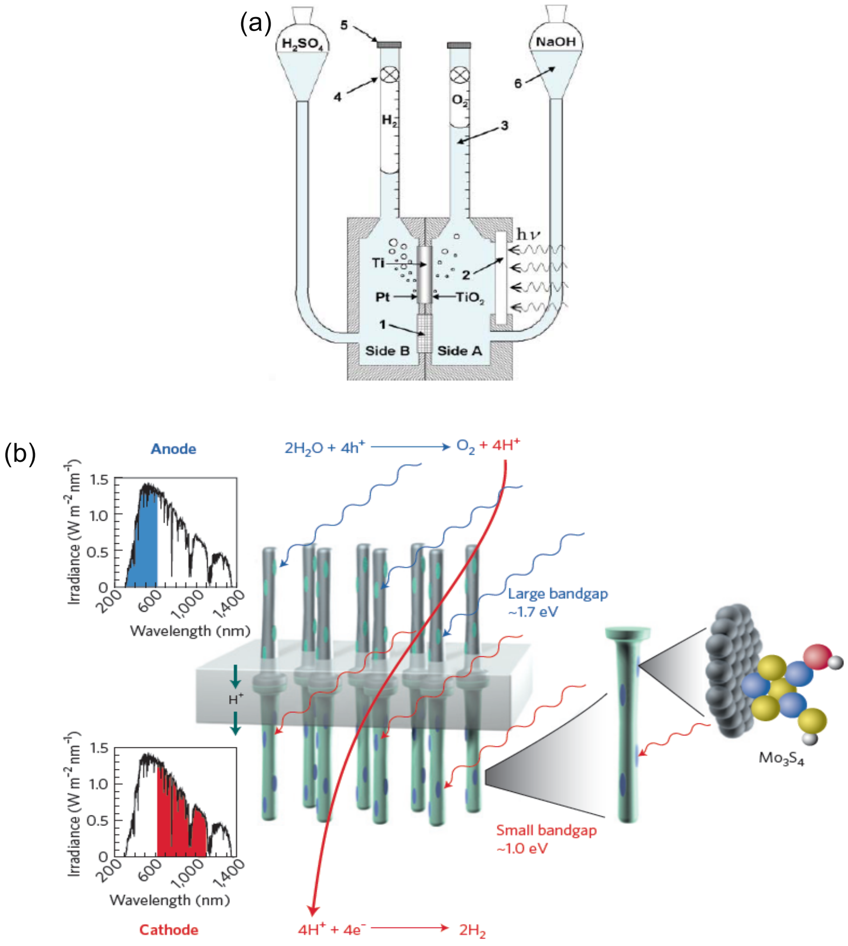

Figure 2.8 (a) Photocatalytic water splitting with separate H_2 and O_2 evolution [166]. (b) Schematic of a device based on a tandem design [171].

Hou et al. [171] developed a new device using bio-inspired molecular clusters based on molybdenum and sulphur to separate oxidation and reduction sites as shown in Figure 2.8 (b). When the anode absorb the blue part of the spectrum, water oxidation occurred in a proton-conducting membrane and then, the protons transfer through the membrane and produce hydrogen at the cathode side by the red part of the spectrum. Despite this progress, there is still a need to design new materials or devices that will spatially separate the products of water splitting in a simple, low cost way. In this work, a new approach to the separation of oxidation and reduction sites will be shown using nanotubes whose outside is the oxidation site and inside is the reduction site.

The separation of charge carriers is also crucial for effective photocatalysis. To verify the separation of photo-generated electrons and holes, the photodeposition of metal or/and metal oxides on photocatalysts has been reported. Munprom et al. [172] reported ferroelastic domains in $BiVO_4$ which could promote the spatially selective reduction of Ag from an aqueous solution. The domain microstructure showed lamellar contrast as shown in Figure 2.9 (a) left, and after silver ions are photochemically reduced to silver metal only on certain domains, the same surface is shown in Figure 2.10 (a) right. In this way, the polar response of $BiVO_4$ can be investigated by photo-generated charge carrier separation.

Li et al. [173] used monoclinic bismuth vanadate crystals and achieved effective charge separation. They concluded that the reduction reaction took place on the {010} facet and oxidation reaction was on {110} facets under photo-irradiation as shown in Figure 2.9 (b). The selectively deposited reduction and oxidation catalysts resulted in much higher photocatalytic activity of water splitting, compared with the randomly distributed photo catalyst. In this work, the photoelectrochemical cells we developed the separate oxidation and reduction reactions and, to verify the separation, the photo-deposition of metal and metal oxides is used in a way similar to the studies of $BiVO_4$.

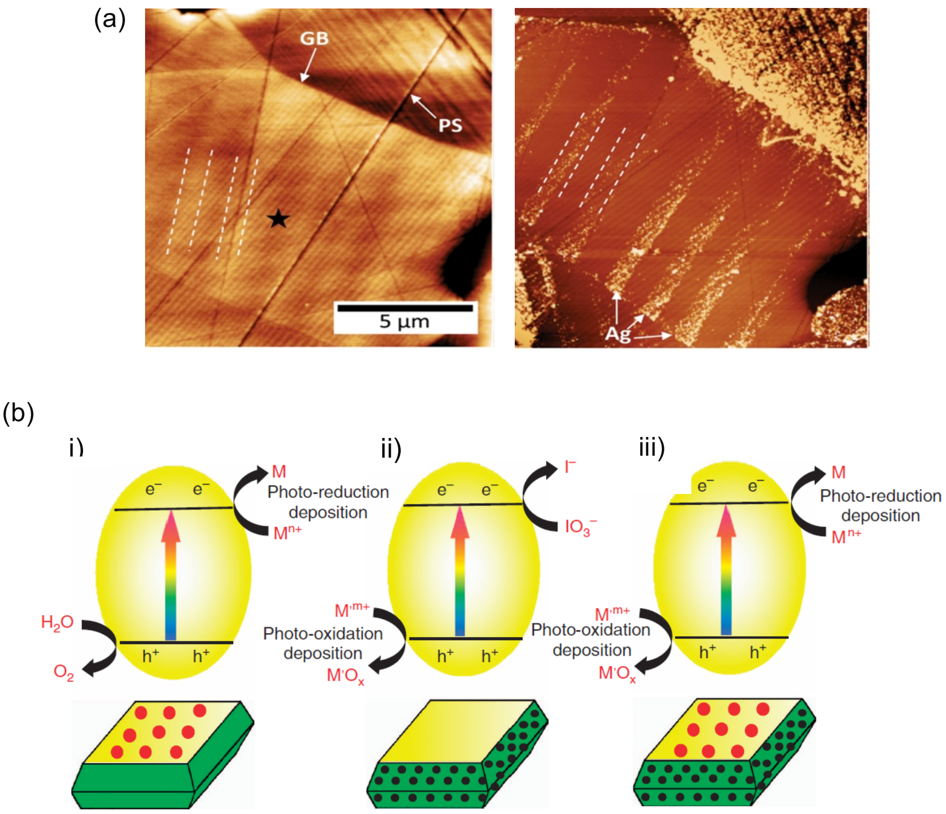

Figure 2.9 AFM image before (a) and (b) after photo-deposition of Ag. [172]. (b) Selective photo-deposition on $BiVO_4$ i) photo-reduction deposition of metals ii) photo-oxidation deposition of metal oxides iii) simultaneous photo-deposition of metal and metal oxides [173].

Chapter 3

Experimental Overview

3.1 Anodic aluminum oxide (AAO) template method

Template methods are widely used to synthesize specific structures. As long as the template can be removed, free standing materials can be created. Among various template methods, anodic aluminum oxide (AAO) has been used to make one-dimensional structures such as nanotubes and nanowires [20]. The advantage of using the AAO template is that ordered nanostructures perpendicular to the substrate are created instead of a randomly oriented network [20]. Chu et al. [174] synthesized TiO_2 nanotubes successfully using sol-gel infiltration on the AAO templates and Durstock et al. [175] developed a versatile technique to fabricate highly ordered TiO_2 nanotubes based on a directed growth on AAO template via sol- gel infiltration.

In addition to TiO_2 nanotubes, carbon nanotubes are also synthesized by the AAO template method [20]. Although CNT synthesis methods such as the arc-discharge method and the chemical vapor deposition method are the most common techniques for making nanotubes, the products contain metal impurities that must be removed and it is hard to produce well-aligned and open-ended CNTs [20]. By using the AAO template method, aligned multi-walled and diameter-controlled carbon nanotubes can be easily synthesized with open ends, implying the possibility of the deposition of metal nanoparticles or a double coaxial structure [176]. Wen et al. [20] developed aligned arrays of CNTs via the in situ hydrothermal polymerization of glucose by using AAO templates, followed by carbonization at high temperature. They then deposited Pt nanoparticles on the surfaces of the carbon nanotubes using the wet method. The transmission electron microscopy image of the synthesized CNTs shows a tubular structure with a diameter of around 200 nm, which corresponds to the pore size of the AAO template. They said that the advantage of using the AAO template is that the diameter and length of the open-ended CNTs are tuned by selecting an appropriate AAO template. In addition, the overall procedure is convenient and some of the advantages are the relatively low cost and the ability to control the wall thickness.

3.2 Characterization methods

Scanning Electron Microscopy

Scanning Electron Microscopy (SEM) uses secondary electrons to analyze the morphologies of materials. The SEM images were taken with a FEI Quanta 600. For sample preparation, the TiO_2-CNT-Pt membranes and TiO_2-SWCNT aerogels were broken into small pieces and put onto a SEM sample holder using a carbon tape. Since the real resolution is limited to a few nanometers, the TiO_2-CNT-Pt membranes could be easily imaged; however, it is difficult to image individual SWCNTs. To take images of SWCNT aerogels, a smaller spot size was chosen and an acceleration voltage of 10 kV was used. Elemental analysis of the composites was performed with the energy dispersive X-ray spectrometer (EDS) in the ASPEX SEM.

Transmission Electron Microscopy

Transmission Electron Microscopy images in chapter 4 and 5 were taken with a Tecnai F20 at 200 kV. For the preparation of any samples discussed in chapter 4, all AAO templates of TiO_2-CNT-Pt membranes were removed by dissolving them in 2 M NaOH with stirring. The samples were washed with DI water several times until neutralization, followed by centrifugation. After overnight drying, the samples were sonicated in ethanol. Finally, the samples with ethanol were dropped onto a holey carbon grid. The TEM image in chapter 6 was taken with a JEOL 2000EX. For the TEM sample preparation of the TiO_2-SWCNT aerogels, the aerogels were sonicated in ethanol for 10 min, followed by dropwise deposition onto a holey carbon grid.

Raman spectroscopy

Raman spectroscopy is used to analyze vibrational modes and microstructure of the materials. For analysis of CNTs, since only a small amount of sample is needed, it is easy to prepare samples to measure Raman spectroscopy. In addition, since CNTs have a specific Raman spectrum of radial breathing modes (RBM), the D-band, the G-band, and the 2D-band, it is desirable to analyze the structure of CNT composites using Raman spectroscopy.

The Raman spectra were collected using a Raman confocal microscope (inVia Raman microscope, Renishaw) using a 50× air objective with a numerical aperture of 0.75 (Leica Microsystems) and a 785 nm (1.58 eV) laser. Laser power was set to 10 mW and the laser beams have 1-2 μm spot size with an exposure time of 1 second. We collected five scans each at five different locations for each sample to verify uniformity within a sample and then averaged the scans to improve the signal-to-noise ratio. We performed the data collection and data analysis using WiRE software (Renishaw). Each Raman spectrum was normalized by its G-band intensity; note that the G-band at ~1591 cm^{-1} is a characteristic Raman feature of CNTs and quantified sp^2-hybridized carbon bonds.

Surface area and pore size distribution

The specific surface area of materials can be analyzed by the Brunauer, Emmett and Teller method [177]. The method is based on multilayer gas adsorption on surfaces and the observations are interpreted using a mathematical model that makes it possible to compute the number of adsorbed molecules [177]. In this work, the specific surface area of materials was examined through adsorption-desorption isotherms of nitrogen at 77 K using a surface area analyzer (Micromeritics Gemini VII 2390) and the Brunauer−Emmet−Teller [178] theory. The BET surface area was calculated by using the isothermal curve at a specific range of relative pressure, $0.05 < P/P_0 < 0.3$. The pore size distribution and pore volumes were calculated using Barrett−Joyner−Halenda (BJH) methods from the desorption branch of the isotherms.

UV-Visible Absorption/Reflection Spectroscopy

The optical properties of the samples in chapter 4, 5, and 6 were investigated using an UV-Visible Reflection or OL 770-LED Multichannel spectoradiometer and a cold cathode mercury (Hg) vapor lamp as a light source. For the measurement of reflection, solid samples with a size of 0.7cm × 0.7 cm were used. The reflectance was converted by using Kubelka-Munk (K-M) function which can be described as following equation [179]:

$$F(R) = \frac{k}{s} = \frac{(1-R)^2}{2R}$$

where F(R) is Kubelka-Munk function, R is the reflectance, k is absorption coefficient, and s is scattering coefficient.

To investigate the photocatalytic degradation of methylene blue, the concentration of methylene blue was analyzed by measuring the light absorbed at a specific wavelength, 665 nm, using a Varian Cary 5000 UV-vis-NIR spectrometer. In chapter 6, to analyze the concentration of SWCNTs, UV-vis absorbance spectra of pristine SWCNT aerogels were measured by Varian Cary 5000 UV-vis-NIR spectrometer.

X-ray photoelectron spectroscopy (XPS)

We collected XPS data with a DESA 150 analyzer (Staib instruments). The X-ray source was Al Kα X-rays from a TX400/2 X-ray gun (PSP vacuum technology). We carried out elemental analysis using CasaXPS.

Photocatalytic methylene blue degradation

Photocatalyst was put into an aqueous solution of 0.02 mM methylene blue and then trapped air was removed by a vacuum filtering. The suspension was stirred in the dark for various durations of time. The specimen in methylene blue solution was irradiated with a 300 W Hg lamp equipped with an UV filter ($\lambda > 420$ nm), IR filter, and cooling system. 0.5 ml of the methylene blue solution was periodically withdrawn and its absorbance was measured using a Varian Cary 5000 UV-vis-NIR spectrometer. The concentration ratio, C/C_0 was calculated using the intensity at 665 nm which is the maximum of the methylene blue visible light absorption. C is the concentration of the methylene blue at each time and C_0 is the initial concentration of methylene blue.

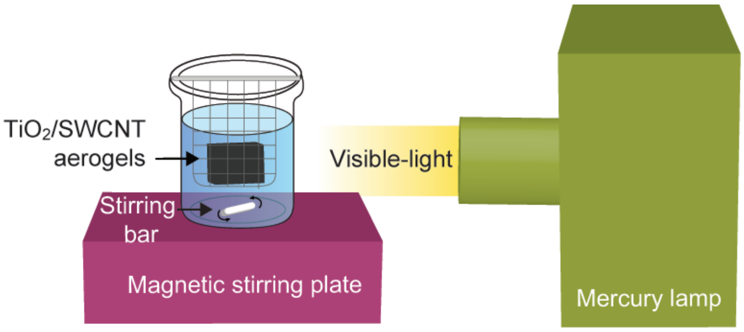

Figure 3.1 Schematic illustration of photocatalytic methylene blue degradation experiment.

Chapter 4

TiO_2-CNT-Pt membrane with Spatially Separated Oxidation and Reduction Channels

4.1 Research Goal and Hypotheses

In this chapter, the goal of the research is to develop a photoelectrochemical cell consisting of a TiO_2-CNT-Pt membrane with spatially separated oxidation and reduction channels to efficiently split water. The cell is composed of an abundant photocatalyst, TiO_2, CNTs as a separator between the oxidation and reduction sites, and a co-catalyst, Pt, as the reduction site. TiO_2 is located on the outside of the CNTs and Pt nanoparticles are located on the inside of the CNTs.

The hypothesis of the research is that the oxidation reaction will occur on the outside of a carbon nanotube and the reduction reaction will occur on the inside of the carbon nanotube, which would enhance photocatalytic activity due to separation of both the charge carriers and the products. Moreover, CNTs can enhance the photocatalytic activity of TiO_2 by extending the light response of the TiO_2 as well as assisting the charge transfer from the TiO_2 to CNTs [180-182].

4.2 Experimental methods

4.2.1 Synthesis of the TiO_2-CNT-Pt membrane

Synthesis of TiO_2 on AAO

The synthesis process of the TiO_2-CNT-Pt membrane is described in Figure 4.1. For the TiO_2 synthesis, titanium [82] butoxide, $Ti(OCH_2CH_2CH_2CH_3)_4$, was used as a precursor and a titanium butoxide (denoted as TBOT) solution was prepared by mixing absolute ethanol (100 %) with a molar ratio of TBOT:ethanol of 1:100 under a N_2 atmosphere. Anodic aluminum oxide (AAO) membranes (Whatman) with 0.2 μm pores, 60 μm thickness, and a 25 mm diameter were used as templates to make nanotubes. The AAO templates were first immersed in 2 mL of TBOT solution and then bubbles inside of the AAO were removed under vacuum.

A typical synthesis process for TiO_2 is the hydrolysis of a precursor solution by adding water drop wise; however, a slow hydrolysis technique is required in this experiment to make thin and uniform walls of TiO_2 nanotubes. The details of the synthesis process and characterization of different TiO_2 thickness will be discussed in the next chapter, as well as their effects on photocatalytic activities. A larger size glassware than the one containing both the AAO template and the TBOT solution was prepared with 2 mL of water inside, and the small one was put inside of the large one and capped. Water vapor inside of the large glassware slowly hydrolyzed the TBOT inside of AAO pores. After 2.5 hours, the AAO templates were taken out and excess TiO_2 aggregation on the surface of the AAO was scraped off followed by rinsing with absolute ethanol and drying at 60 °C overnight.

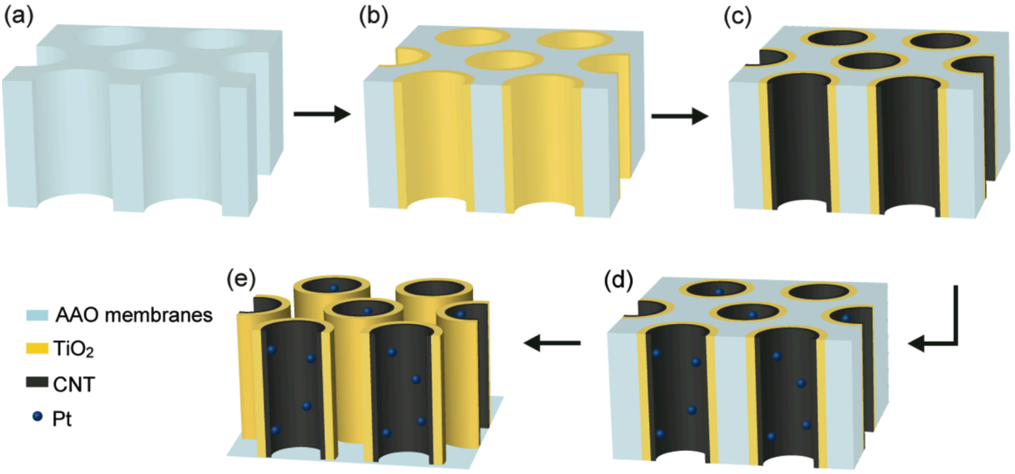

Figure 4.1 Schematic diagram of the fabrication process. (a) Anodic Aluminum Oxide (AAO) template. (b) TiO_2 deposition inside of AAO template by soaking the template to Titanium butoxide solution in water vapor. (c) Deposition of carbon layers by polymerization of glucose at 600 °C for 5h to get both graphitic layers and anatase TiO_2. (d) Deposition of Pt nanoparticles using H_2PtCl_6 solution with chemical reduction. (e) Removal of AAO template using 2M NaOH for 5h.

Synthesis of carbon nanotubes inside TiO_2-AAO

To make the carbon nanotubes, the amorphous TiO_2-AAO template was immersed in a 5 mL aqueous solution of 0.1 M glucose, and trapped air was removed under vacuum. After 1 hour, excess glucose on the surface was removed by careful scraping and then the sample was dried at 60 °C for 3 hours and at 180 °C for 3 hours. The glucose coating process was repeated twice. Pyrolysis of the glucose coated amorphous TiO_2-AAO template was carried out at 600 °C for 5 hours under an argon atmosphere to make anatase TiO_2 and graphitic layers at the same time. A pyrolysis temperature higher than

600 °C is required to make high quality graphitic layers; however, 600 °C was selected to maintain the anatase phase of TiO_2, which is reported to have higher photocatalytic activity than rutile [87] as well as to prevent coarsening of TiO_2 particle size. After pyrolysis, the surface of the sample was scraped carefully using a piece of soft polymer and washed off with absolute ethanol to remove impurities such as excess carbon aggregation before drying at 60 °C.

Deposition of Pt nanoparticles inside TiO_2-CNT-AAO

An aqueous solution of 10 mM H_2PtCl_6 was dropped on the prepared TiO_2-CNT-AAO and bubbles inside of pores were also removed by vacuum filtering. After 1 hour, the sample was taken of the H_2PtCl_6 solution and the surface was scraped to prevent excess Pt deposition on the surface, followed by drying at 60 °C. For chemical reduction, a sodium borohydride solution was prepared by mixing 40 mM $NaBH_4$ and 20 mM NaOH solution. To reduce the platinum, sodium borohydride solution was dropped into the sample followed by a vacuum filtering to remove bubbles inside, and this process was repeated two times. After 30 minutes, the sample was taken out and dried. The process of Pt deposition was repeated twice to deposit more Pt particles.

Removal of AAO templates

There were two ways to remove the AAO template and the one that was used depended on the application. To make TiO_2-CNT-Pt samples in powder form for studies of photo-deposition of metal oxide and metal, and a few other characterizations, TiO_2-CNT-Pt was liberated from AAO templates by soaking the samples in a 2 M NaOH solution for 5 hours with stirring at room temperature. After 5 hours, the sample was rinsed with DI water several times and filtered followed by drying. When the sample is needed in thin film form, it was attached to a glass holder to prohibit breakdown of the sample during dissolution of the AAO template. Then, the sample was treated with a 2M NaOH solution for 5 hours followed by neutralization until pH = 7.

4.2.2 Photocatalytic methylene blue degradation

The sample was put into a 4 ml aqueous solution of 0.02 mM Methylene Blue and then bubbles inside of the sample were removed by vacuum filtering. The suspension was stirred for 2 hours in the dark until adsorption-desorption equilibration was reached. The next steps of the experiment were described in chapter 3.

4.2.3 Photodeposition of metal oxide and metal on TiO_2-CNT-Pt

Photodeposition of MnO_x

Photodeposition of MnO_x on TiO_2-CNT-Pt was conducted in a 10 mM $MnSO_4$ solution with 10 mM $NaIO_3$ as an electron acceptor. 0.5 mg of TiO_2-CNT-Pt was immersed in 2 mL of $MnSO_4$ and $NaIO_3$ solution and exposed to visible light for 2 hours. A 300 W Hg lamp with a UV-filter and a water filter (IR filter) was used as the light source. After light irradiation, the sample was washed and centrifuged. If the hypothesis is supported, then during illumination, photo-generated holes remain on the outer surface of the TiO_2-CNT-Pt structure while electrons transfer to the inside of the tubes. Meanwhile, OH ions dissociated from water molecules are bound on the surface of TiO_2, and the adsorbed OH ions attract Mn^{2+} ions to make $Mn(OH)_2$. Then, the photo-generated holes on the TiO_2 surface make manganese oxide (MnO_x) from $Mn(OH)_2$ and finally MnO_x can be deposited on the outer surface of the TiO_2-CNT-Pt structure.

Photodeposition of Ag

Photodeposition of Ag on TiO_2-CNT-Pt was conducted in a 10 mM $AgNO_3$ solution uing a visible light exposure for 2 hours, in this case, water is the hole acceptor. A 300 W Hg lamp with a UV-filter and a water filter (IR filter) was also used as the light source. After light irradiation, the sample was washed and centrifuged. If the hypothesis is supported, then during light irradiation, electrons and holes are photo-generated, and electrons can transfer to Pt nanoparticles through carbon layers which can make faster charge transfer than without Pt. Ag^+ ions inside of a tube can meet electrons and make Ag nanoparticles inside of the tube.

4.2.4 Photoelectrochemical water splitting

Preparation of photoelectrodes

The TiO_2-CNT-Pt structure with the AAO template was attached to the Cu foil electrode with silver paste. After drying the silver paste at 60 °C, the specimen was soaked into 10 wt.% PVA solution followed by vacuum filtering several times to remove bubbles inside of nanotubes. After an overnight delay, the specimen in the PVA solutions was taken out and the surface was wiped off with a dried paper towel. A few minutes later, when the PVA solution on the surface is dried, the surface is wiped off again with a wet paper towel that is prepared using distilled water. After drying for a few hours, silver paste regions around the specimen were covered with epoxy and cured overnight to prevent the electrolyte from contacting the silver paste or copper electrode. Then, the AAO template was removed with 2M NaOH for 5 hours followed by repeated washing with distilled water. The TiO_2-CNT electrode was prepared using the same process.

Photoelectrochemical measurements.

The photoelectrochemical performance of these materials was investigated using a SP-200 potentiostat (Bio Logic Science Instrument) using a three electrodes system. All measurements were conducted using a saturated calomel reference electrode (SCE) and a platinum coil counter electrode. 1 M Na_2SO_4 was used an electrolyte and the scan rate was 10 mV/s. A 150 W Xenon lamp was used as the light source and the power density of the light was calibrated to 100 mW/cm^2 under white light and 73 mW/cm^2 under visible light. The results in this work are presented against SCE and the reversible hydrogen electrode (RHE) to compare the potential with water splitting levels. The conversion between potentials is calculated using the following relationship.

$$E\ (\text{vs. RHE}) = E\ (\text{vs. SCE}) + 0.244 + 0.059 \times \text{pH}$$

4.3 Results

4.3.1 Analysis of morphology and structure

Morphology and crystallinity

A scanning electron microscopy image of TiO_2-CNT-Pt reveals uniformly synthesized nanotubes with long-range order (Figure 4.2 (a)) and a higher magnification image shows around 200 nm diameter TiO_2-CNT-Pt nanotubes (Figure 4.2 (b)). Figure 4.2 (c) is a transmission electron microscopy image of TiO_2-CNT-Pt that represents very clear outer and inner wall surface with around 10 nm wall thickness as shown in Figure 4.2 (c) inset. Dark nanoparticles inside of the tube are platinum nanoparticles. A high resolution TEM image shows crystalline TiO_2, graphitic fringes, and Pt nanoparticles with a 5 nm diameter (Figure 4.2 (d)). The diffraction pattern (Figure 4.2 (d) inset) is for a TiO_2 wall region indicating well-synthesized polycrystalline anatase TiO_2. Higher resolution images of TiO_2 and Pt nanoparticles are shown in Figure 4.3.

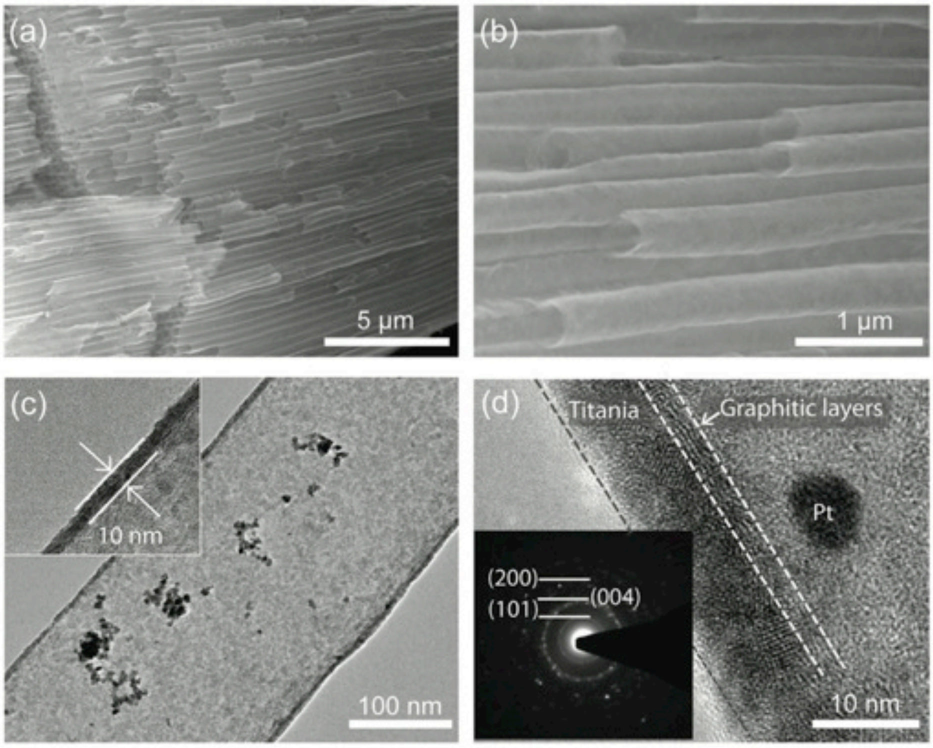

Figure 4.2 Morphologies and microstructure of pristine TiO_2-CNT-Pt. (a) SEM image of TiO_2-CNT-Pt bundles in low magnification. (b) SEM image of a region of (A) with a higher magnification. (c) TEM image of a TiO_2-CNT-Pt, the inset is an enlarged TEM image to show the wall thickness. (d) TEM image of a wall of TiO_2-CNT-Pt with local graphitic layers and a Pt nanoparticle, inset is a diffraction pattern of the TiO_2 wall.

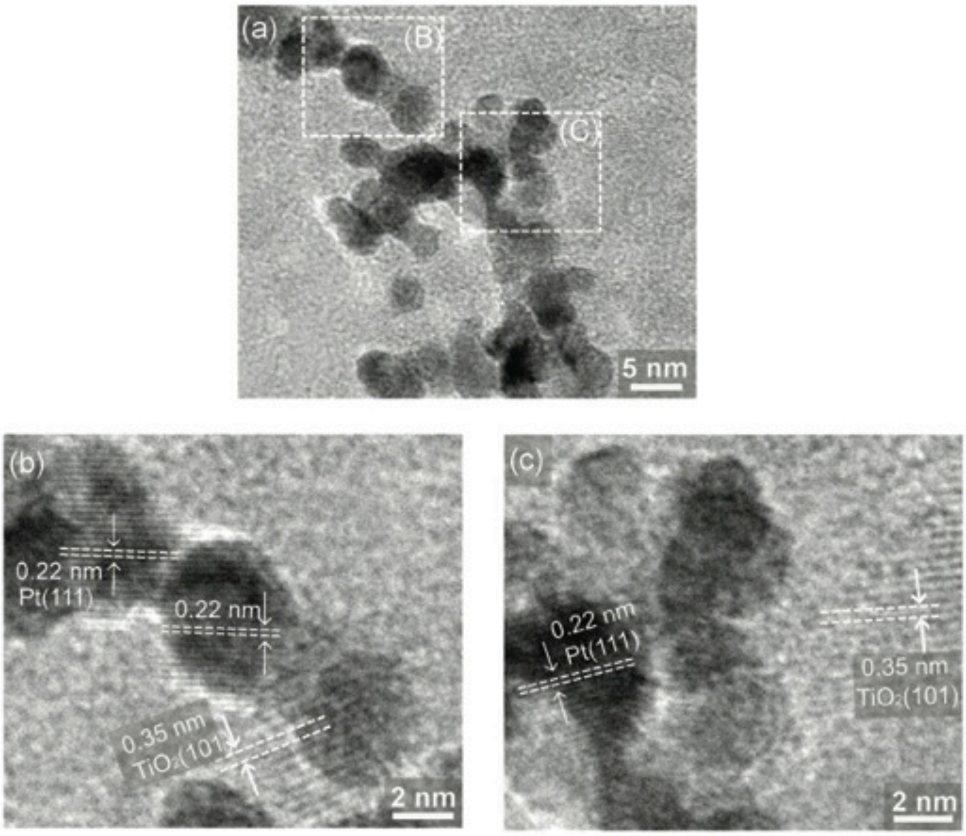

Figure 4.3 (a) TEM image of TiO_2-CNT-Pt to show TiO_2 and Pt nanoparticles. (b) (c) Higher magnification of the specific region in the image (a) to show lattice distances of anatase TiO_2 and Pt nanoparticles. The darker particles have 0.22 nm d-spacings that are consistent with Pt (111) and the planes in the light grey region have 0.35 nm d-spacings, consistent with TiO_2 (101).

Analysis of structure and phases

Raman spectroscopy was carried out to study the microstructure of the cells (Figure 4.4). Anatase TiO_2 as a reference was synthesized on an AAO template with the same precursor followed by annealing at 450 °C in air to make anatase TiO_2. The Raman spectrum of TiO_2-AAO shows a strong peak at 144.3 cm^{-1} corresponding to the E_g mode of anatase TiO_2 [183]. After annealing at 450 °C in air, amorphous TiO_2 crystallized as anatase TiO_2. The other three peaks at 395, 516 and 637 cm^{-1} are the B_{1g}, A_{1g} and B_{1g} modes of anatase TiO_2.

The Raman spectrum of TiO_2-CNT-Pt shows well-defined TiO_2 peaks and graphitic layers confirmed by the D and G modes, respectively. The strong peak at 151.0 cm^{-1}, assigned to the E_g mode of anatase TiO_2, was shifted by 7 cm^{-1} compared with that of pristine anatase TiO_2, which indicates a large decrease in the vibration energy of the crystal lattice due to an increased interaction between TiO_2 and carbon. The other three peaks at 395, 514 and 639 cm^{-1} are assigned to the B_{1g}, A_{1g} or B_{1g}, and E_g modes of anatase, respectively. The Raman peaks at 1317 and 1581 cm^{-1} correspond to the D and G-band, respectively.

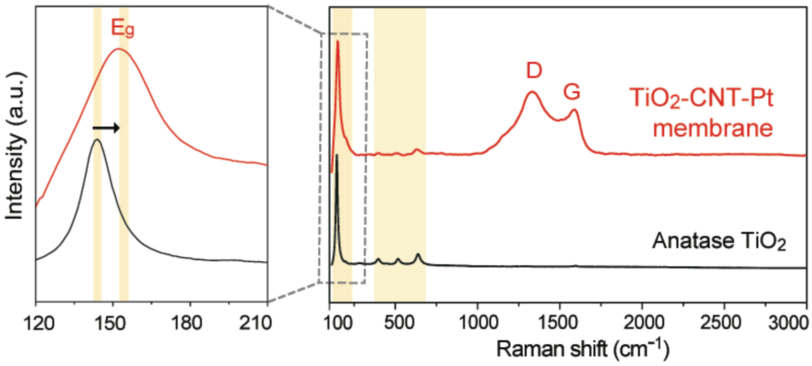

Figure 4.4 Raman spectroscopy measurement. Raman shift of TiO_2 E_g peak region (left) and whole spectrum [2] of TiO_2-CNT-Pt and anatase TiO_2.

X-ray photoelectron spectroscopy (XPS)

We further examined interactions between TiO_2 and CNTs by determining various bondings within TiO_2-CNT using XPS (Figure 4.5). The 1s core level spectrum of carbon (C) can be deconvolved into five peaks: the C=C peak at around 283.6 eV and the C–C peak at 284.7 eV were the dominant peaks arising from CNTs with comparatively smaller but still significant C–O peak at 286.6 eV (O ≡ oxygen), which suggests that some oxygen dissociated from titania and formed bonds with CNTs, along with Ti–C peak at 282.0 eV (Ti ≡ titanium) and Ti–O–C at 288.5 eV, further validating bonding between titania and CNTs. Signatures of these bondings were also present in the deconvolved 2p core level spectrum of Ti with Ti–O $2p_{3/2}$ and $2p_{1/2}$ peaks at 458.4 eV and 464.1 eV, respectively, as well as Ti–C peaks at 457.6 and 462.2 eV. Finally, the 1s core level spectrum of O can be fitted into two peaks of which one of the peaks at 530.8 eV can be attributed to Ti–O and the other peak at 532.6 eV can be attributed to C–O. Overall, the 1s core level spectrum of C and 2p core level spectrum of Ti established that TiO_2 formed bonds with CNTs.

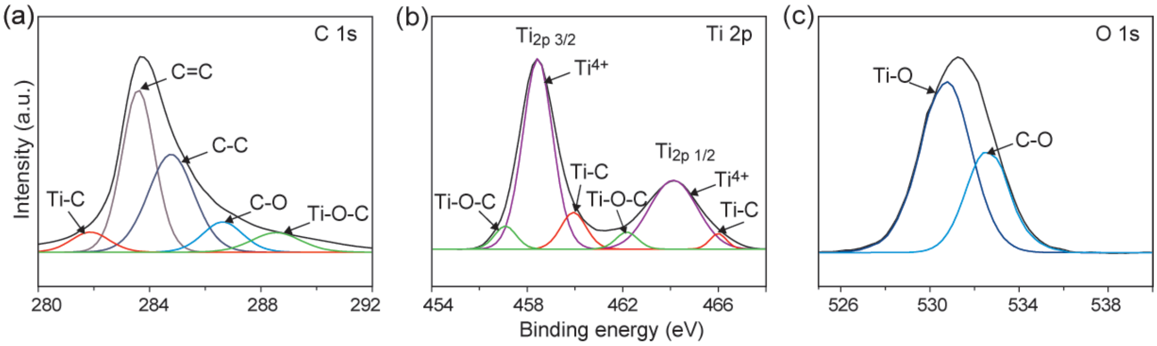

Figure 4.5. X-ray photoelectron spectroscopy (XPS) spectra from TiO_2-CNT for (a) 1s core level of carbon (C), (b) 2p core level of titanium (Ti), and (c) 1s core level of oxygen (O), suggesting Ti-C and Ti-O-C bonding between TiO_2 and CNTs.

Optical properties

The optical properties were investigated by UV-vis reflectance. Figure 4.6 shows the reflectance of the CNT, TiO_2-CNT, and TiO_2 samples. TiO_2 is prepared on AAO templates followed by annealing at 450 °C in air, and carbon is prepared by coating glucose on the AAO templates followed by pyrolysis at 600 °C under argon. The bandgaps of the specimens are calculated by using Kubelka-Munk function, $F(R) = (1-R)^2/2R$, and Tauc-plot, $F(R)h\nu = A(h\nu-E_g)^2$. It can be seen that TiO_2-CNT has a lower bandgap than anatase TiO_2. Moreover, despite the absence of a distinct bandgap edge, the results shows enhanced visible light response compared to anatase TiO_2.

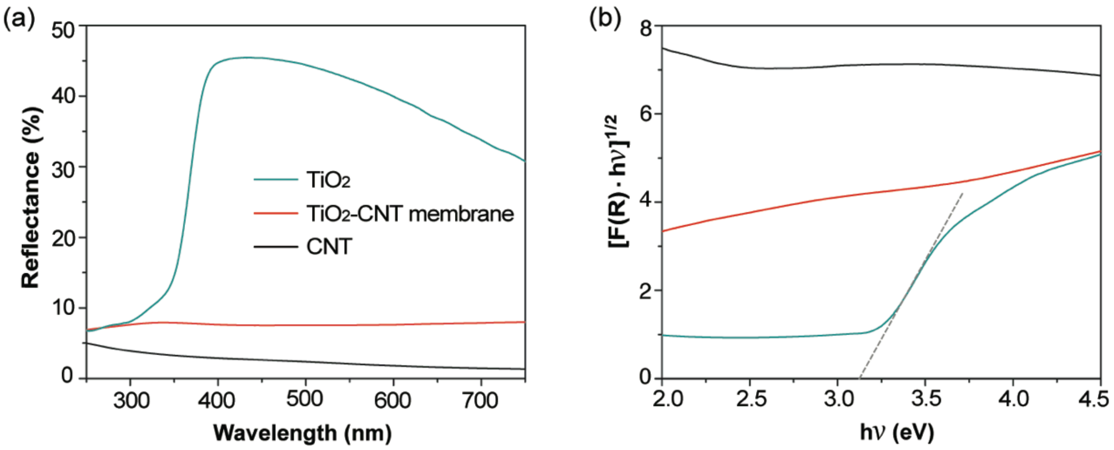

Figure 4.6 (a) Ultraviolet-visible reflectance spectra of CNT, TiO_2-CNT, and TiO_2. (b) Tauc plot of $F(R)h\nu$ as a function of photon energy($h\nu$) using a Kubelka-Munk function of $F(R)=(1-R)^2/2R$.

4.3.2 Photocatalytic properties

Photocatalytic Methylene Blue degradation

The photodegradation of methylene blue was investigated to measure the photocatalytic activity [184, 185]. The photocatalytic activity for methylene blue degradation was obtained by calculating the change in the concentration (C/C_0) using the measured absorbance at 665 nm [186]. C_0 and C denote initial concentration of methylene blue and the concentration at each time, respectively. The photocatalytic activity of TiO_2-CNT-Pt was compared with blank (only methylene blue), TiO_2 P25 that is a commercially available TiO_2 as a reference, and TiO_2-CNT without Pt nanoparticles (Figure 4.7). The methylene blue degradation experiment was conducted at least three times for reliability and error bars were inserted by calculating the standard deviation. Blank (methylene blue) and reference TiO_2 P25 decompose methylene blue slightly but the amount was negligible.

The degradation rate was enhanced with TiO_2-CNT that has activity under the visible light. In addition, TiO_2-CNT-Pt shows higher photocatalytic activity than TiO_2-CNT. The rate constant, k, of TiO_2-CNT-Pt is 7×10^{-3} min^{-1}, k of TiO_2-CNT is 4.8×10^{-3} min^{-1}, k of the reference TiO_2 is 0.4×10^{-3} min^{-1}, and k of methylene blue is 0.3×10^{-3} min^{-1}. The rate constant of TiO_2-CNT-Pt was 1.43 times higher than that of TiO_2-CNT that was 12.25 times than that of TiO_2 P25. To compare how many μmol of methylene blue were decomposed by a unit mass of the photocatalyst per unit time, a unit of μmol/h/g was used in the work. To calculate the degradation rate, we assume that all methylene blue molecules that adsorbed on the photocatalyst were decomposed and C_0 is the initial concentration. The degradation amount of methylene blue per unit mass of the photocatalyst and unit time of TiO_2-CNT-Pt was 173 μmol/h/g that is 1.3 times higher than that of TiO_2-CNT, 133μmol/h/g. The time profile of the methylene blue absorbance spectrum of TiO_2-CNT-Pt under visible light irradiation shows a decrease in concentration of methylene blue every 30 minutes (Figure 4.8 (a)). The absorption intensity decreased with time indicating methylene blue degradation by TiO_2-CNT-Pt under visible light. Figure 4.8 (b) shows the recycle properties of photocatalytic methylene blue degradation of TiO_2-CNT-Pt. After one methylene blue degradation experiment, the TiO_2-CNT-Pt was washed and put in distilled water overnight in the dark, and the photo-degradation of the methylene blue experiment with the sample was conducted again. The reduced degradation rate during the recycle test was negligible, showing that the catalyst is reusable.

Table 4.1 shows data comparing TiO_2-CNT-Pt and TiO_2-CNT with other recently developed photocatalysts in photocatalytic methylene blue degradation experiments. Most of them used different methylene blue concentrations, different power and sources of light, and different adsorption-desorption equilibration times in the dark, which makes it difficult to compare the final rates. Nevertheless, TiO_2-CNT-Pt shows the highest photocatalytic activity among those photocatalysts. To calculate the degradation rate of other works, we assume that C_0 is the initial concentration of dye that the authors mentioned and the all dye molecules adsorbed on the photocatalyst were decomposed.

Before light irradiation, all of the methylene blue degradation experiments in this work were conducted after 2 hours in the dark to obtain the adsorption-desorption equilibration of methylene blue with the surface. The changes in the methylene blue concentration during the 2 hours in the dark are shown in the Figure 4.9, which show adsorption-desorption equilibration was reached within 2 hours for both TiO_2-CNT and TiO_2-CNT-Pt. Methylene blue was also photocatalytically degraded by TiO_2-CNT and TiO_2-CNT-Pt under white light including ultraviolet and visible light to compare with the degradation rate in the visible light experiment (Figure 4.10). The results show photocatalytic degradation rate of both TiO_2-CNT and TiO_2-CNT-Pt under white light was higher than that under visible light.

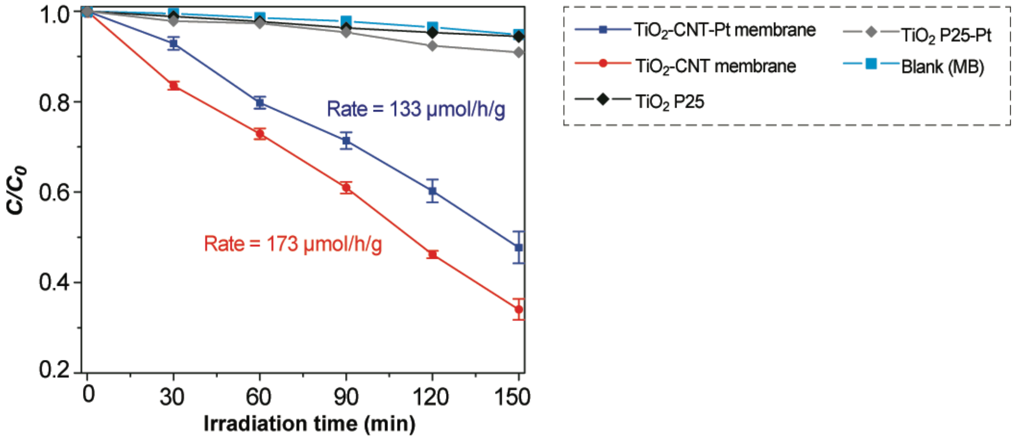

Figure 4.7 Photocatalytic methylene blue degradation of TiO_2-CNT-Pt (TCP), TiO_2-CNT (TC), TiO_2 P25 as a reference, and blank (methylene blue) under visible light irradiation (λ > 420 nm). The concentration change of methylene blue was calculated by comparison of absorbance intensity (C/C_0) at 665 nm. The reaction rate of methylene blue degradation per unit mass of photocatalyst and unit time of TiO_2-CNT-Pt is 173 μmol/h/g and that of TiO_2-CNT is 133 μmol/h/g.

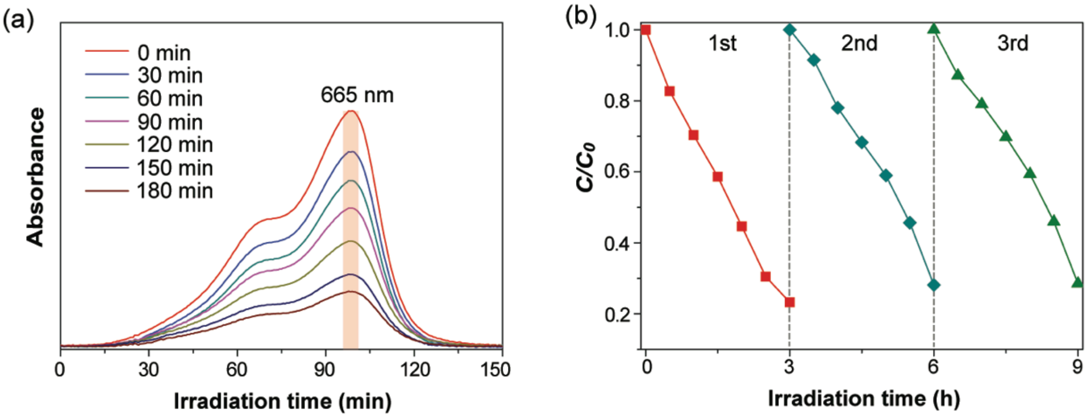

Figure 4.8. (a) Time profile of absorbance spectrum of methylene blue at every 30 minutes indicating decrease of absorbance as time goes by. (b) Recycle properties of photocatalytic MB degradation of TiO_2-CNT-Pt. After one set of MB degradation, TiO_2-CNT-Pt was washed and put in DI water overnight in the dark, and photo-degradation of MB experiment with the sample was conducted again.

Table 4.1 Comparison data of photocatalytic dye degradation

Photocatalyst composites	Concentration of MB	Power of light source	Dark equilibrium time	MB degradation rate	Ref.
TiO_2-CNT-Pt (This work)	0.02 mM	300 W	2 hours	173 μmol/h/g	This work
TiO_2-CNT (This work)	0.02 mM	300 W	2 hours	133 μmol/h/g	This work
TiO_2-graphene	0.027 mM	400 W	1 hour	25 μmol/h/g	[187]
TiO_{2-x}/B-graphene	0.06 mM	500 W	1 hour	12 μmol/h/g	[188]
P25-graphene	0.027 mM	500 W	10 min.	24 μmol/h/g	[189]
TiO_2-reduced graphene oxide	0.03 mM	1000 W	10 min.	27 μmol/h/g	[190]
TiO_2-MWCNT	0.06 mM	-	2 hours	98 μmol/h/g	[191]
P25-MWCNT	0.027 mM	500 W	10 min.	20 μmol/h/g	[189]
TiO_2-carbon dots	0.15 mM	1000 W	Overnight	38 μmol/h/g	[127]
Mesoporous FeS_2	0.1 mM	300 W	-	65 μmol/h/g	[192]
Mesoporous CoS_2	0.1 mM	300 W	-	63 μmol/h/g	[192]

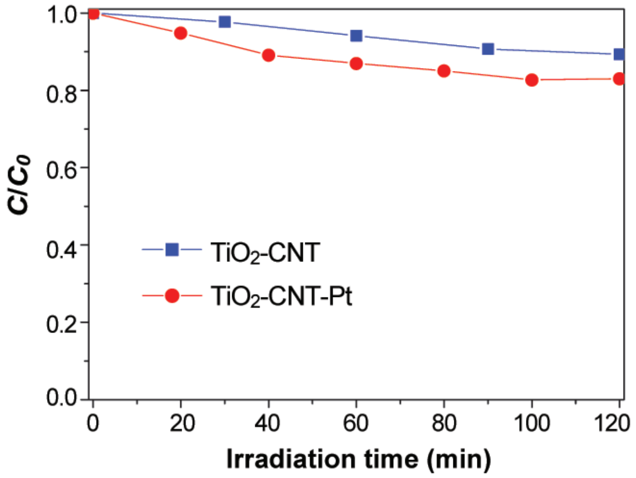

Figure 4.9. Adsorption-desorption equilibration of methylene blue with TiO_2-CNT and TiO_2-CNT-Pt in the dark for 2 hours. All of the methylene blue degradation experiment in this work was conducted after 2 hours equilibrium in the dark.

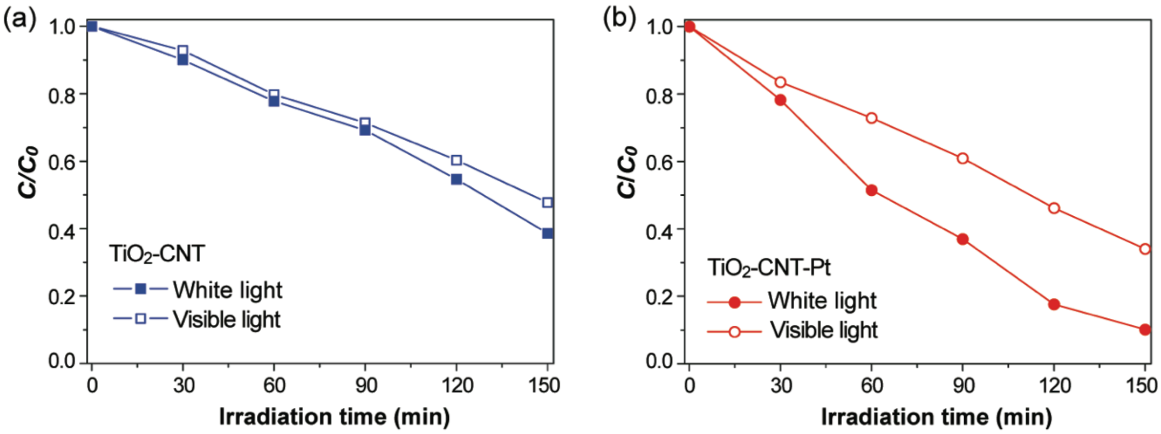

Figure 4.10. (a) Photocatalytic methylene blue degradation of TiO_2-CNT under white light to compare with visible light experiment. (b) Photocatalytic methylene blue degradation of TiO_2-CNT-Pt under white light and visible light irradiation.

4.3.3 Verification of oxidation and reduction sites

The crucial functionality of the photoelectrochemical cells is to spatially separate oxidation and reduction sites. To verify the separation of photo-generated electron-hole pairs and their different reaction sites, the photo-deposition of MnO_x and Ag was used. MnO_x was deposited by photo-deposition using $MnSO_4$ as a precursor and $NaIO_3$ as an electron scavenger under visible light. Figure 4.11 (a) shows a TEM image of MnO_x covered TiO_2-CNT-Pt after the reaction. The outside of TiO_2-CNT-Pt is composed of thin layers with sharp flakes that are definitely different from the pristine TiO_2-CNT-Pt that has clear and neat outer wall surfaces. Higher magnification images displayed in Figure 4.11 (b) also shows the unique shape of the MnO_x region outside a wall and a HRTEM image of MnO_x region is shown at Figure 4.11 (c).

The proposed mechanism of photo-deposition of MnO_x is shown in Figure 4.11 (d). During illumination, photo-generated holes remain on the outer surface of a TiO_2-CNT-Pt while electrons transfer to the inside of the TiO_2-CNT-Pt. Meanwhile, OH^- ions dissociated from water molecules are bound on the surface of TiO_2, and the adsorbed OH^- ions attract Mn^{2+} ions to make $Mn(OH)_2$ outside of a tube. Then, the photo-generated holes on the TiO_2 surface make manganese oxide (MnO_x) from $Mn(OH)_2$ and finally MnO_x can be deposited on the outer surface of a TiO_2-CNT-Pt. From the experiment, it was demonstrated that MnO_x was deposited outside of TiO_2-CNT-Pt by showing a different surface morphology compared with the pristine TiO_2-CNT-Pt.

Table 4.2 shows the results of an elemental analysis of MnO_x-TiO_2-CNT-Pt after different reaction times. The amount of Mn is 7.88 wt.% after a 30 minute reaction and 8.68 wt.% after a 3 hour reaction, which confirms deposition of MnO_x and suggests that the reaction is fastest in the initial 30 minutes. Since $MnSO_4$ was used as a precursor and

$NaIO_3$ was used as an electron accepter, negligible amounts of remaining S, Na, and I indicate that Mn is definitely deposited while others are only adsorbed on surface in small quantities.

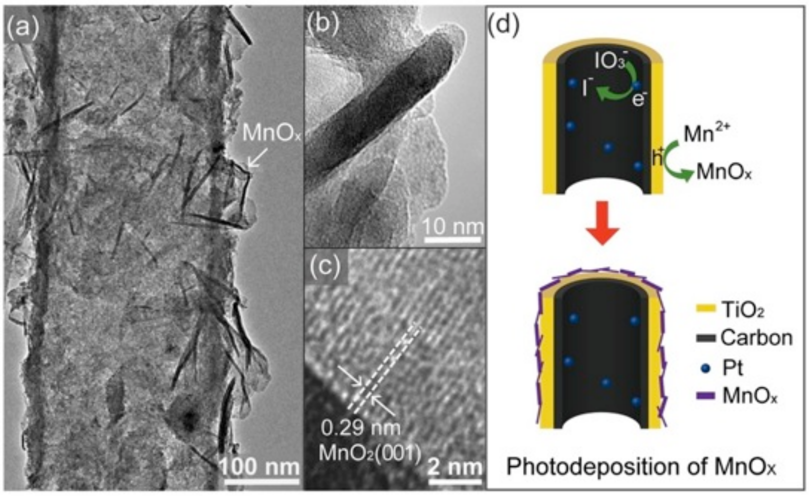

Figure 4.11 Verification of oxidation sites by photo-deposition of metal oxide. (a) TEM image of MnO_x deposited TiO_2-CNT-Pt at a low magnification. (b) TEM image of MnO_x on an outside of TiO_2 wall. (c) HRTEM image of a region in the image (b) to show MnO_x lattice. (d) Schematic diagram of the proposed mechanism for photo-deposition of MnO_x on the outside of TiO_2-CNT-Pt.

Table 4.2 Elemental analysis of Mn and related ions in photo-deposited MnO_x-TiO_2-CNT-Pt depending on reaction times. Although $MnSO_4$ was used as a precursor and $NaIO_3$ was used as an electron accepter, negligible amounts of S, Na, and I remain, indicating that Mn is in the solid deposit while others elements were washed away.

Reaction time	Elements			
	Mn	S	Na	I
30 minutes	7.88 wt.%	0	0.2 wt.%	0
3 hours	8.68 wt.%	0.34 wt.%	0.06 wt.%	0.08 wt.%

The locations of the reduction sites were verified through the photo-deposition of Ag nanoparticles on TiO_2-CNT-Pt. Ag nanoparticles were deposited using $AgNO_3$ as a precursor under visible light. After deposition, most of Ag nanoparticles are located inside of the TiO_2-CNT-Pt structure, as shown in Figure 4.12 (a). A higher magnification image of an Ag nanoparticle shows that its diameter is about 20 nm (Figure 4.12 (b)). Based on images of pristine TiO_2-CNT-Pt, the small nanoparticles are Pt and the larger particles that appear after the photochemical reaction are Ag. Pt nanoparticles with 3-5 nm in size while the Ag particles are 20 nm and easily distinguished. A HRTEM image of an Ag particle is shown in Figure 4.12 (c), indicating a lattice parameter of 0.239 nm, consistent with the spacing between Ag (111) planes.

The proposed mechanism of photo-deposition of Ag nanoparticles is shown in Figure 4.12 (d). During light irradiation, photo-generated electrons transfer to a CNT and/or Pt nanoparticles. Ag^+ ions inside of a tube can meet electrons at the surface of a

CNT and/or Pt nanoparticles, and make Ag nanoparticles inside of the tube. On the other hand, on the outer surface of the tube, there are no electrons; as a result, no Ag is found on the outer surface. Table 4.3 shows the results of elemental of Ag-TiO_2-CNT-Pt after the reaction for different reaction times. The amount of Ag after 30 minutes and 3 hours are about the same, within expected uncertainty.

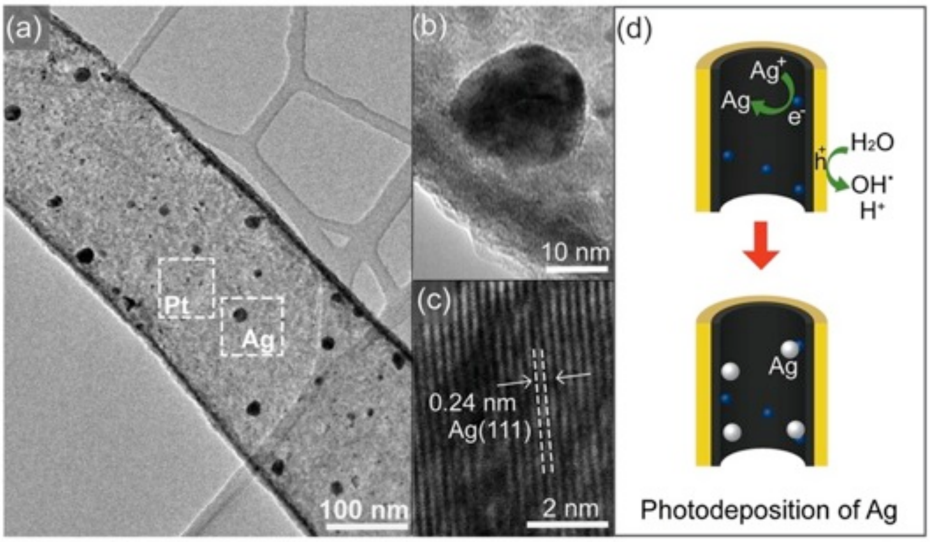

Figure 4.12 Verification of reduction sites by photo-deposition of Ag particles. (a) TEM image of Ag deposited TiO_2-CNT-Pt. (b) TEM image of an Ag particle in a region of image (a). (c) HRTEM image of Ag. (d) Schematic diagram of proposed mechanism for photo-deposition of Ag particles on the inside of TiO_2-CNT-Pt.

Table 4.3 Elemental analysis of Ag in photo-deposited Ag-TiO_2-CNT-Pt at three reaction times. The amount of Ag after 30 minutes and 3 hours are about the same, within expected uncertainty. The results suggest that most of the Ag accumulated in the first five minutes.

Concentration of $AgNO_3$	Reaction time		
	5 minutes	30 minutes	3 hours
1 mM	8.68 wt.%	10.34 wt.%	10.22 wt.%

The TEM images and EDX images suggest that Ag particles are deposited inside of TiO_2-CNT-Pt; however, TEM is a transmission technique, so it is difficult to be certain which side of the carbon they are on. To get more reliable information on the location of the Ag particles, more TEM images were recorded and are shown in Figure 4.13. TEM images of TiO_2-CNT-Pt walls at different spots from (a) to (f) show that Ag particles are definitely deposited inside the tubes. Images of (g) and (h) also show deposition of Ag particles within the tubes. Figure 4.13 (i) is a region that has Ag particles located outside. In the case when there is a pinhole in the wall, charge carriers can be mixed and Ag^+ ions can meet electrons on the outside. The pinhole could be generated during the experimental process due to non-uniform deposition of TiO_2 by the sol-gel method, or walls might be broken due to the vigorous stirring during photodeposition.

Another case of Ag particle deposition on the outside of the tube is shown in Figure 4.13 (j). During removal of the AAO template, there are imperfectly separated walls that have some impurities, which causes mixing of charge carriers allows Ag to be deposited on the outside of TiO_2-CNT-Pt. In other words, Ag particles are not exactly seated on a TiO_2 wall, but seated on detached carbon layers. Figure 4.13 (k) is the whole image including images from (g) to (j) indicating perfect walls of TiO_2-CNT-Pt can have Ag particles deposited inside of a tube, while in the case of non-perfect walls, Ag could be deposited on the outside of tubes at pinholes or impurities, but not directly on TiO_2. Based on the observation of 122 Ag particles on random walls, it was determined that 90.8 % of the Ag particles are inside the tubes and 9.2 % of the Ag particles are outside.

Further verification of how many pinholes exist and how much they can affect the photocatalytic activity is shown in Figure 4.14. Photocatalytic methylene blue degradation of TiO_2-CNT before removal of the AAO templates and TiO_2-CNT-Pt with the AAO templates is removed were low compared with TiO_2-CNT and TiO_2-CNT-Pt after the AAO template was removed. The result implies that TiO_2 is located only on the outside and the oxidation and reduction sites are separated almost perfectly.

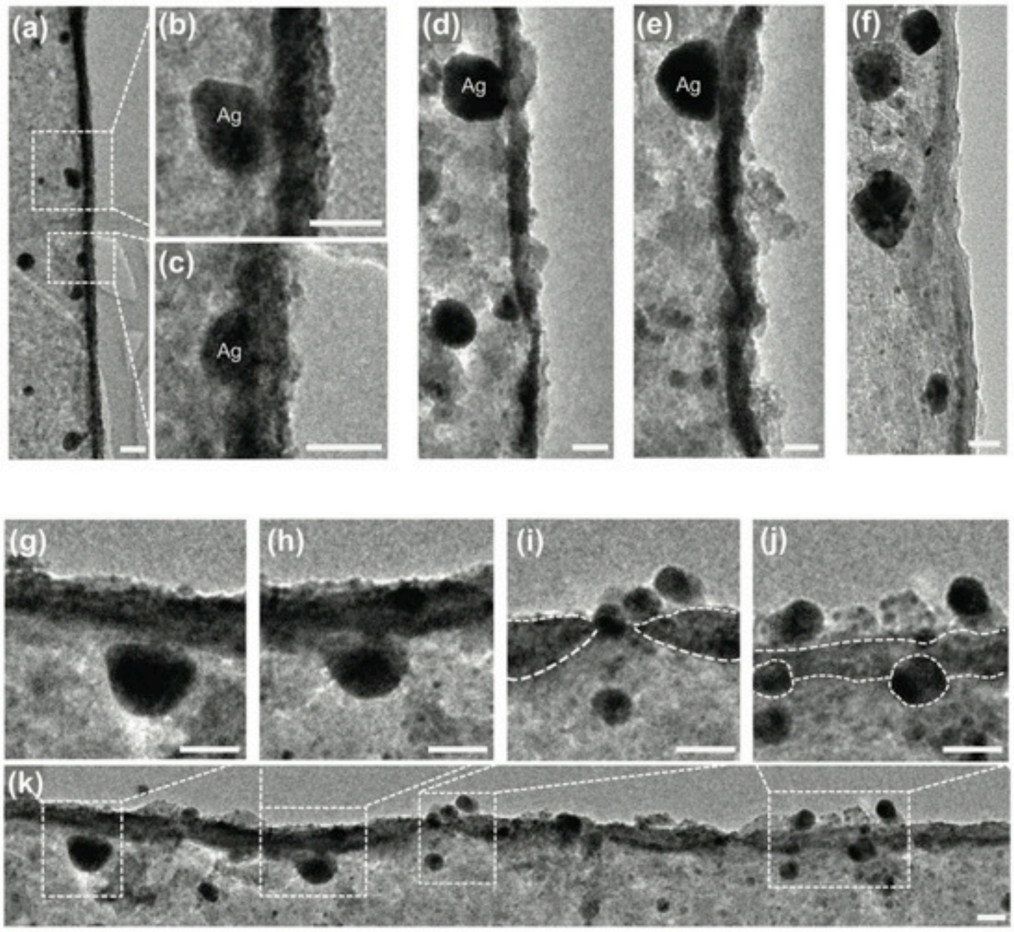

Figure 4.13 Photo-deposited Ag particles on different walls of TiO_2-CNT-Pt. (a)-(f) TEM images of TiO_2-CNT-Pt walls at different spots to show that Ag particles are deposited inside the tubes. (g-h) TEM images to show Ag particles are definitely located inside with a thick wall of TiO_2-CNT-Pt. (I) A region that has Ag particles located outside. In the case when there is a pinhole of the wall, charge carriers can be mixed and Ag^+ ions can meet electrons outside of tubes. (j) During removal of AAO template, there would be not perfectly separated walls such that have some impurities, which causes mixing in charge carriers and Ag deposition outside of TiO_2-CNT-Pt. (k) Whole image including images (g)-(j). Calculated percentage of Ag particle location by counting 122 Ag particles in random walls is that 90.8 % of Ag particles are inside of tubes and 9.8 % of Ag particles are outside.

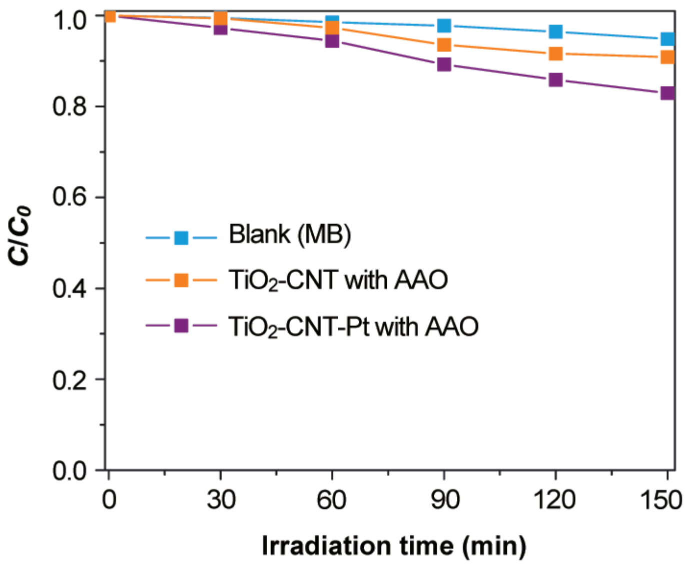

Figure 4.14 Photocatalytic methylene blue degradation of TiO_2-CNT with AAO templates and TiO_2-CNT-Pt with AAO templates under visible light to investigate the degree of separation of the oxidation and reduction sites in the structure. The degradation amounts of methylene blue of the both samples with AAO templates were too low to be compared with those without AAO templates. The result implies that TiO_2 was located only outside and the oxidation and reduction sites are separated almost perfectly.

4.3.4 Photoelectrochemical water splitting

The photoelectrochemical properties were examined in 1M Na_2SO_4 under both white and visible light. Figure 4.15 (a) shows delta photocurrent-potential (ΔJ-V) curves of water oxidation with TiO_2-CNT-Pt using a scan rate of 10 mV/s. The inside of the TiO_2-CNT-Pt nanotubes is filled with a polymer, PVA, to insulate the surface of the carbon and Pt from the electrolyte. The delta photocurrent is the measured photocurrent after subtracting the dark current. TiO_2-CNT-Pt under white light shows high photocurrent below 1.23 V versus reversible hydrogen electrode (RHE). Under visible light, the photocurrent is less than that under white light but it is still a high value enough to demonstrate photoelectrochemical activity of TiO_2-CNT-Pt. Figure 4.15 (b) shows the applied bias photon-to current efficiency (ABPE) of TiO_2-CNT-Pt under both white and visible light calculated by the ΔJ-V curves of Figure 4.15 (a). At 0.8 V versus RHE, the ABPE shows maxima of 1.45 % under white light and 0.83 % under visible light.

The original data for Figure 4.15 (a), including the dark current, are shown in Figure 4.16. Although the dark current is greater than zero, photocurrent after subtracting the dark current is still significant. Figure 4.16 shows the photocurrent from a TiO_2-CNT electrode prepared using the same method. Under white light, TiO_2-CNT shows an earlier onset potential and a higher photocurrent than TiO_2-CNT-Pt; however, the photocurrent decreases above 0.8 V, while that of TiO_2-CNT-Pt continues to increase.

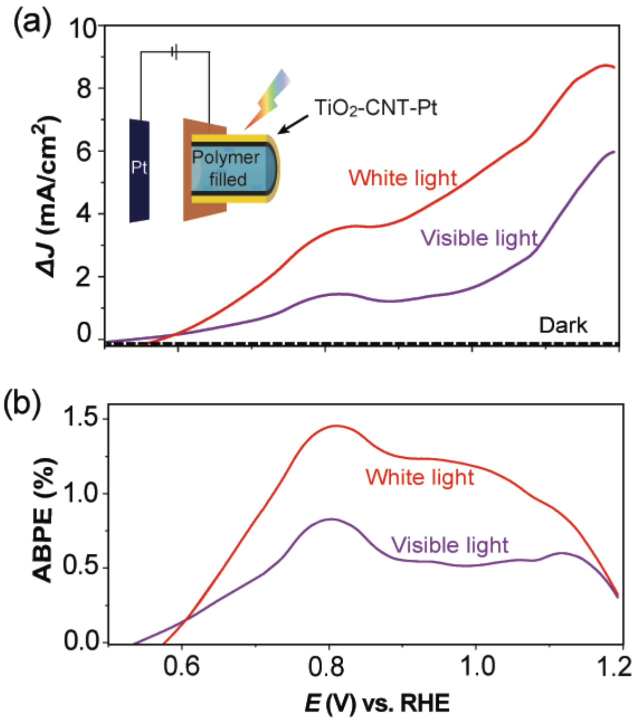

Figure 4.15 Photoelectrochemical properties of TiO_2-CNT-Pt. (a) ***Δ****J*-V curve of TiO_2-CNT-Pt measured in 1M Na_2SO_4 electrolytes under visible light and white light (scan rate, 10 mV/s). ***Δ****J* is the photocurrent after subtracting the dark current. (b) The applied bias photon-to-current efficiency (ABPE) of TiO_2-CNT-Pt obtained by a three-electrode system.

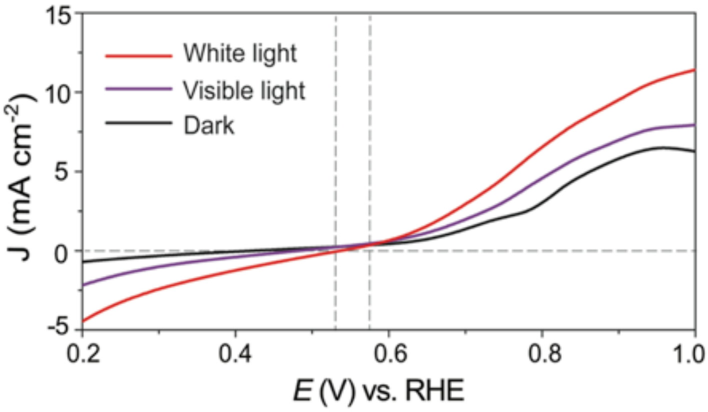

Figure 4.16 J-V curve of TiO_2-CNT-Pt including dark current. The photocurrents are original result of Figure 4.15 before subtracting dark current. The experimental conditions are the same with Figure 4.15.

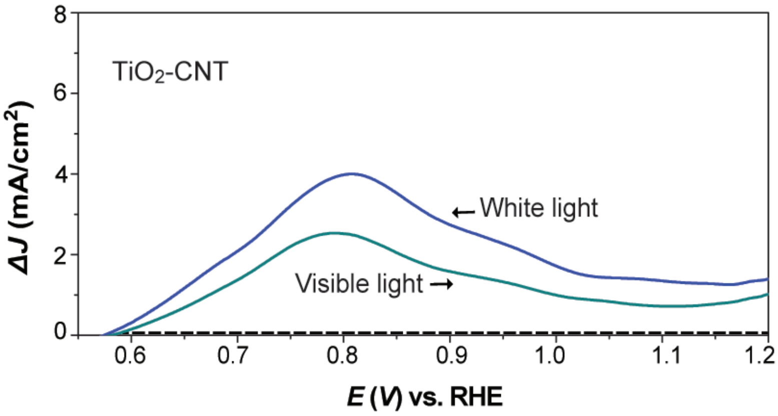

Figure 4.16 ***Δ***J-V curve of TiO_2-CNT measured in 1M Na_2SO_4 electrolytes under visible light and white light (scan rate, 10 mV/s).

4.4 Discussion

4.4.1. Analysis in morphology and structure

The photoelectrochemical cells of TiO_2-CNT-Pt were uniformly synthesized with long-range order and 200 nm diameters as shown in the scanning electron microscopy images in Figure 4.2 (a) and (b). In addition, transmission electron microscopy images show that the TiO_2-CNT-Pt structure wall thicknesses of about 10 nm with very clear outer and inner wall surface and platinum nanoparticles with a 5 nm diameter located on the inside of the tubes. (Figure 4.2 (c) and (d). Graphitic fringes inside of the TiO_2 walls are observed, implying that some regions have crystalline carbon layers even though the other regions are composed of amorphous carbon.

Raman spectroscopy was used to study the microstructure of the membrane. The strongest peak corresponds to the E_g mode of anatase TiO_2 and confirms that anatase TiO_2 was formed with long-range order. In the case of TiO_2-CNT, the lowest peak assigned to the E_g mode of anatase TiO_2 was shifted by 7 cm^{-1} compared with that of pristine TiO_2. The Raman spectrum of TiO_2-CNT shows D and G modes, confirming the formation of graphitic layers. The D-band indicates disordered carbon (breathing mode of k-point phonons of A_{1g} symmetry) and the G-band indicates graphitic carbon (the first order scattering of the E_{2g} phonons) [193].

Improvement in visible light absorption by the TiO_2 is consistent with the Raman spectroscopy results. It has been reported that changes in the Raman spectra can be attributed to non-stoichiometry, phonon confinement, and surface pressure [194, 195]. In the case of TiO_2-CNT, the non-stoichiometry effect could be induced when pyrolysis was carried out to make crystalline TiO_2 and graphitic layer under argon atmosphere. In addition, interaction between TiO_2 and CNT at the interface could affect the change in the vibrational mode of TiO_2 lattice inducing Raman peak shift as well as band gap narrowing. We further examined interactions between TiO_2 and CNTs by determining various bondings within TiO_2-CNT using XPS. There are significant C–O peak, which suggests that some oxygen dissociated from titania and formed bonds with CNTs, along with Ti–C peak and Ti–O–C, further validating bonding between titania and CNTs. Signatures of these bondings were also present in Ti–O and C–O peaks. The XPS results could support the significant bonding between TiO_2 and CNTs, which affect the Raman shift as well as band gap narrowing of TiO_2. Specifically, the interaction between TiO_2 and carbon can give rise to a new energy level in the TiO_2 band gap [183], which makes it possible for photo-excited electrons transfer to carbon [19, 191]. The remaining holes in the TiO_2 can decompose organic material on the surface. When glucose transforms to graphitic layers, they have π electrons which can bond with titanium atoms during the pyrolysis process [187, 189]. Thus, the band gap narrowing of TiO_2 may occur through the interaction of titanium atoms on the surface of TiO_2 with π electrons of carbon during crystallization and induces visible light absorption.

4.4.2 Photocatalytic properties

The bandgap of pristine TiO_2 is around 3.2 eV; therefore, TiO_2 does not absorb visible light. However, by interacting with graphitic layers, the bandgap of TiO_2 was narrowed, inducing visible light response. The bandgap narrowing of TiO_2 makes it possible for electrons in the valence band to be excited to the conduction band and transferred through the carbon layers to platinum particles. The carbon layer can promote faster charge transfer from TiO_2 to carbon layer than the case of only TiO_2 without any carbon layer, which accelerates degradation of methylene blue. That is why the photocatalytic activity of TiO_2-CNT-Pt was enhanced compared to that of TiO_2-CNT, TiO_2 P25, and the blank as shown in Figure 4.7. The rate constant, k, that is commonly used in the methylene blue degradation field is $\ln(C/C_0) = k$. The k of TiO_2-CNT-Pt was 7×10^{-3} min^{-1} which is 1.43 times higher than that of TiO_2-CNT.

However, the problem of the rate constant is that it is only related to degradation time and does not reflect the effects of the sample mass or methylene blue concentration. Moreover, there is no standard for the mass of the photocatalyst verses the concentration of methylene blue, which makes the two parameters inconsistent in most of studies. Thus, a new approach is needed to make a more exact comparison between the degradation rates reported by different groups. The unit of μmol/h/g is introduced in the work indicating how many μmol of methylene blue were decomposed by a unit mass of the photocatalyst per unit time. This unit for photocatalytic degradation of dyes has never been used, but it will be a better method to compare the results in the field. The amount of methylene blue degraded per unit mass of the photocatalyst and unit time shows that the rate of TiO_2-CNT-Pt was 173 μmol/h/g that is 1.3 times higher than that of TiO_2-CNT, 133 μmol/h/g. In addition to the charge separation that reduces the recombination rate of electron-hole pairs, the TiO_2-CNT-Pt structure can separate oxidation and reduction species via spatially separated channels. The outside of the carbon nanotubes consists of TiO_2 as an oxidation site and the inside of the carbon nanotubes consists of platinum particles as a reduction site, which also leads to improved photocatalytic activity by hindering backward reaction of the products and intermediates. When one compares the photodegradation rates of methylene blue with various carbon-TiO_2 hybrids and other photocatalysts, the TiO_2-CNT-Pt and TiO_2-CNT materials described in this work show the highest reaction rate under visible light irradiation.

The enhanced photocatalytic activities are also caused by the unique structure of the TiO_2-CNT-Pt that has spatially separated oxidation and reduction sites. In the TiO_2-CNT-Pt structure, photo-excited electrons from the surface of TiO_2 can transfer through a carbon nanotube to a platinum particle that is located inside of the carbon nanotube, which separates the charge carriers as well as the intermediates and products. On the other hand, if platinum particles are on the surface of TiO_2, photo-excited electrons can transfer to platinum particles located on the TiO_2 directly. In that case, the charge separation would be fast; however, the oxidation and reduction parts are not spatially separated. Thus, the unique structure of the TiO_2-CNT-Pt with a strong interaction between the TiO_2 and carbon nanotubes contributed to efficient photocatalysis similar to what is found in a photoelectrochemical cell.

4.4.3. Verification of oxidation and reduction sites

To verify the spatial separation of oxidation and reduction sites in the photoelectrochemical cells, MnO_x and Ag were photo-deposited. MnO_x was deposited on the outside of the TiO_2-CNT-Pt as shown in Figure 4.11. During light irradiation, photo-generated holes on the TiO_2 surface can attack hydroxyl ions which are dissociated from water molecules and bound on the TiO_2 surface. Then the adsorbed hydroxyl ions can make $Mn(OH)_2$ by bonding with Mn^{2+} ions while photo-generated electrons are transferred to Pt particles through carbon nanotubes. Then, $Mn(OH)_2$ can meet the photo-generated holes on the TiO_2 surface and can be finally transformed to manganese oxide (MnO_x) which is deposited on the outer surface of a TiO_2-CNT-Pt. Ag was photo-deposited on TiO_2-CNT-Pt to verify the location of the reduction sites. Ag particles with around 20 nm diameters are deposited inside of the TiO_2-CNT-Pt nanotubes and the size and morphology is quite distinct from Pt nanoparticles with 3-5 nm sizes. Under visible light, photo-generated electrons could transfer to CNTs and/or Pt nanoparticles, and meet Ag^+ ions inside of a tube to make reduced Ag. Since we analyzed the results via two-dimensional TEM images of the three-dimensional nanotubes, even though some of Ag particles seemed to be located on a Pt nanoparticle, we could not precisely figure out whether an Ag particle was located on a Pt nanoparticle or on the surface of CNTs. Nevertheless, the experiments demonstrate the separation of charge carriers and their transfer to the two different reaction sites, outside and inside the nanotubes. Moreover, it is also shown that outside of the nanotubes is the oxidation site and inside of the nanotubes is the reduction site.

Photo-degradation of methylene blue of TiO_2-CNT-Pt with AAO templates shows separation of the oxidation and reduction sites with negligible pinholes between TiO_2 and carbon nanotubes. After the synthesis of TiO_2 on the AAO template, carbon layers are deposited on the inside of the TiO_2-AAO template. During this process, if a pinhole exists between the TiO_2 and carbon, and some of TiO_2 forms within the carbon layers, it would be possible that e-h pairs are photo-generated on the TiO_2 inside the tubes causing decomposition of methylene blue. However, when TiO_2 is located only on the outside of the carbon layers, most of the TiO_2 surface is covered with AAO, and e-h pairs cannot be generated because light is blocked and methylene blue is not decomposed. Even if some of the light can penetrate to the TiO_2 and some e-h pairs are photo-generated, holes in the TiO_2 cannot migrate anywhere since the surface is blocked by the AAO template and this stops the reaction. A little decomposition of methylene blue could be caused by the TiO_2 surface on the top and bottom of the nanotubes. The results also indicate importance of the exposure of the TiO_2 surface to light and reactant in designing materials.

4.4.4 Photoelectrochemical water splitting

The photoelectrochemical experiments showed photocurrent at low voltage regions under both white and visible light. The photo-electrode was prepared by filling the inside of the TiO_2-CNT-Pt nanotubes with a polymer, PVA, to prevent the carbon nanotube and Pt nanoparticles from contacting the electrolyte. Thus, delta photocurrent-potential (ΔJ-V) curves of water oxidation were considered. TiO_2-CNT-Pt shows high photocurrent below 1.23 V versus reversible hydrogen electrode (RHE) under both white and visible light. Even though pristine TiO_2 does not have any activity under visible light, TiO_2-CNT-Pt shows a higher photocurrent under visible light.

The applied bias photon-to current efficiency (ABPE) of TiO_2-CNT-Pt is 1.45 % under white light and 0.83 % under visible light at 0.8 V versus RHE. Since TiO_2 has no activity under visible light and fast recombination of charge carriers, the efficiency is greatly increased by just combining carbon nanotubes and Pt nanoparticles. The enhancement in photoelectrochemical water splitting is attributed to visible light harvesting of TiO_2 by bonding with CNT to generate electron-hole pairs under visible light, separation of the generated electrons and holes at the Schottky junction between TiO_2 and CNT, and low recombination of charge carriers and intermediates due to the spatially separated oxidation and reduction channels in the structure.

4.5 Conclusions

The photoelectrochemical cells of TiO_2-CNT-Pt were developed by locating TiO_2 outside of a carbon nanotube and locating Pt nanoparticles inside of a carbon nanotube to spatially separate the oxidation and reduction reactions. The microscopic images show well-aligned TiO_2-CNT-Pt tubes with a 10 nm wall of TiO_2 outside, graphitic layers for a carbon nanotube, and Pt nanoparticles inside. Raman spectra of TiO_2-CNT-Pt showed a shifted TiO_2 E_g mode which indicates a stronger interaction between the TiO_2 and the CNTs. The photocatalytic activity of the TiO_2-CNT-Pt structure for the photocatalytic degradation of methylene blue under visible light was significantly enhanced. The result is attributed to charge separation that reduces the recombination of e-h pairs and the absorption of visible light by the heterostructure.

The separated oxidation and reduction sites were verified by photo-deposition of MnO_x and Ag. MnO_x was deposited the outside of the TiO_2-CNT-Pt and the Ag nanoparticles were deposited on the inside of the TiO_2-CNT-Pt tubes. By this experiment, it is shown that oxidation sites are on the outside of the TiO_2-CNT-Pt nanotubes and the reduction sites are within the TiO_2-CNT-Pt nanotubes. Moreover, the results demonstrate that the TiO_2-CNT-Pt structure also has a high activity for the separation of oxidation and reduction species hindering backward reaction of intermediates or final products. The unique design of spatially separated channels keeps charge carriers and products from mixing each other. The limited degradation of methylene blue by TiO_2-CNT-Pt with AAO templates confirms the separation of the oxidation and reduction sites and shows that there are negligible pinholes between TiO_2 and CNTs. Even if some of the light can penetrate to TiO_2 and some e-h pairs are photo-generated, holes in the TiO_2 cannot migrate anywhere they are blocked by the AAO template and this stops the reaction.

The photoelectrochemical performance of TiO_2-CNT-Pt showed high photocurrent below 1.23 V versus reversible hydrogen electrode (RHE) under both white and visible light. Even though pristine TiO_2 does not have any activity under visible light, the applied bias photon-to current efficiency (ABPE) of TiO_2-CNT-Pt is 1.45 % under white light and 0.83 % under visible light at 0.8 V versus RHE.

Chapter 5

Effect of TiO_2 thickness and the bondings between TiO_2 and carbon in TiO_2-CNT hybrids on photocatalytic activity

5.1 Research Goals and Hypotheses

The first goal in this chapter is to synthesize TiO_2 with different wall thickness in TiO_2-CNT-Pt membranes and determine their effect on photocatalytic activity. The particle size of photocatalysts is a key parameter for efficient photocatalytic reactions. Typically, a decrease in the particle size increases the specific surface area and in turn increases the number of reactive sites [196]; however, there have reports that an optimal diameter of TiO_2 particle exists for efficient photocatalysis [33]. When the particle size of a photocatalyst is too large or too small, electron and hole recombination rates on the surface of the photocatalyst increase, deteriorating the advantages of high surface area [33].

Meanwhile, the bonding between TiO_2 and carbon is also important to narrow the bandgap of TiO_2 by doping carbon to enhance visible light activity as discussed in the chapter 4. The second goal of this chapter is to investigate two types of bonding between

TiO_2 and carbon in TiO_2-CNT hybrids by using different pyrolysis methods and their effect on photocatalytic activity. The hypothesis of the work is that the pyrolysis of amorphous TiO_2 and glucose as a carbon source at the same time would make their bonding stronger, resulting in more carbon doping or interfacial bonding than when the crystalline TiO_2 and glucose are pyrolyzed separately.

5.2 Experimental methods

5.2.1 Synthesis of TiO_2 with different wall thickness

Fast hydrolysis to make thick TiO_2 walls

To synthesize TiO_2 nanotubes using AAO templates, the sol-gel method with the hydrolysis of a precursor solution was used as a typical synthesis process. Figure 5.1(a) shows the schematic illustration of the synthesis method. To make thick TiO_2 walls, anodic AAO templates were immersed in Titanium butoxide (TBOT) solution for 2 hours followed by dropwise addition of water for a fast hydrolysis which is a typical method to make TiO_2. After 30 minutes, the AAO templates were taken out and excess TiO_2 aggregation on the surface of the AAO was scraped off. It was then rinsed with absolute ethanol and dried overnight at 60 °C. The deposition process was repeated twice to make thicker TiO_2 walls.

Slow hydrolysis to make thin TiO_2 walls

On the other hand, to make a thin and uniform TiO_2 wall, a slow hydrolysis technique was used in this experiment. To this end, we submerged AAO templates in a TBOT solution in a small glass container and then placed the entire small glass container inside a larger glass container with 2 mL of water. We capped the larger glass to control the water vapor level within the larger glass container. Water vapor inside of the large glassware slowly hydrolyzed the TBOT inside the AAO pores in the small glass container. After 2.5 hours, the AAO templates were taken out and excess TiO_2 aggregation on the surface of the AAO was scraped off followed by rinsing with absolute ethanol and drying at 60 °C overnight.

Synthesis of CNT inside of TiO_2 nanotubes

The synthesis process of the TiO_2-CNT is described in the following pages. For both thicknesses of TiO_2, CNT was synthesized simultaneously by pyrolyzing amorphous TiO_2 and glucose at the same time.

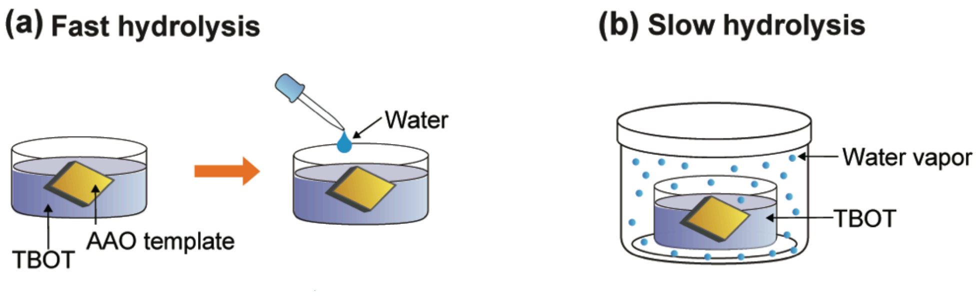

Figure 5.1. Schematics for different TiO_2 synthesis methods. (a) Fast hydrolysis of titanium butoxide (TBOT) solution on the surface of AAO templates by dropwise addition of water. (b) Slow hydrolysis of TBOT by using water vapor inside a closed container.

5.2.2 Synthesis of TiO_2-CNT hybrids with different bonding between TiO_2 and CNT

Synthesis of TiO_2-CNT-onestep

The synthesis process for the TiO_2-CNT-onestep was described in the chapter 4. The name of the sample is based on the one step pyrolysis of TiO_2 and CNT. Briefly, for the TiO_2 synthesis, a titanium butoxide (denoted as TBOT) solution was prepared with a molar ratio of TBOT:ethanol of 1:100 under a N_2 atmosphere. Anodic aluminum oxide (AAO) membranes (Whatman) with 0.2 μm pores, a 60 μm thickness, and a 25 mm diameter were used as templates to make nanotubes. The AAO templates were first immersed in 2 mL of a TBOT solution and then bubbles inside of the AAO were removed under vacuum. To make thin and uniform walls of TiO_2 nanotubes, slow hydrolysis via water vapor was used. After coating with TiO_2, the prepared amorphous TiO_2-AAO structure was immersed in a 5 mL aqueous solution of 0.1 M glucose to make CNTs.

After 1 hour, excess glucose solution on the surface was removed by careful scraping and then the sample was dried at 60 °C for 3 hours and at 180 °C for 3 hours. The glucose coating process was repeated twice. Pyrolysis of the glucose coated amorphous TiO_2-AAO was carried out at 600 °C for 5 hours under an argon atmosphere to make anatase TiO_2 and graphitic layers at the same time.

Synthesis of TiO_2-CNT-twostep

In this case, the synthesis of TiO_2 is the same as for TiO_2-CNT-onestep, but before coating the titania with glucose, anatase TiO_2 was synthesized by annealing the amorphous TiO_2 on the AAO template at 450 °C in air for 2 hours. Thus, TiO_2-CNT-twostep was named for the two-step pyrolysis; making crystalline TiO_2 first then synthesizing CNTs. The next step of carbon nanotube synthesis is the same as described in the preceding paragraph.

5.3 Results: Effect of TiO_2 thickness on photocatalytic activity

5.3.1 Analysis of morphology and microstructure

Figure 5.2 shows a transmission electron microscopy image of the TiO_2-CNT-Pt membranes made by the fast and slow hydrolysis method. The thickness of a TiO_2 wall synthesized by a fast hydrolysis method is about 50 nm as shown in Figure 5.2 (a) while

TiO_2 walls synthesized by a slow hydrolysis method represent around 10 nm wall thickness (Figure 5.2 (b)).

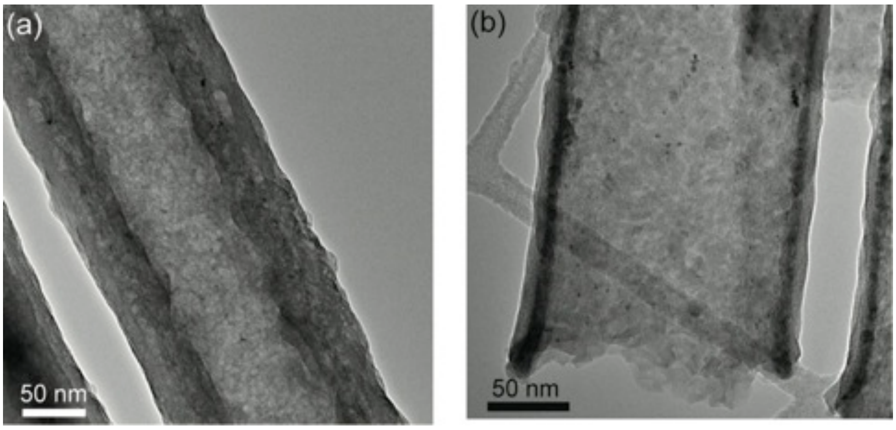

Figure 5.2. TEM images of the two types of TiO_2-CNT-Pt nanotubes. (a) TiO_2-CNT-Pt nanotubes with 50 nm TiO_2 thickness via fast hydrolysis. (b) TiO_2-CNT-Pt nanotubes with 10 nm TiO_2 thickness via slow hydrolysis.

The optical properties of the TiO_2-CNT hybrids with different TiO_2 thicknesses were investigated by UV-vis reflectance. Figure 5.3 shows the reflectance of the CNT, 50 nm TiO_2-CNT, 10 nm TiO_2-CNT, and anatase TiO_2. The bandgaps of the specimens are calculated by using the Kubelka-Munk function, $F(R) = (1-R)^2/2R$, to determine the absorbance and the Tauc-plot, $F(R)hv = A(hv-E_g)^2$. In the cases of the 50 nm and 10 nm TiO_2-CNT membranes, despite the absence of distinct band edges, the results show enhanced visible light response compared to anatase TiO_2. It can be seen that the 50 nm TiO_2-CNT membrane has a higher absorption in the UV region than the 10 nm TiO_2-CNT membrane.

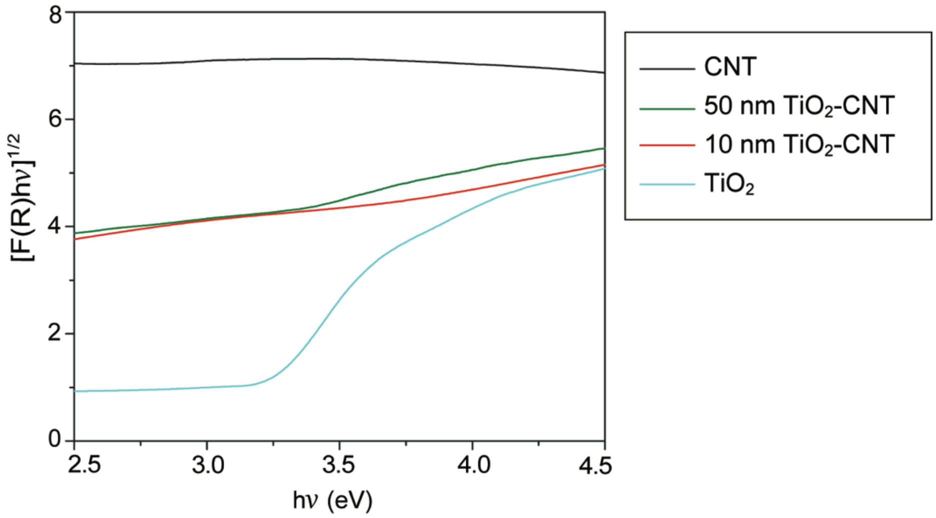

Figure 5.3. Ultraviolet-visible reflectance spectra of 50 nm TiO_2-CNT, 10nm TiO_2-CNT, CNT, and TiO_2. The reflectance spectra was represented via Tauc plot of F(R)*hv* as a function of photon energy (*hv*) using a Kubelka-Munk function of $F(R)=(1-R)^2/2R$.

5.3.2 Photocatalytic properties

The photodegradation of methylene blue was also investigated to test the photocatalytic activity and the results are shown in Figure 5.4. The photocatalytic activities TiO_2-CNT hybrids with different TiO_2 thicknesses were compared with a blank (only methylene blue) and TiO_2 P25 as a reference.

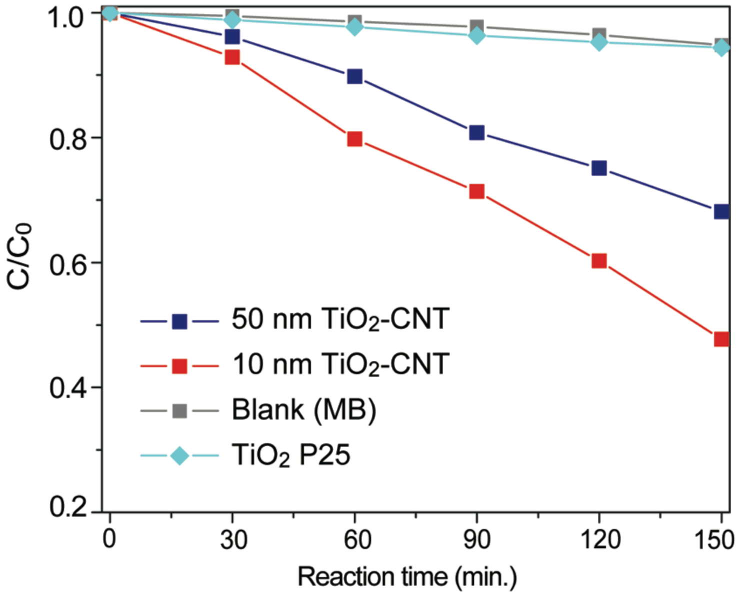

Figure 5.4. Photocatalytic methylene blue degradation using 50 nm TiO_2-CNT, 10 nm TiO_2-CNT, blank (methylene blue), and TiO_2 P25 as a reference under visible light irradiation (λ > 420 nm). The reaction rate of methylene blue degradation per unit mass of photocatalyst and unit time of 50 nm TiO_2-CNT is 22 μmol/h/g and that of 10 nm TiO_2-CNT is 133 μmol/h/g.

Blank (methylene blue) and reference TiO_2 P25 could decompose methylene blue slightly but the amount was negligible. The degradation rate was enhanced with TiO_2-CNT hybrids that have photocatalytic activity under the visible light irradiation. The 10 nm TiO_2-CNT membrane shows higher photocatalytic activity than the 50 nm TiO_2-CNT membrane. To compare how much of the methylene blue was decomposed per unit mass of the photocatalyst per unit time, units of μmol/h/g were also used in this work. The amount of methylene blue degraded per unit mass of the photocatalyst and unit time with the 50 nm TiO_2-CNT membrane was 22 μmol/h/g and with the 10 nm TiO_2-CNT membrane was 133μmol/h/g. For this calculation, we assume C_0 is the initial concentration and all adsorbed dye molecules were decomposed as the calculation in chapter 4.

5.4 Results: Effect of bonding between TiO_2 and CNT on photocatalytic activity

5.4.1 Analysis of morphology and microstructure

Figure 5.5 shows Raman spectra of TiO_2-CNT-onestep, TiO_2-CNT-twostep, and anatase TiO_2 as a reference. In the case of TiO_2-CNT-onestep, the strong peak at 151.0 cm^{-1}, assigned to the E_g mode of anatase TiO_2, was shifted by 7 cm^{-1} compared with that of pristine anatase TiO_2 and by 4.5 cm^{-1} compared with that of TiO_2-CNT-twostep, which indicates a large decrease in the vibration energy of the crystal lattice due to a greater interaction between the TiO_2 and carbon. In the case of TiO_2-CNT-twostep, the strong peak at 146.5 cm^{-1} assigned to the E_g mode of anatase TiO_2 is shifted by 2.5 cm^{-1} which is lower than that of TiO_2-CNT-onestep. The other three peaks at 392, 515 and 638 cm^{-1} are assigned to the B_{1g}, A_{1g} or B_{1g}, and E_g modes of anatase phase, respectively. The Raman peaks at 1316 and 1585 cm^{-1} correspond to the D and G-mode, respectively.

The optical properties were investigated by UV-vis reflectance. Figure 5.6 shows the reflectance of TiO_2, TiO_2-CNT-onestep, TiO_2-CNT-twostep, and carbon. The TiO_2 sample was prepared by synthesizing it using the sol-gel method on the AAO templates followed by annealing at 450 °C in air, and carbon is prepared by coating glucose on the AAO templates followed by pyrolysis at 600 °C under argon. The bandgaps of the specimens are calculated by using Kubelka-Munk function, $F(R) = (1-R)^2/2R$, and Tauc-plot, $F(R)hv = A(hv-E_g)^2$.

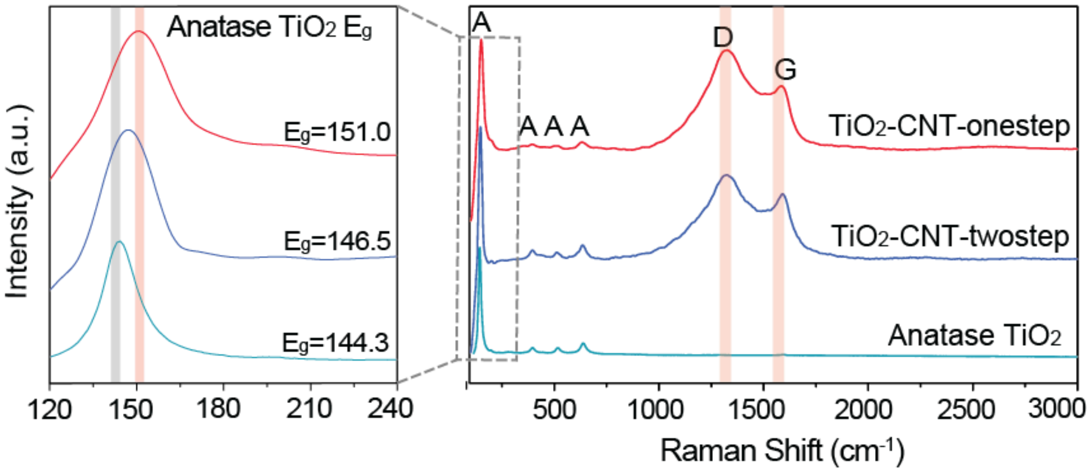

Figure 5.5 Raman spectra. The shift of the TiO_2 E_g peak region (left) and the whole spectrum [2] of TiO_2-CNT-onestep, TiO_2-CNT-twostep, and TiO_2-anatase.

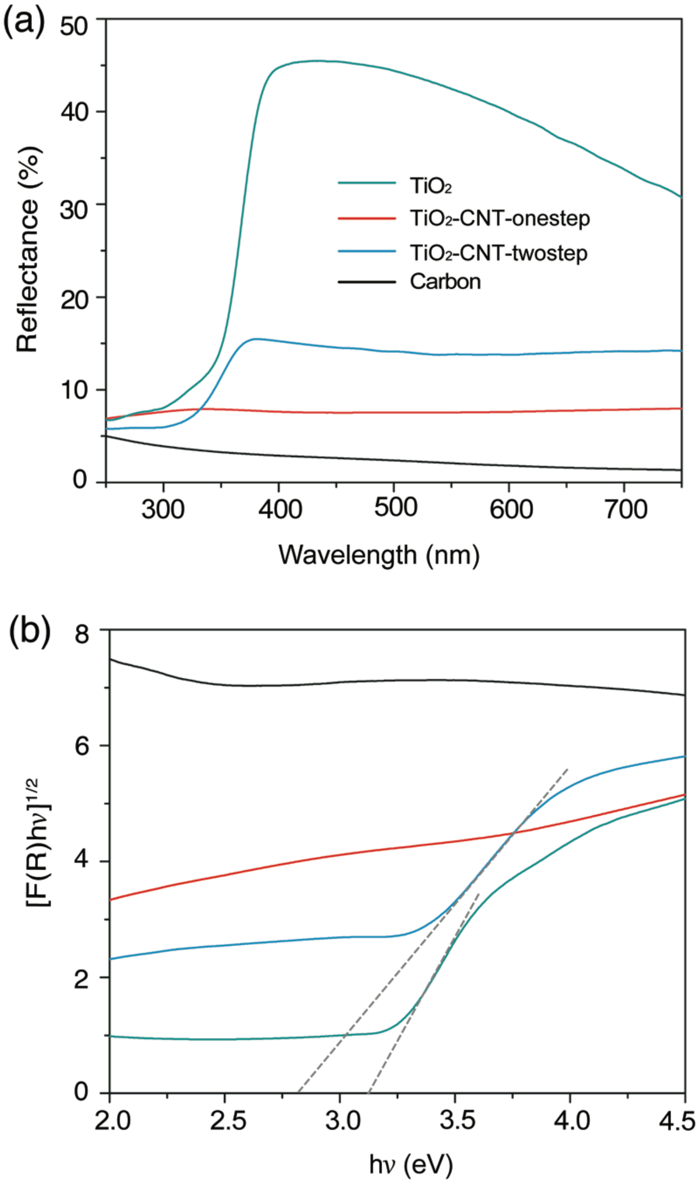

Figure 5.6 (a) Ultraviolet-visible reflectance spectra of CNT, TiO_2-CNT-onestep, TiO_2-CNT-twostep, and TiO_2. (b) Tauc plot of F(R)*hv* as a function of photon energy(*hv*) using a Kubelka-Munk function of $F(R)=(1-R)^2/2R$.

5.4.2 Photocatalytic properties

To investigate the difference in photocatalytic activity between TiO_2-CNT-Pt-onestep and TiO_2-CNT-Pt-twostep, photodegradation of methylene blue was investigated under visible light (Figure 5.7). Before getting the results, all of the methylene blue degradation experiments in this work were conducted after 2 hours in the dark to establish an adsorption/desorption equilibrium between methylene blue and the surfaces of the specimens. The reaction rate of TiO_2-CNT-Pt-twostep is 127 μmol/h/g which is lower than that of TiO_2-CNT-Pt-onestep, 173 μmol/h/g. TiO_2-CNT-twostep also has less activity than TiO_2-CNT-onestep with a rate of 113 μmol/h/g. These results indicate that TiO_2-CNT-Pt synthesized by one step pyrolysis of amorphous TiO_2 and glucose shows higher photocatalytic activity than TiO_2-CNT-Pt synthesized by two step pyrolysis.

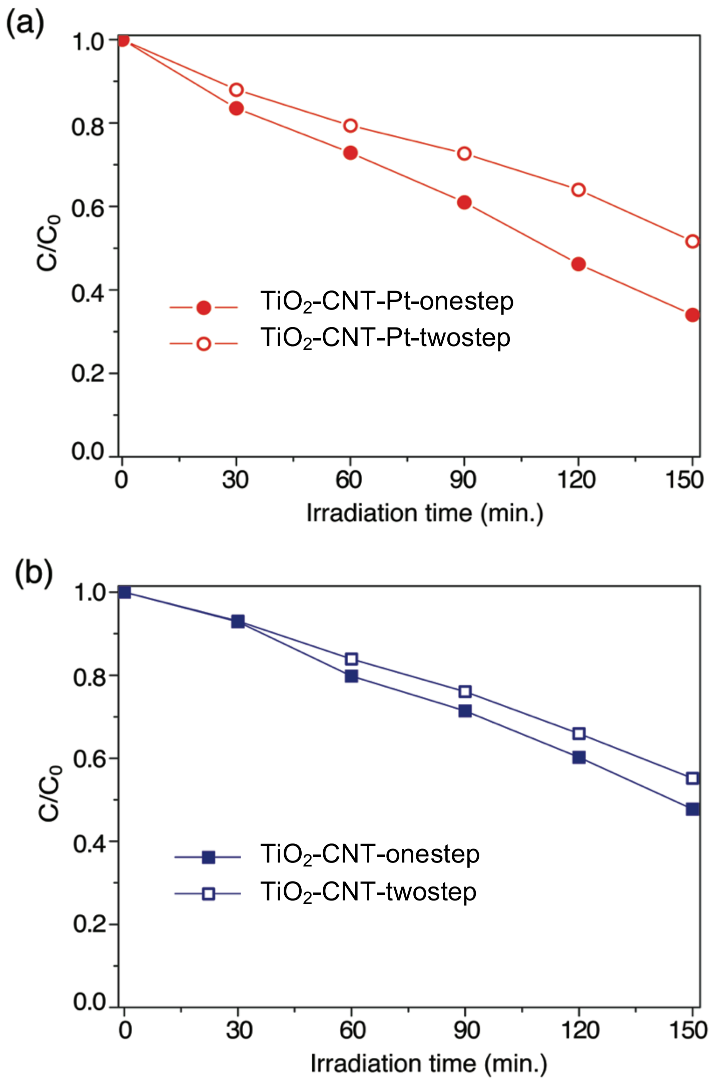

Figure 5.7 (a) Photocatalytic methylene blue degradation of TiO_2-CNT-Pt-onestep and TiO_2-CNT-Pt-twostep. The reaction rate of TiO_2-CNT-Pt-onestep, 173 μmol/h/g, is 1.36 times higher than that of TiO_2-CNT-Pt-twostep, 127 μmol/h/g. (b) Photocatalytic methylene blue degradation of TiO_2-CNT-onestep and TiO_2-CNT-twostep. The reaction rate of TiO_2-CNT-onestep is 133 μmol/h/g which is 1.17 times higher than that of TiO_2-CNT-twostep, 113 μmol/h/g.

5.5 Discussion

5.5.1 Effect of TiO_2 thickness in TiO_2-CNT hybrids on photocatalytic activity

The transmission electron microscopy image of the TiO_2-CNT-Pt membranes synthesized by the fast hydrolysis method shows that the thickness of TiO_2 is about 50 nm and the inside surfaces are non-uniform due to fast particle growth. Meanwhile, TiO_2 walls synthesized by the slow hydrolysis method have very clear outer and inner wall surfaces with wall thicknesses around 10 nm. The slow hydrolysis makes smaller and slower growing TiO_2 particles resulting in thinner walls and smooth outer and inner surfaces.

The optical properties of both the 50 nm and 10 nm TiO_2-CNT membranes show the absence of a distinct band edge and enhanced visible light absorption compared to anatase TiO_2. It can be seen that the 50 nm TiO_2-CNT membrane has greater absorption in UV region than the 10 nm TiO_2-CNT membrane, indicating that thicker TiO_2 absorbs more light. Since there is no more absorption in the visible region with the 50 nm TiO_2-CNT membrane, it is noted that thicker TiO_2 only enhances the absorption in the UV region and not in the visible region. This result can be also explained if the visible light absorption of the hybrids arises from the interface between TiO_2 and CNT, and thus more TiO_2 than an optimal thickness is not necessary to absorb more visible light.

The photocatalytic activities of TiO_2-CNT hybrids with different thicknesses of TiO_2 were investigated via methylene blue degradation under visible light irradiation. Both the 10 nm and 50 nm TiO_2-CNT hybrids show enhanced photocatalytic activity under visible light compared to pristine CNT and TiO_2. Specifically, the 10 nm TiO_2-CNT hybrid shows higher photocatalytic activity than the 50 nm TiO_2-CNT hybrid. Even though both TiO_2-CNT hybrids have almost the same absorption properties in visible region as shown by the UV-vis reflectance, the higher photocatalytic activity of the 10 nm TiO_2-CNT can be explained that there were more recombination of electron-hole pairs in the 50 nm TiO_2-CNT hybrid due to the trapping of charge carriers inside of the bulk or at grain boundaries. Thus the photocatalytic activity of the 50 nm TiO_2-CNT hybrid was as low as 22 μmol/h/g while that of 10 nm TiO_2-CNT was 133 μmol/h/g. The result implies that the reaction occurred on the surface of photocatalyst and that beyond 10 nm, additional photocatalyst inside the bulk is not necessary to enhance the activity.

5.6.2 Effect of bonding between TiO_2 and carbon on photocatalytic activity

The Raman spectra of the TiO_2-CNT-onestep imply more interaction between the TiO_2 and the carbon nanotubes than occurs in the TiO_2-CNT-twostep. The lowest peak assigned to the E_g mode of anatase TiO_2 was shifted by 7 cm^{-1} compared with that of pristine TiO_2 and 4.5 cm^{-1} compared with that of TiO_2-CNT-twostep. The result is consistent with the improvement in photocatalytic activity under visible light irradiation of the membranes with a larger peak shift. In contrast, in the TiO_2-CNT-Pt-twostep, crystalline anatase TiO_2 was first formed by annealing in air. The effect of pyrolysis in argon gas was negligible since anatase TiO_2 was already formed.

The optical properties of TiO_2-CNT membranes are also enhanced. It can be seen that TiO_2-CNT-twostep has a lower bandgap than anatase TiO_2. In the case of TiO_2-CNT-onestep, despite the absence of a distinct bandgap edge, the results show enhanced visible light response compared to TiO_2-CNT-twostep and anatase TiO_2. At the junction of the TiO_2 and CNT, electronic interaction between them as well as carbon doping might occur on the TiO_2 lattice, narrowing the bandgap [183]. During the synthesis process, glucose can be transformed to graphitic layers by pyrolysis under argon, which have π electrons that might bond with TiO_2 [187, 189]. The bandgap of pristine TiO_2 is around 3.2 eV; therefore, it does not absorb visible light. However, by interacting with graphitic layers, the bandgap of TiO_2 was narrowed inducing visible light response. The bandgap narrowing of TiO_2 makes it possible for electrons in the valence band to be excited to the conduction band by absorbing visible light and by transferring through the carbon layers to the platinum particles. The carbon layer can promote charge transfer from the TiO_2 to the carbon layer better than TiO_2 alone, and this accelerates the degradation of methylene blue. There is also a difference in the photocatalytic activities of TiO_2-CNT-Pt-onestep and TiO_2-CNT-Pt-twostep. Both TiO_2-CNT-Pt-onestep and TiO_2-CNT-onestep have higher photocatalytic activity than TiO_2-CNT-Pt-twostep and TiO_2-CNT-twostep, respectively. As shown in Raman spectra and reflectance, there is more interaction between TiO_2 and carbon in the case of TiO_2-CNT-onestep. This occurs during pyrolysis when the amorphous TiO_2 transforms to anatase TiO_2 at the same time that the glucose transforms to graphitic layers.

The enhanced photocatalytic activities are also caused by the unique TiO_2-CNT-Pt structure that separates the oxidation and reduction sites. In the TiO_2-CNT-Pt structure, photo-excited electrons from the surface of TiO_2 can transfer through a carbon nanotube to a platinum particle that is located inside of the carbon nanotube, which separates the charge carriers as well as the intermediates and products. On the other hand, if platinum particles are on the surface of TiO_2, photo-excited electrons can transfer to platinum particles located on the TiO_2 directly. In that case, the charge separation would be fast; however, the oxidation and reduction reactions are not spatially separated. Thus, the unique TiO_2-CNT-Pt structure with a strong interaction between the TiO_2 and carbon nanotubes contributed to efficient photocatalysis similar to what is found in a photoelectrochemical cell.

5.7 Conclusions

The microscopic images of the TiO_2-CNT hybrids synthesized by fast hydrolysis showed that the TiO_2 walls were about 50 nm thick while the TiO_2-CNT hybrids synthesized by slow hydrolysis had TiO_2 walls about 10 nm thick. Optical properties of the 50 nm TiO_2-CNT hybrid showed higher absorption in the UV region than the 10 nm TiO_2-CNT hybrid, indicating that the thicker TiO_2 absorbs more UV light; however, thicker TiO_2 did not absorb more visible light. The photocatalytic activity of the 10 nm TiO_2-CNT hybrid was enhanced compared to the 50 nm TiO_2-CNT hybrid for the degradation of methylene blue under visible light. This implies that there may be an optimal thickness of TiO_2 that maximizes the photocatalytic activity.

For the experiments on the effect of bonding between TiO_2 and carbon, the TiO_2-CNT-Pt-onestep showed greater photocatalytic activity than the TiO_2-CNT-Pt-twostep under visible light. The peak assigned to the E_g mode of anatase TiO_2 was shifted by 7 cm^{-1} compared with that of pristine TiO_2 and 4.5 cm^{-1} compared with that of the TiO_2-CNT-twostep, which implies that there is a stronger interaction between TiO_2 and carbon in the one step material. The photocatalytic activity of the TiO_2-CNT-Pt-onestep for the photocatalytic degradation of methylene blue under visible light was significantly enhanced compared to the TiO_2-CNT-Pt-twostep hybrid. This also suggests stronger bonding between the TiO_2 and carbon together. The one step pyrolysis also leads to a narrower bandgap and more light absorption and this also enhances the photocatalytic activity.

Chapter 6

TiO_2–Single walled carbon nanotube aerogels

6. 1. Background

Single walled carbon nanotubes have ultrahigh specific surface area [197], outstanding electrical [198] and thermal conductivities [199], and high mechanical strength [200]. To maximize the properties of SWCNTs, it is important to make singly isolated SWCNTs by eliminating bundles and reducing the volume fraction. Aerogels are highly porous materials with high surface area-to-volume ratios [25].

Bryning et al. [25] developed carbon nanotube aerogels from aqueous-gel precursors by critical point drying and freeze-drying. Their aerogels were derived from CNT networks in suspension, and the network properties are readily manipulated. Figure 6.1 (a) shows low density, free standing SWCNT aerogels fabricated by Kim et al. [22] from purified and isolated SWCNTs. As shown in the figure, the shape and size of the aerogels are tunable, which is strength of the aerogels. The SEM and TEM images of the aerogels show a porous, isotropic nanotube network with an open-cell structure (Figure 6.1 (b)). They found that the specific surface area of the SWCNT aerogels was 1291 m^2/g at a density of 7.3 mg/ml, which approaches the theoretical limit of 1315 m^2/g.

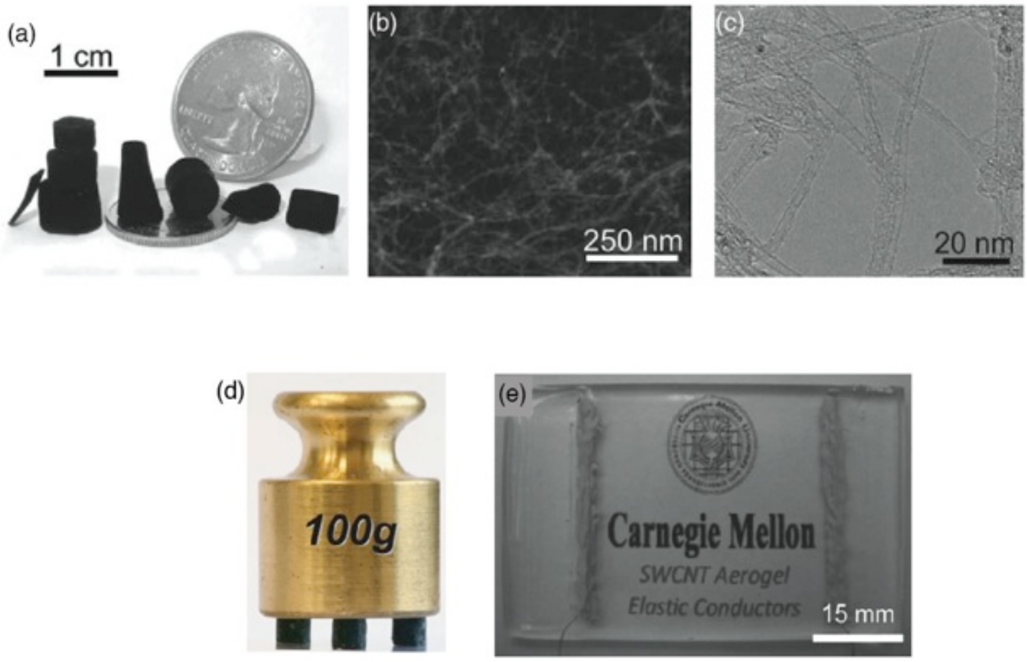

Figure 6.1 (a) SWCNT aerogels with various sizes and shapes such as cylinders, rectangles, cubes, truncated cylinders, and truncated cones [22]. (b) SEM image and (c) TEM image of SWCNT aerogel networks [22]. (d) Mechanical property of SWCNT aerogels which are reinforced by PVA supporting 100 g [25]. (e) A transparent composite film of SWCNT aerogels with the electrodes [201].

Due to the outstanding properties mentioned above, SWCNTs have been regarded as an outstanding material for photoelectrochemical cells, photovoltaic cells, and as a substrate and photosensitizer. However, it is hard to demonstrate the potential improvement in properties if the single walled carbon nanotubes are bundled together [21, 24]. Thus, by using single walled carbon nanotube aerogels with ultrahigh surface area, high porosity, and high conductivity, TiO_2-SWCNT hybrids can be realized in a form where they can be used as high efficiency photocatalysts.

6.2 Research Goal and Hypothesis

A hybrid photocatalyst comprised of TiO_2 and carbon nanotubes has been getting attention continuously; however, the complete advantages of single walled carbon nanotubes (SWCNTs) have yet to be realized because of the easily formed bundles that degrade their ideal properties [21, 24]. The goal of the work in this chapter is to develop TiO_2 coated SWCNT aerogels where the SWCNT aerogels are 3D porous networks of mostly individual SWCNTs. The hypothesis of the research is that when we first synthesize SWCNT gel networks and then coat them with TiO_2, the TiO_2 nanoparticles will disperse at the SWCNT junctions, retaining the network and its properties such as high conductivity and high surface area.

6.3 Experimental method

6.3.1 Fabrication of SWCNT hydrogels and wetgels

Purified SWCNTs (CoMoCAT CG 200; Southwest Nanotechnologies) with diameters of 1.0 ± 0.3 nm and lengths of ~1 μm were mixed with sodium dodecylbenzene sulfonate surfactant (SDBS; Acros Organics) at a SWCNT concentration of 1 mg mL^{-1} and a SWCNTs:SDBS wt. ratio of 1:10 [24, 201] in deionized water (Ultrapure Milli-Q, resistivity 18.2 MΩ·cm). The mixtures were sonicated for 2 h at a power of 60 W using a probe tip sonicator (Thermo Fisher 500). The SWCNTs-SDBS suspensions were then centrifuged at 125,000 g for 19 min (Beckman Coulter Optima™ L-100 K) to pallet bundles and retain mostly isolated nanotubes in the supernatant. We decanted the supernatant and measured SWCNT concentration using UV-visible (vis)-near infrared

(NIR) spectroscopy (Cary 5000; Varian) with a known extinction coefficient of 2.6 (absorbance·ml) (mg·mm)$^{-1}$ at a wavelength of 930 nm. The suspensions were then concentrated to a final nanotube concentration of 3.5 mg ml^{-1} where SWCNTs-SDBS suspensions typically form gels within a few hours. We loaded SWCNTs-SDBS suspensions into glass capillaries and waited 12 h to allow the suspensions to form hydrogels; the glass capillaries acted as molds to provide suitable shapes to the hydrogels for subsequent experiments. We washed off the surfactants using 1 M nitric acid for 20 min at 50 °C. We then removed the hydrogels from the capillaries and washed thoroughly with deionized water. Since titania could not be deposited on SWCNTs gels in water, we exchanged water with increasing concentration of ethanol (EtOH) until SWCNT networks were in anhydrous ethanol; hereinafter we refer to SWCNT networks in ethanol as SWCNT wetgels. In parallel, we also created pristine SWCNT aerogels by removing anhydrous ethanol through critical point drying process.

6.3.2 Fabrication of TiO_2-SWCNT aerogels

The major steps in the synthesis process of TiO_2-SWCNT aerogels are schematically illustrated in Figure 6.2. To make 75 wt.% TiO_2-SWCNT aerogels, we first dissolved titanium butoxide (TBOT; Acros Organics) in anhydrous ethanol under a nitrogen atmosphere at a TBOT:EtOH molar ratio of 1:100. We soaked SWCNT wetgels in the TBOT solution for 2 h at 50 °C, then removed the wetgels from TBOT solution and wiped off any excess solution from the wetgel surfaces using a wet lint-free wiper (Kimwipes; Kimtech) to prevent TiO_2 formation on the surfaces. We hydrolyzed TBOT to make TiO_2 by adding water dropwise of an amount that was about half the volume of the hydrogels. We allowed the hydrolysis process to proceed for half an hour and then washed the wetgels with ethanol several times to remove unreacted TBOT; note, TiO_2 that formed within the wetgels had amorphous structure. We also fabricated 25 wt.% and 90 wt.% TiO_2-SWCNT aerogels and the parameters to fabricate them are shown in Table 6.1. To transform amorphous-TiO_2-SWCNT wetgels into aerogels, we exchanged ethanol with anhydrous ethanol thoroughly followed by critical point drying (Autosamdri 815, Tousimis) of the samples to remove anhydrous ethanol. Finally, we annealed amorphous-TiO_2-SWCNT aerogels at 600 °C for 2 h under argon (Ar) environment to crystallize TiO_2.

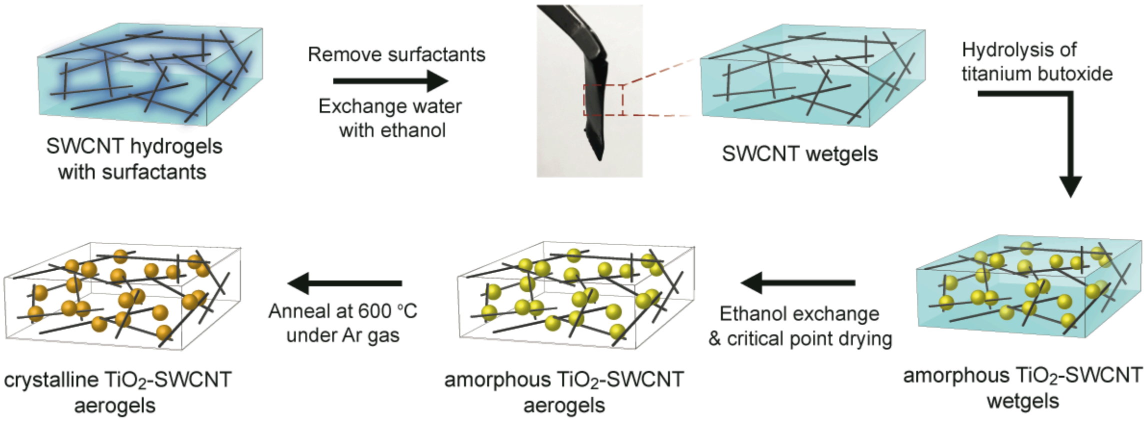

Figure 6.2. Schematic illustration of the fabrication process for TiO_2-SWCNT aerogels. SWCNTs are first sonicated in water with surfactants followed by drying until gelation. Then, the surfactants are removed by using a nitric acid solution. After neutralization and ethanol exchange, titanium butoxide (TBOT) was used to deposit TiO_2 by hydrolysis. After exchange of ethanol, the gels are dried by critical point dry (CPD) followed by annealing under an argon atmosphere.

Table 6.1 Parameters to fabricate different wt.% of TiO_2-SWCNT aerogels.

Name of specimen	Wt.% ratio of TiO_2 to SWCNT	TBOT: EtOH	Coating times
25 wt.% TiO_2-SWCNT	1 : 3	1: 200	1
75 wt.% TiO_2-SWCNT	3 : 1	1: 100	1
90 wt.% TiO_2-SWCNT	9 : 1	1: 100	2

6.3.3 Structural stability characterization by immersion in water

We submerged both freestanding SWCNT and TiO_2-SWCNT aerogels of known physical dimensions in distilled water and then applied a weak vacuum to facilitate water infiltration into the nanopores of the aerogels until air bubbles stopped escaping from the aerogels (~15 min). We kept the samples in water for 5 h and measured their physical dimensions once per hour.

6.4 Results

6.4.1 Analysis of morphology and structure

Figure 6.3 (a) shows photographs of single walled carbon nanotube (SWCNT) hydrogels. The SWCNTs in a sodium dodecylbenzene sulfonate solution are injected into a piece of capillary with a 400 μm thickness (left) and, after 1-day gelation, hydrogels are formed with the shape of the capillary. After nitric acid treatment to remove the surfactant and neutralize, the hydrogels inside of the capillary are taken out to be ready for TiO_2 deposition. Figure 6.3 (b) shows photographs of pristine SWCNT aerogels (left two images) and TiO_2 coated SWCNT aerogels (the others). These aerogels are free standing with the TiO_2-SWCNT aerogels begin grey and the SWCNT aerogels being black. The bottom image shows the thickness and curvature of the TiO_2-SWCNT aerogels.

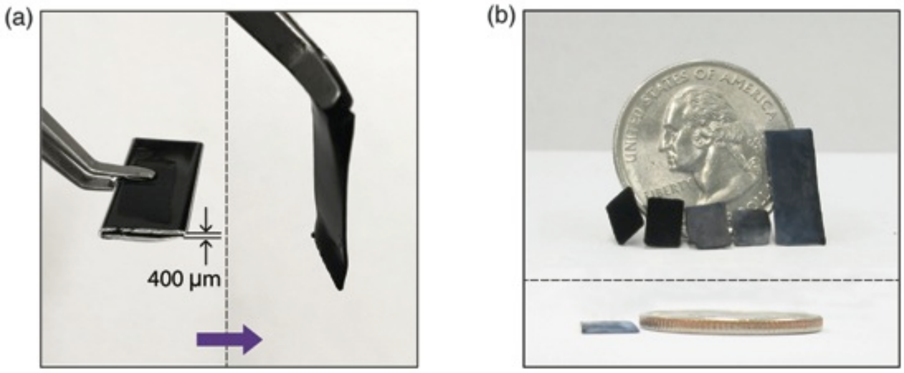

Figure 6.3 (a) Photographs of pristine single walled carbon nanotube hydrogels. The SWCNTs in a surfactant solution are first injected into a piece of capillary with a 400 µm thickness (left), and after 1-day gelation hydrogels are formed with the shape of the capillary [2]. (b) Photographs of pristine SWCNT aerogels and TiO_2 coated SWCNT aerogels (top). The bottom image shows the thickness and curvature of the TiO_2 coated SWCNT aerogels.

A scanning electron microscopy image of a 75 wt.% TiO_2-SWCNT aerogel reveals a uniform network within the aerogel (Figure 6.4 (a)). A transmission electron microscopy image of a 75 wt.% TiO_2-SWCNT aerogel shows TiO_2 nanoparticles deposited on well-dispersed SWCNTs as shown in Figure 6.4 (b). The average size of the TiO_2 nanoparticles is 9.3 nm and most of the TiO_2 nanoparticles are seated on junctions of the SWCNT network.

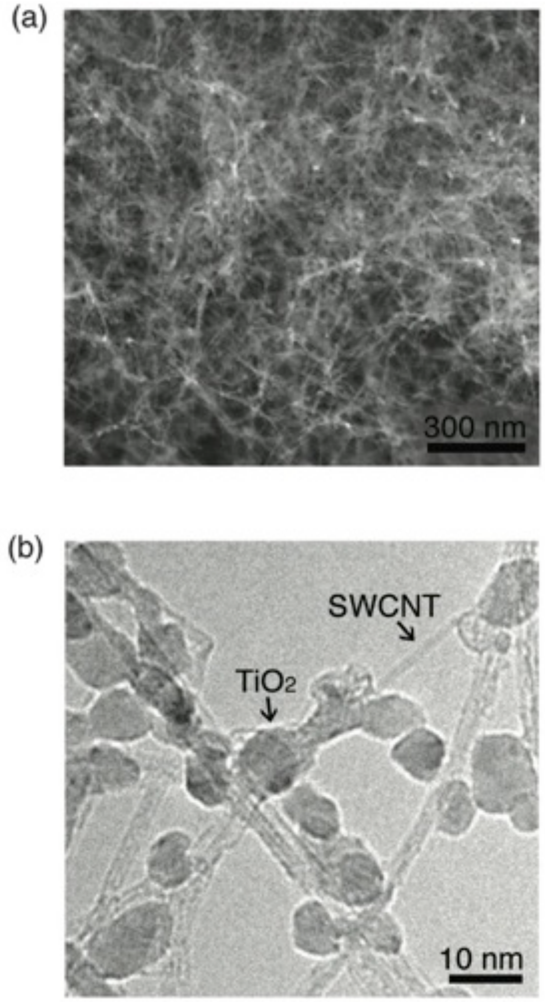

Figure 6.4 Morphologies and microstructure of TiO_2-SWCNT aerogels. (a) SEM image of 75 wt.% TiO_2-SWCNT aerogels. (b) TEM image of 75 wt.% TiO_2-SWCNT aerogels, which shows TiO_2 nanoparticles deposited on well-dispersed SWCNTs.

Analysis of structure and phases

Raman spectroscopy was investigated to study microstructure of TiO_2-SWCNT aerogels (Figure 6.5). Anatase TiO_2 was synthesized as a control specimen using the sol-gel method and annealing at 450 °C in air. The Raman spectrum of anatase TiO_2 shows a strong peak at 144 cm^{-1} corresponding to the E_g mode of anatase TiO_2. The Raman spectra of the TiO_2-SWCNT aerogel series show well-defined TiO_2 peaks, RBM, and D and G mode. In the case of TiO_2 coated SWCNT aerogels, the strong peak at 150 cm^{-1}, assigned to the E_g mode of anatase TiO_2, was shifted by 6 cm^{-1} compared with that of the pristine anatase TiO_2. This indicates a large decrease in the vibration energy of the crystal lattice due to interaction between TiO_2 and the carbon nanotubes. The RBM mode is a unique property of SWCNTs and TiO_2-SWCNT aerogels also show the RBM mode without any decrease in its intensity implying there is no change in the SWCNT properties. A small D-band and a high G-band are also properties of SWCNTs and the TiO_2-SWCNT aerogel series also shows also small D-bands implying that the addition TiO_2 does not create additional defects.

The crystal structure of TiO_2 was also investigated by X-ray diffraction. Figure 6.6 shows the X-ray diffraction pattern of the 90 wt.% TiO_2-SWCNT aerogel. From the result, distinct peaks show that some TiO_2 is crystalline and that there is a mixture of the anatase and rutile phases. The conductivity (S/cm) and density of pristine SWCNT aerogels, 25 wt.% TiO_2-SWCNT aerogels, 75 wt.% TiO_2-SWCNT aerogels, and 90 wt.% TiO_2/SWCNT aerogels are calculated and shown at Figure 6.7. The conductivity of the TiO_2-SWCNT aerogels is enhanced compared to pristine TiO_2 (10^{-12} S/cm) even though even though they are less conductive than pristine SWCNT aerogels. The density of the TiO_2-coated SWCNT aerogels is less than that of anatase TiO_2, about 3.78 g/cm^3.

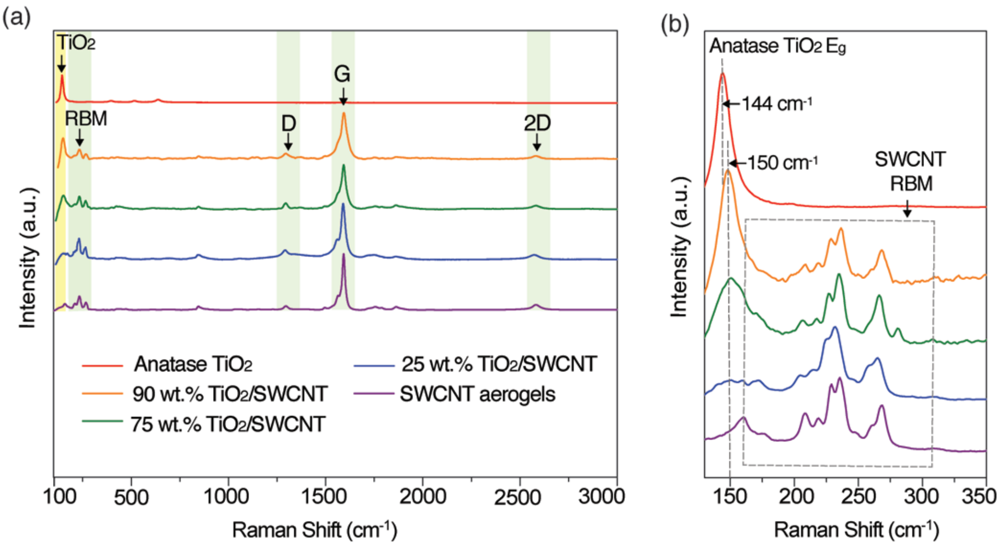

Figure 6.5 Raman spectra. (a) Whole spectra of anatase TiO_2, 25 wt.% TiO_2/SWCNT aerogels, 75 wt.% TiO_2/SWCNT aerogels, 90 wt.% TiO_2/SWCNT aerogels, and pristine SWCNT aerogels. (b) TiO_2 E_g peak region and RBM mode of SWCNTs.

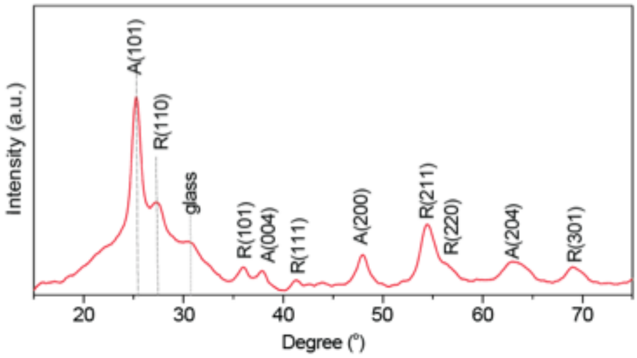

Figure 6.6 X-ray diffraction pattern of a 90 wt.% TiO_2-SWCNT aerogels indicating both anatase and rutile phases coexist.

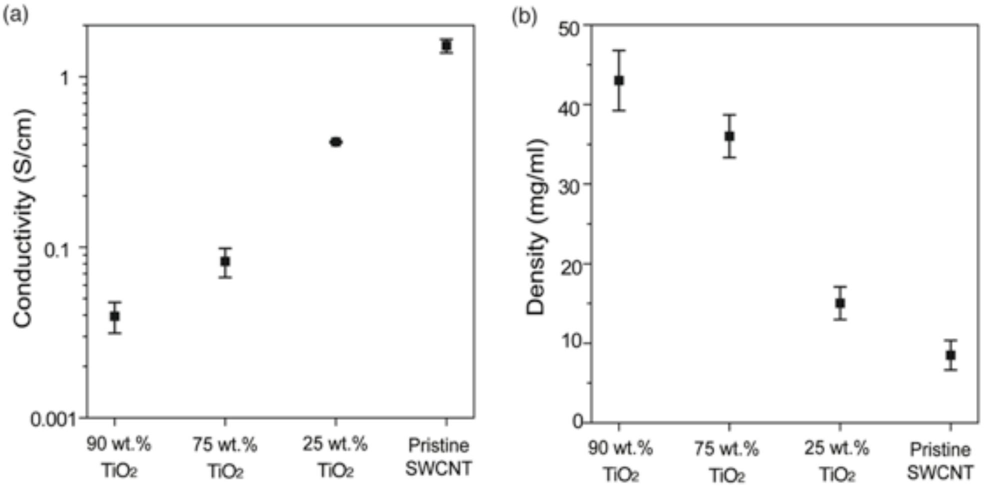

Figure 6.7 (a) Conductivity (S/cm) and (b) density of pristine SWCNT aerogels, 25 wt.% TiO_2-SWCNT aerogels, 75 wt.% TiO_2-SWCNT aerogels, 90 wt.% TiO_2-SWCNT aerogels. Since the conductivity of TiO_2 is about 10^{-12} S/cm and density of TiO_2 (anatase) is ~ 3.78 g/cm^3, the conductivity of the TiO_2-SWCNT was enhanced compared to pristine TiO_2 even though the value was less than that of pristine SWCNT aerogels.

We further examined interactions between TiO_2 and SWCNTs by determining various bondings within TiO_2-SWCNT aerogels using XPS (Figure 6.8). The 1s core level spectrum of carbon (C) can be deconvolved into five peaks: the C=C peak at around 283.8 eV and the C–C peak at 284.9 eV were the dominant peaks arising from SWCNTs with comparatively smaller but still significant C–O peak at 285.8 eV (O ≡ oxygen), which suggests that some oxygen dissociated from titania and formed bonds with SWCNTs, along with Ti–C peak at 282.4 eV (Ti ≡ titanium) and Ti–O–C at 287.2 eV, further validating bonding between titania and SWCNTs. Signatures of these bondings were also present in the deconvolved 2p core level spectrum of Ti with Ti–O $2p_{3/2}$ and $2p_{1/2}$ peaks at 459.0 eV and 464.8 eV, respectively, as well as Ti–C peaks at 460.6 and 466.0 eV. Finally, the 1s core level spectrum of O can be fitted into two peaks of which one of the peaks at 530.5 eV can be attributed to Ti–O and the other peak at 532.7 eV can be attributed to C–O. Overall, the 1s core level spectrum of C and 2p core level spectrum of Ti established that titania formed bonds with SWCNTs within TiO_2-SWCNT aerogels.

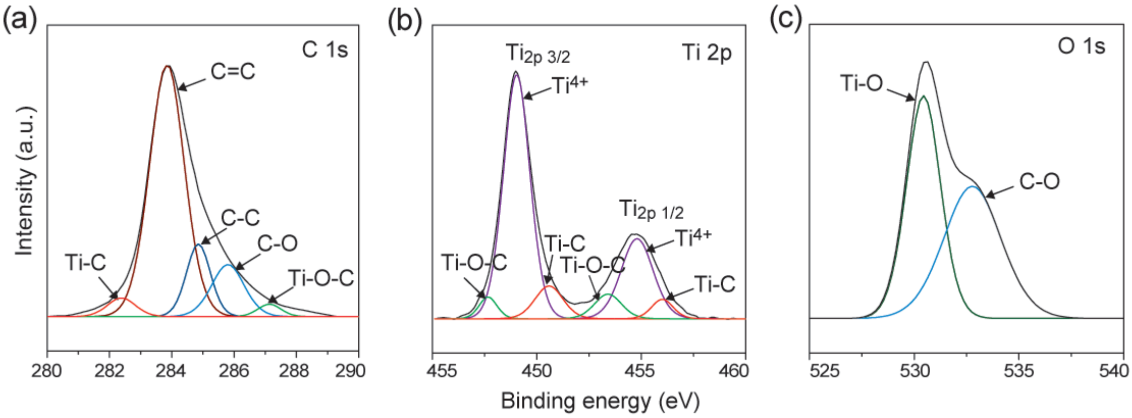

Figure 6.8 X-ray photoelectron spectroscopy (XPS) spectra from TiO_2/SWCNT aerogels for (c) 1s core level of carbon (C), (d) 2p core level of titanium (Ti), and (e) 1s core level of oxygen (O), suggesting Ti-C and Ti-O-C bonding between TiO_2 and SWCNTs.

We next assessed the effects of interactions between TiO_2 and SWCNTs on the optical absorbance and bandgap of TiO_2-SWCNT aerogels using UV-Vis reflectance spectroscopy (Figure 6.9). Anatase TiO_2 showed significant reflectance across visible spectrum, whereas SWCNT and TiO_2-SWCNT aerogels showed minimal reflectance over the same range. To estimate the bandgap of TiO_2-SWCNT aerogel composites, we first calculated Kubelka-Munk function, F(R), from the reflectance (R) using the expression $F(R) = (1-R)^2/2R$ and then plotted $[F(R)\cdot h\nu]^{1/2}$ as a function of photon energy, $h\nu$. This type of plot is commonly known as Tauc plot and is widely used to estimate bandgaps of materials. Anatase titania bandgap was observed at the expected ~3.2 eV, while SWCNT aerogels did not show any characteristic bandgap due to broad absorbance in the visible spectrum. Interestingly, TiO_2-SWCNT aerogels showed a bandgap of ~2.6 eV which is significantly lower than anatase TiO_2 bandgap, likely because of the interfacial bondings between TiO_2 and carbon.

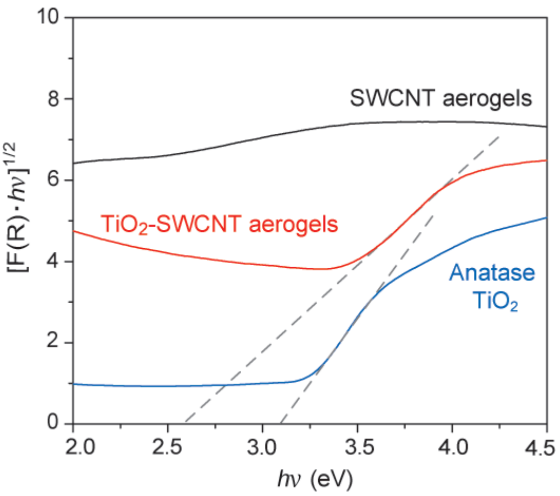

Figure 6.9 Tauc plot of $[F(R)\cdot h\nu]^{1/2}$ versus photon energy, *hν*, to estimate bandgap of TiO_2/SWCNT aerogels.

6.4.2 Analysis of surface area and network stability

The nitrogen adsorption isotherms of the TiO_2-SWCNT aerogel series were measured and are displayed in Figure 6.10 (a). The specific surface area determined from the Brunauer-Emmett-Tellet plot in the range from $P/P_0 = 0.05$ to $P/P_0 = 0.3$ for 25 wt.% TiO_2-SWCNT aerogels is 484.3 m^2/g, for 75 wt.% TiO_2-SWCNT aerogels it is 293.1 m^2/g, and for 90 wt.% TiO_2-SWCNT aerogels it is 140.7 m^2/g. The pore size for pristine SWCNT aerogels is 3.15 nm with a narrow distribution, for 25 wt.% TiO_2-SWCNT aerogels the sizes are 2.0 and 3.2 nm, for 75 wt.% TiO_2-SWCNT aerogels the sizes are 1.8 and 2.8 nm, and for

90 wt.% TiO_2-SWCNT aerogels the size is 2.2 nm. Figure 6.10 (b) shows the pore size distributions of the TiO_2-SWCNT series that were calculated from the desorption branches of the isotherm using Barrett, Joyner, and Halenda (BJH) method. Table 6.2 summarizes the specific surface area, pore size, and pore volume of the TiO_2-SWCNT aerogel series.

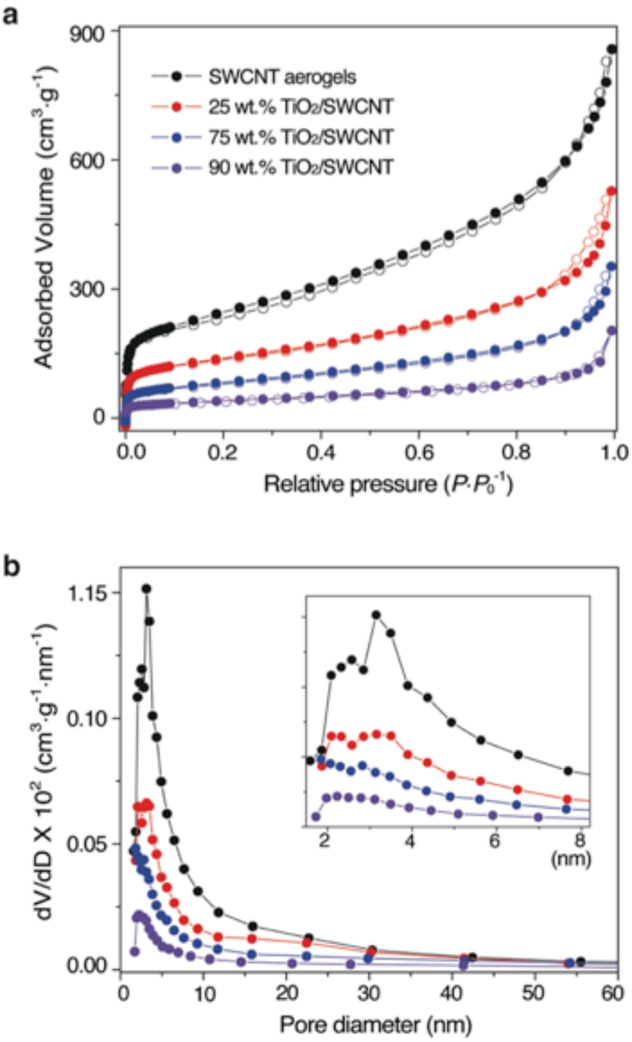

Figure 6.10 (a) Nitrogen adsorption (filled symbol)–desorption (open symbol) isotherm and (b) Pore size distribution of pristine SWCNT aerogels, 25 wt.% TiO_2-SWCNT aerogels, 75 wt.% TiO_2-SWCNT aerogels, and 90 wt.% TiO_2-SWCNT aerogels. The inset of (b) is enlarged data of (b).

Table 6.2 Summary of the specific surface area, pore size, and pore volume of 25 wt.% TiO_2-SWCNT aerogels, 75 wt.% TiO_2-SWCNT aerogels, and 90 wt.% TiO_2-SWCNT aerogels.

Specimen	Specific surface area	Pore size	Pore volume
25 wt.% TiO_2-SWCNT	484.3 m^2/g	2.0 nm, 3.2 nm	0.783 m^3/g
75 wt.% TiO_2-SWCNT	293.1 m^2/g	1.8 nm, 2.8 nm	0.502 m^3/g
90 wt.% TiO_2-SWCNT	140.7 m^2/g	2.2 nm	0.305 m^3/g

To investigate the stability of the TiO_2-SWCNT aerogel networks, each specimen was soaked in distilled water for 5 hours. As shown in Figure 6.11, the volume of the pristine SWCNT aerogels was significantly decreased after the water experiment while the TiO_2-SWCNT aerogels showed a smaller volume decrease. The results imply TiO_2 particles between SWCNT junctions make the network stable in the water environment and maintain their high surface areas.

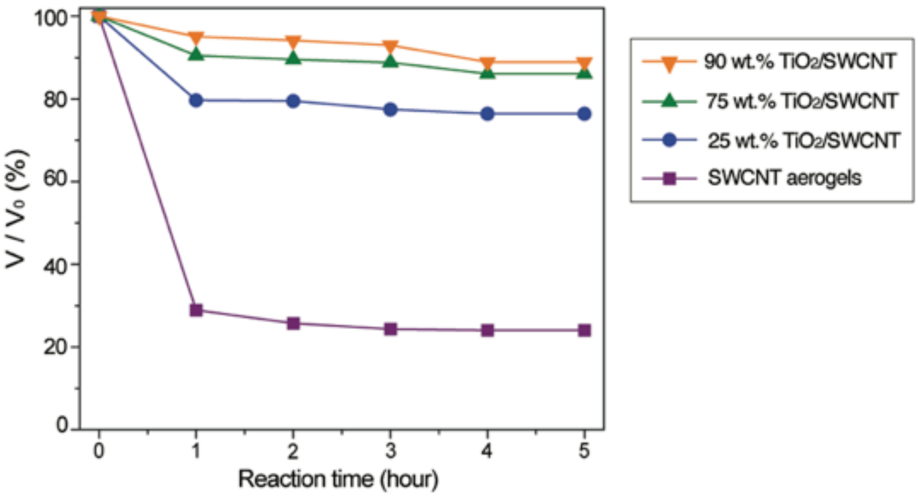

Figure 6.11 Volume changes after water immersion to investigate the stability of the network. Pristine SWCNT aerogels show a large decrease in the volume after water contact compared with 25 wt.% TiO_2-SWCNT aerogels, 75 wt.% TiO_2-SWCNT aerogels, and 90 wt.% TiO_2-SWCNT aerogels. The experiment was conducted by soaking the specimens into distilled water followed by removal of bubbles inside of pores using vacuum.

6.5 Discussion

6.5.1 Analysis of morphology and structure

Scanning electron microscopy images of the TiO_2-SWCNT aerogels show uniform networks and the transmission electron microscopy image shows TiO_2 nanoparticles deposited on well-dispersed SWCNTs. The majority of the TiO_2 nanoparticles are located at the junctions between SWCNTs, which can be explained by the synthesis process. Because the TiO_2 nanoparticles were deposited on existing SWCNT hydrogel networks, TiO_2 is preferentially nucleated at the junctions of the SWCNT network. The TiO_2 nanoparticles located on the SWCNT junctions are very stable, which might be less favorable for catalytic reactions than an unstable location on the open surface of a SWCNT. Despite this, a structure consisting of TiO_2 nanoparticles sandwiched by SWCNTs might be beneficial for other applications such as photoelectrochemical cells and supercapacitors due to the stability of their structure within highly porous networks. Instead of using functional groups to deposit nanoparticles, which can introduce defects in SWCNTs, we used the SWCNT networks as a template to deposit nanoparticles, which contributes to the nanoparticle stability without introducing defects in the SWCNTs.

While the TiO_2 particles grew on the SWCNT network, the network remained intact; the average diameter of TiO_2 was 9.3 nm at the final stage. It has been reported that the optimal diameter for TiO_2 photocatalysts is $\leq$ 11 nm it inhibits surface e^-/h^+ recombination while an intermediate particle size (~ 20 nm) needs Pt loading to prevent e^-/h^+ recombination [196]. In addition to the stability of nanoparticles on defect-free SWCNTs, appropriate particle size of TiO_2 in SWCNT aerogels can also play an important role in the photocatalytic reaction.

Raman spectroscopy was used to determine the phase of TiO_2 and make sure CNTs are well synthesized. In the case of anatase TiO_2, Raman spectra show the E_g mode of anatase TiO_2 at 144 cm^{-1}. Raman spectra of the TiO_2-SWCNT aerogel series also show the E_g mode of anatase TiO_2, and the RBM, D band, and G band for the SWCNTs. The TiO_2 E_g peaks of the TiO_2-SWCNT aerogel series are shifted by 6 cm^{-1}, which implies that the vibration energy of crystal lattice was decreased due to an interaction between the TiO_2 and carbon. In the case of the RBM mode of TiO_2-SWCNT aerogels, it is unchanged from the pristine SWCNT, indicating that the properties of the SWCNTs are not changed. The RBM mode is a unique property of SWCNTs and SWCNT-TiO_2 aerogels also show the RBM mode without any decrease in intensity, implying that the properties of the SWCNTs are not changed. The low D-band and high G-band are also properties of SWCNTs. The Raman peak of the D-band indicates disordered carbon and is taken to be a measure of defects in SWCNTs and the G-band indicates graphitic carbon to measure the amount of sp^2 bonded carbon. The SWCNT-TiO_2 aerogels also show a low D-band indicating that the TiO_2 coating on SWCNTs hardly introduces defects the SWCNTs. Combined, Raman spectra suggest reasonably strong interactions between TiO_2 and SWCNTs likely at the interface between TiO_2 and SWCNTs, but such interactions/bondings did not destroy SWCNT structure.

Improvement in visible light absorption by the TiO_2 is consistent with the Raman spectroscopy results. Interaction between TiO_2 and CNT at the interface could affect the change in the vibrational mode of TiO_2 lattice inducing Raman peak shift as well as band gap narrowing. We further examined interactions between TiO_2 and SWCNTs by determining various bondings within TiO_2-CNT using XPS. Some oxygen dissociated from titania and formed bonds with CNTs, along with C-O and Ti–O–C. The Ti–C peak validates bonding between TiO_2 and CNTs. The XPS results strengthen bonding between TiO_2 and CNTs, which affect the Raman shift as well as band gap narrowing of TiO_2.

6.5.2 Analysis of the surface area and network stability

The specific surface area of the TiO_2-SWCNT aerogels and their highly porous structures are investigated by nitrogen isotherms at 77 K. The TiO_2-SWCNT aerogels show high surface areas that would be effective reactive sites for photocatalytic dye degradation. The isotherms shows hysteresis loops at $P/P_0 > 0.8$ indicating Type IV under IUPAC (1972) classification [202]. The 25 wt.% TiO_2-SWCNT aerogels have a high surface area of 484.3 m^2/g and the other composites of 75 wt.% and 90 wt.% TiO_2-SWCNT aerogels are less than that of the 25 wt.% TiO_2-SWCNT aerogels, but still have high surface areas.

The surface area of the composite decreases as the amount of TiO_2 increases; however, the porous structure of the SWCNT aerogels is preserved. Based on the classification, SWCNT-TiO_2 aerogels have a mesoporous structure where the pore diameters are in the range of 2-50 nm [203]. A gradual increase in the isotherms for $P/P_0 > 0.05$ is due to multilayer formation on the nanotubes [203]. The pore size distributions of the TiO_2-SWCNT aerogels were calculated from the desorption branches of the isotherm using Barrett, Joyner, and Halenda (BJH) method. The photocatalytic reaction occurs on the surface of the photocatalysts so a high surface area provides more reactive sites. The mesopores and the high surface area in the aerogels are important because the make it possible to adsorb more dye molecules to sites where they can be decomposed.

The volume change of the TiO_2-SWCNT aerogels when immersed in water was half that of the SWCNT aerogels, which implies that the TiO_2 nanoparticles support the SWCNT networks by locating at the junctions of each SWCNT. To investigate the hypothesis that TiO_2 nanoparticles are located at SWCNT junctions and stabilize the network, the following experiment was conducted.

Due to Van-der Waals forces, SWCNTs tend to aggregate into bundles [21, 24], especially in water. To make isolated SWCNT aerogels and reduce the number of bundles, a surfactant was used in the fabrication step and removed by nitric acid after the SWCNT hydrogels are made. However, any SWCNTs and any TiO_2-SWCNTs composites including the TiO_2-SWCNT aerogels in this work will need to be in contact with water during a performance test for water-based applications such as photocatalytic dye degradation, photocatalytic water splitting, or photoelectrochemical water splitting. Since TiO_2-SWCNTs composites do not have any surfactants in the final steps of the synthesis process, the SWCNTs might be expected to form bundles in water. However, the volumes of the TiO_2-SWCNT decreased less than the pristine SWCNT aerogel, which implies that TiO_2 nanoparticles help to maintain the structure of the aerogel network.

6.6 Conclusions

In this study, TiO_2-SWCNT aerogels were developed with high surface areas, charge separation, and networks that were stable under water. In the synthesis process, SWCNT gel networks were prepared and then coated with TiO_2 using the sol-gel method. Scanning electron microscopy and transmission electron microscopy showed that TiO_2-SWCNT aerogels had uniform networks and TiO_2 nanoparticles with a 9.3 nm average particle size situated at the junctions. The Raman spectra of the TiO_2-WCNT aerogel series showed that the TiO_2 E_g mode was shifted by 6 cm^{-1}, indicating a decrease in vibration energy. There were negligible differences in the RBM mode, D-band, and G-band between the TiO_2-SWCNT aerogels and the pristine SWCNT aerogels.

TiO_2-SWCNT aerogels have a high specific surface area and porosity. The highly porous networks of TiO_2-SWCNT aerogels remained after critical point drying. The volume change of the TiO_2-SWCNT aerogels on drying was half that of the SWCNT aerogels, implying that TiO_2 particles help to support the SWCNT networks by immobilizing the positions of the junctions where SWCNTs meet. The stability of the TiO_2-SWCNT aerogels was shown by the water contact experiment, where the total volume change of the specimens after water contact was smaller for the TiO_2-SWCNT aerogels than for the pristine aerogels.

Chapter 7

Photocatalytic dye degradation by TiO_2-SWCNT aerogels and Pt loaded aerogels

7.1. Research goals and hypotheses

In this chapter, the main focus is on the simultaneous enlargement of TiO_2 absorbance to the visible light region and the enhanced photocatalytic performance of the TiO_2 nanoparticles when deposited on SWCNT aerogels. One challenge of using high surface area materials in degradation studies is that one must distinguish the dye removal that occurs by physical adsorption onto the carbon materials versus chemical degradation. Most people use 10 minutes to 2 hours to reach the physical adsorption/desorption equilibrium in the dark [187, 189-191]. If equilibrium is not achieved, then degradation rates will be overestimated. Thus, it is necessary to distinguish the physical absorption and photochemical removal of dyes to show the accurate activity of the photocatalysts. Thus, in this chapter, we characterize the adsorption/desorption equilibrium first, so that the photochemical decomposition rates can be measured independent of this process. The second goal of this chapter is to investigate the effect of Pt particles deposited on the TiO_2-SWCNT aerogels. Cocatalysts such as Pt nanoparticles have been reported to enhance the photocatalytic activity by separating charge carriers [34, 35]. Therefore, we deposit Pt particles on TiO_2-SWCNT aerogels to determine whether or not Pt can enhance the photocatalytic activity.

7.2 Experimental methods

7.2.1 Fabrication of TiO_2-SWCNT aerogels

The TiO_2-SWCNT aerogels were synthesized using the same method described in the chapter 6 and the all of the TiO_2-SWCNT aerogels used in this chapter are 75 wt.% TiO_2-SWCNT aerogels.

7.2.2 Fabrication of Pt-TiO_2-SWCNT aerogels

To investigate the effect of metal cocatalysts on photocatalytic performance of TiO_2/SWCNT aerogel composites, we deposited platinum nanoparticles on TiO_2-SWCNT aerogels. We soaked TiO_2-SWCNT aerogels in an aqueous solution of 10 mM hexachloroplatinic acid (H_2PtCl_6) under weak vacuum for ~1 h to remove any air bubbles trapped inside the aerogels and to facilitate solution infiltration. We then removed the samples from the H_2PtCl_6 solution, gently wiped off any excess solution from the sample surfaces using a wet lint-free wiper (Kimwipes; Kimtech) to prevent platinum formation on the surfaces. To create platinum nanoparticles, we reduced H_2PtCl_6 solution by adding 0.5 ml of sodium borohydride ($NaBH_4$) solution, which was prepared by mixing 40 mM $NaBH_4$ with 20 mM sodium hydroxide (NaOH) solution, dropwise onto the sample. We allowed the reduction process to proceed for ~30 min, and then washed the sample with deionized water to remove unreacted H_2PtCl_6, $NaBH_4$ and NaOH solutions. To make Pt-TiO_2-SWCNT aerogels, we exchanged the water inside of the Pt-TiO_2-SWCNT hydrogels with increasing concentration of ethanol until the gels were in anhydrous ethanol, and then dried with a critical point dryer.

7.2.3 Fabrication of TiO_2-Pt-SWCNT aerogels

The TiO_2-Pt-SWCNT aerogels were fabricated by first making SWCNT hydrogels, then depositing platinum nanoparticles onto SWCNTs, followed by exchanging water with anhydrous ethanol and lastly growing TiO_2 within Pt-SWCNT wetgels. The reagents and their concentrations as well as the synthesis steps for making platinum and TiO_2 nanoparticles were identical to the process described in previous sections.

The typical dimensions of all aerogels were 8 mm × 4 mm × 0.4 mm (length × width × thickness) that were imposed by the glass capillary. The average density of SWCNT aerogels was ~9 mg mL^{-1}, which corresponds to a volume fraction of ~0.006. After TiO_2 deposition on SWCNT aerogels, the density increased to ~36 mg mL^{-1} that translates to a volume fraction of ~0.01, a titania mass loading of 2 mg cm^{-2}, and a porosity of ~99%, which allowed easy transport of dye molecules to the titania surfaces.

7.2.4 Experimental setup for the photocatalytic degradation of methylene blue

0.25 mg of photocatalyst was put into a 5 ml aqueous solution of 0.02 mM methylene blue. The suspension was stirred for 24 hours in the dark until the adsorption/desorption equilibrium for methylene blue molecules on the catalyst surface was reached. The specimen in methylene blue solution was irradiated with a 300 W Hg lamp equipped with a visible pass filter, an IR filter, and a cooling system. 0.5 ml of the methylene blue solution was periodically withdrawn and its absorbance was measured using a Varian Cary 5000 UV-vis-NIR spectrometer. The concentration ratio, C/C_0 was calculated using the intensity at 665 nm, which is the main absorption peak of methylene blue. C is the concentration of the methylene blue at each time and C_0 is the initial concentration of methylene blue.

7.3 Results

In the process of photocatalytic methylene blue degradation, it is necessary to reach the adsorption/desorption equilibrium in the dark before light irradiation. Times of 10 minutes to 2 hours have been used in previous work [187, 189-191]. However, we found that the even 2 hours is not sufficient to achieve equilibrium for the TiO_2-SWCNT aerogels since the aerogels have a high surface area. We put TiO_2-SWCNT aerogels into a 0.02 mM methylene blue solution and kept them in the dark for 24 hours, periodically withdrawing some solution to see how the concentration changes with time (see Figure 7.1 (a) and (b), at step i). In the dark, the concentration of methylene blue in solution decreased continuously, indicating that the TiO_2-SWCNT aerogels need much more time to equilibrate due to their high surface area. Under light irradiation in step ii) without dark equilibrium, the concentration of methylene blue solution decreased at the same rate in the dark for the first 1.5 h; however, the rate later increased implying the degradation of methylene blue has started to compete with to physical adsorption process.

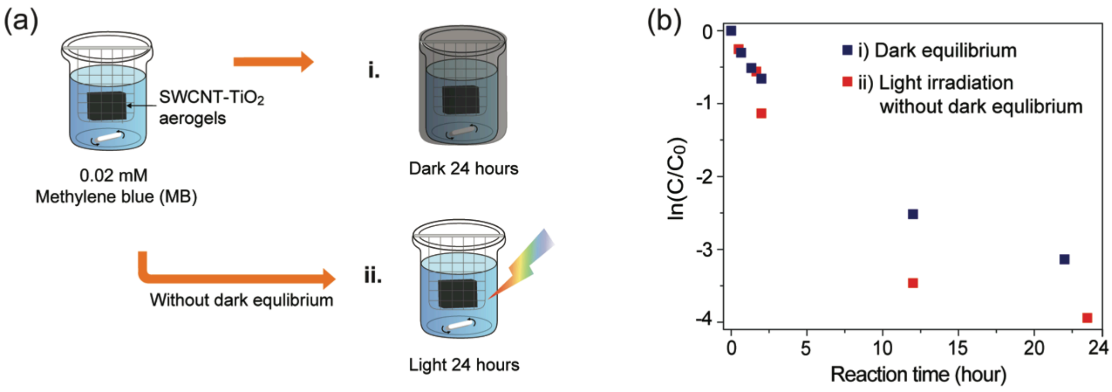

Figure 7.1 (a) Procedures of photocatalytic methylene blue degradation. i) Adsorption/desorption equilibrium in the dark for 24 hours. ii) Light irradiation (λ > 420 nm) without dark equilibrium for 24 hours. (b) Photocatalytic methylene blue degradation of step i) and ii).

Photocatalytic methylene blue degradation with TiO_2-SWCNT aerogels was conducted by using the remaining methylene blue solution under visible light as shown in Figure 7.2 (a) at step i). For comparison, we exchanged the remaining methylene blue with a new 0.02 mM methylene blue solution and conducted photocatalytic methylene blue degradation at step ii) and the results are shown in Figure 7.2 (b). The reaction rate can be accounted for by a pseudo-first-order model using the following equation.

$$\ln(C_0/C) = k_{app}t$$

C_0 is the initial dye concentration in the equation, C is the concentration of dye at time = t, k_{app} is the apparent first-order reaction rate, and t is the light exposure time. Based on the equation, the degradation rate, k, of step i) was 0.009/min which is six times higher than that of step ii), 0.0015/min. However, to precisely compare how many molecules of methylene blue were decomposed by unit mass of the photocatalyst per unit time, a unit of µmol/h/g was used in the work. The amount of methylene blue degraded per unit mass of photocatalyst per unit time of the both samples was the same and equal to 25 µmol/h/g.

In this chapter, since the SWCNTs could adsorb large amount of methylene blue molecules during adsorption-desorption equilibration, we assume C_0 is the concentration after the equilibration in the dark for 24 hours to calculate the degradation rate.

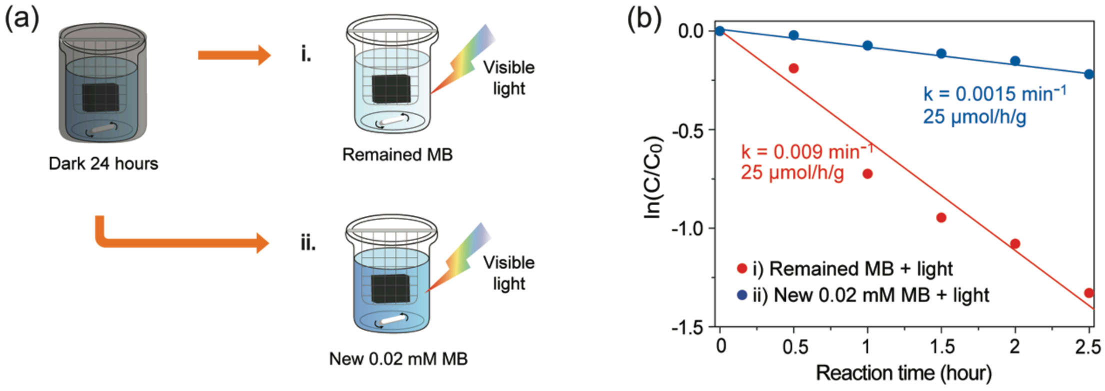

Figure 7.2 (a) Procedures for photocatalytic methylene blue degradation. i) Light irradiation with the remaining methylene blue solution after dark equilibrium for 24 hours. ii) Light irradiation with a new 0.02 mM methylene blue solution after dark equilibrium for 24 hours. (b) Photocatalytic methylene blue degradation for step i) and ii).

Photodegradation of methylene blue by TiO_2-SWCNT aerogels is compared to similar samples of blank (methylene blue), TiO_2 P25, and SWCNT aerogels in Figure 7.3. The blank sample and the reference TiO_2 P25 decomposed negligible amounts of methylene blue. The reaction rate for the pristine SWCNT aerogels was 0.0005/min and that of TiO_2-SWCNT aerogels was eighteen times higher, indicating significantly enhanced photo-catalytic activity.

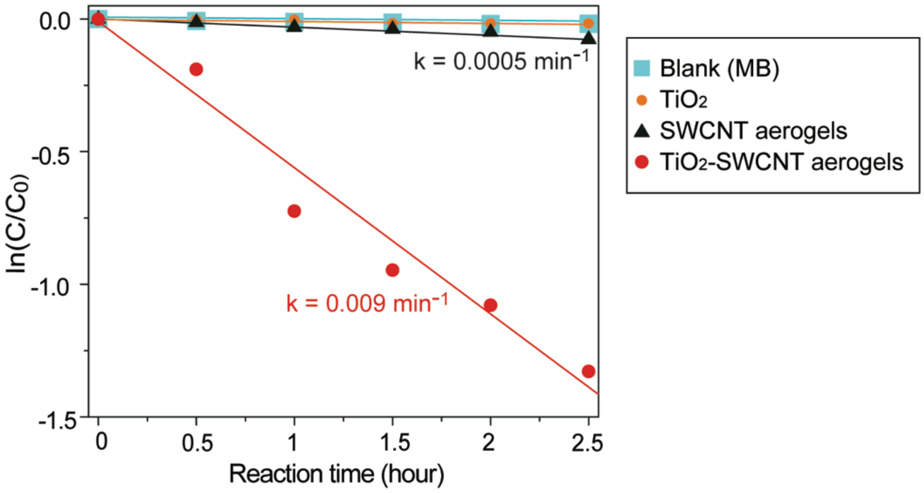

Figure 7.3 Photocatalytic methylene blue degradation of Blank (methylene blue), TiO_2, pristine SWCNT aerogels, and TiO_2-SWCNT aerogels under visible light irradiation ($\lambda > 420$ nm). The concentration change of methylene blue was calculated by comparison of absorbance intensity (C/C_0) at 665 nm.

To investigate how differences in the photocatalytic activity depend on the pyrolysis conditions, we compare TiO_2-SWCNT aerogels annealed in air with those annealed in argon (already shown in Figs. 7.1 to 7.3). Figure 7.4 (a) shows the photocatalytic degradation of methylene blue by TiO_2-SWCNT aerogels annealed in air and by TiO_2 P25 as a reference under ultraviolet light irradiation. For the results in this figure, we used 3 hours adsorption-desorption equilibration time before light irradiation. The results show that both are more active in UV light than in visible light. The methylene blue absorbance spectrum after different times of exposure to the TiO_2-SWCNT aerogels annealed in air shows a decrease in concentration of methylene blue every 20 minutes (Figure 7.4 (b)). Figure 7.4 (c) shows the photocatalytic degradation of methylene blue by SWCNT-TiO_2 aerogels annealed in air and TiO_2 P25 under visible light irradiation. Under visible light, both of them show negligible photocatalytic activity. Therefore, TiO_2-SWCNT aerogels annealed in argon have a higher photochemical activity than TiO_2-SWCNT aerogels annealed in air. The results imply that the microstructure or defect content of TiO_2 deposited on SWCNT aerogels has been changed by the annealing process, as also shown in the Raman spectroscopy, which leads to enhancement in visible light activity of TiO_2.

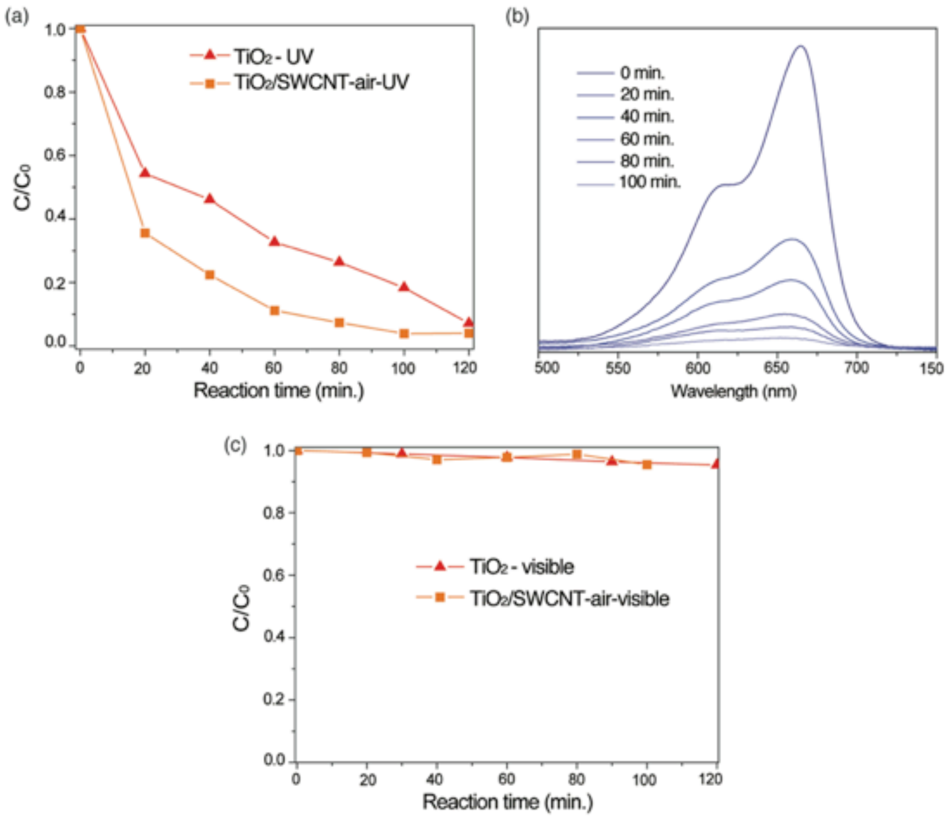

Figure 7.4 Photocatalytic methylene blue degradation by TiO_2-SWCNT aerogels annealed in air and TiO_2 P25. (a) Measurement under ultraviolet light. (b) Absorbance spectrum of methylene blue after different times of exposure to TiO_2-SWCNT aerogels. (c) Measurement under visible light.

To investigate the effect of cocatalysts, Pt nanoparticles were deposited on the TiO_2-SWCNT aerogels by chemical reduction and tested for photocatalytic degradation of methylene blue. We fabricated Pt-TiO_2-SWCNT aerogels (10 mM) and Pt-TiO_2-SWCNT aerogels (2 mM). TiO_2 was first deposited on the SWCNT aerogels followed by Pt deposition. Figure 7.5 shows the photodegradation of methylene blue by Pt-TiO_2-SWCNT aerogels under visible light irradiation. For the methylene blue degradation results in Figure 7.5 and 7.6, as well as 7.4, we used 3 hours for adsorption-desorption equilibration time and the results cannot be compared with those in Figure 7.1 - 7.3 which used 24 hours for the equilibration time. Moreover, we did not use a metal mesh to prevent an aerogels from collision with stir bar in contrast to previous experiments in Figure 7.1-7.3 that used a metal mesh.

The results in Figure 7.5 show that Pt-TiO_2-SWCNT aerogels have a lower photocatalytic reaction rate than pristine TiO_2-SWCNT aerogels. Pt-TiO_2-SWCNT aerogels synthesized by using 2 mM H_2PtCl_6 solution show a higher photocatalytic activity than those synthesized by using 10 mM H_2PtCl_6. However, in both cases the reactivity is less than was observed for the pristine TiO_2-SWCNT aerogels.

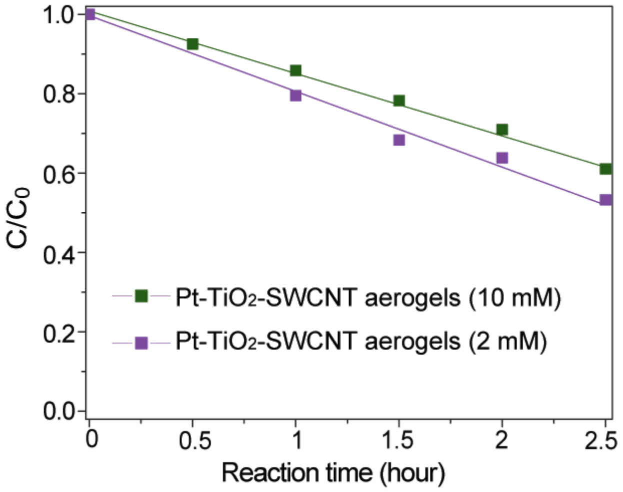

Figure 7.5 Photocatalytic methylene blue degradation of Pt-TiO_2-SWCNT aerogels with different concentration of Pt-precursor under visible light irradiation (λ > 420 nm). The Pt particles of Pt-TiO_2-SWCNT aerogels represented by the green squares were synthesized by using 10 mM H_2PtCl_6 solution and those represented by the purple squares were synthesized by using 2 mM H_2PtCl_6 solution.

We also fabricated TiO_2-Pt-SWCNT aerogels. To make the aerogels, Pt particles were first deposited on SWCNT aerogels followed by TiO_2 deposition. For the methylene blue degradation, we used the same condition with that of Pt-TiO_2-SWCNT aerogels such as 3 hours equilibration time without a metal mesh. Figure 7.6 shows the photo-degradation of methylene blue with TiO_2-Pt-SWCNT aerogels under visible light irradiation. TiO_2-Pt-SWCNT aerogels show similar reaction rate with that of TiO_2-SWCNT aerogels without Pt. From the results, the photocatalytic activity of the aerogels after Pt particles deposition was limited implying that the cathodic reaction in this system depends on SWCNTs, not additional cocatalysts loading. Thus, SWCNT aerogels in the hybrids act as cathodic sites that are good enough to make Pt unnecessary.

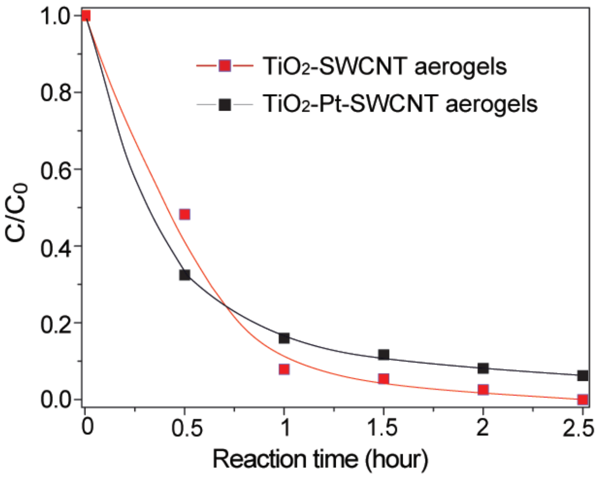

Figure 7.6 Photocatalytic methylene blue degradation of TiO_2-Pt-SWCNT aerogels under visible light irradiation.

7.5 Discussion

The photocatalytic activity of TiO_2-SWCNT aerogels was evaluated by measuring the rate of methylene blue degradation under visible light. The TiO_2-SWCNT aerogels degraded methylene blue significantly faster than pristine SWCNT aerogels and TiO_2 P25. The visible light photocatalytic activity of TiO_2-SWCNT aerogels could be explained by the experiment comparing sample pyrolyzed in Ar and air. TiO_2-SWCNT aerogels annealed in air have a higher photo-activity than TiO_2 P25 illuminated by a source that contains ultraviolet light. However, the photo-activity of TiO_2-SWCNT aerogels annealed in air was negligible under visible light. The result implies that TiO_2-SWCNT aerogels annealed in air have no activity under visible light since the TiO_2 in the TiO_2-SWCNT aerogels is acting as pristine TiO_2 without interaction with the carbon of the SWCNT aerogels. On the other hand, TiO_2-SWCNT aerogels annealed in argon have a higher activity under visible light, which indicates that the microstructure or defect structure of the TiO_2 can be changed by the pyrolysis conditions.

For the case of the TiO_2-SWCNT aerogels annealed in argon, in a low partial pressure of oxygen of the argon anneal, the TiO_2 that forms might be oxygen deficient and this may influence the interaction between the TiO_2 and SWCNTs. On the other hand, when TiO_2-SWCNT aerogels are annealed in air, amorphous TiO_2 transforms to stoichiometric anatase TiO_2 and appears to not interact as strongly with the SWCNT network. Thus, TiO_2-SWCNT aerogels annealed in argon show higher photocatalytic activity under visible light.

Since there have been reports that cocatalysts loading can enhance photocatalytic activity [34, 35], Pt nanoparticles were deposited on TiO_2-SWCNT aerogels to investigate the effect of a cocatalyst on photocatalytic activity. Pt-TiO_2-SWCNT aerogels were less active for the degradation of methylene blue than TiO_2-SWCNT aerogels without Pt under visible light. During chemical reduction, Pt nanoparticles could be randomly distributed on both TiO_2 and SWCNTs. Since SWCNTs are hydrophobic, it is possible that the Pt precursor and reducing agent contacted the TiO_2 nanoparticles more than SWCNTs. If so, it is possible that the majority of the Pt coated the TiO_2 nanoparticles. After light irradiation, most of the electrons transfer to the Pt nanoparticles located on TiO_2 rather than the SWCNTs. If so, the activity of the Pt-TiO_2-SWCNT aerogels should be similar to Pt-coated TiO_2 rather than TiO_2-SWCNT aerogels. Pt-TiO_2-SWCNT aerogels synthesized using 2 mM H_2PtCl_6 solution show higher photocatalytic activity than those synthesized using 10 mM H_2PtCl_6 solution. The result implies that the 10 mM Pt precursor makes more Pt particles on TiO_2 surfaces and this reduces the amount of light absorption. Even though the Pt-TiO_2-SWCNT aerogels synthesized using the 2 mM H_2PtCl_6 solution were a little more reactive than those synthesized with a higher concentration of Pt, both samples are much less active than pristine TiO_2-SWCNT aerogels.

TiO_2-Pt-SWCNT aerogels are less reactive for the photochemical degradation of methylene blue than TiO_2-SWCNT aerogels without Pt. The result implies added Pt additions do not improve the transfer of carriers from the TiO_2 to the SWCNT. The results from the Pt-TiO_2-SWCNT aerogels and the TiO_2-Pt-SWCNT aerogels suggest that SWCNT aerogels in the hybrids have sufficient cathodic sites and that Pt is not necessary. However, since the photocatalytic activity of the Pt loaded aerogels in Figure 7.5 and 7.6 were conducted after 3 hours adsorption-desorption equilibration time without using a metal mesh, and we need to conduct the experiments after 24 hours equilibration time with a metal mesh to precisely investigate how much dye molecules were decomposed under light and compare the data with those in Figure 7.1-7.3.

7.6 Conclusions

In summary, we developed TiO_2-SWCNT aerogels by uniformly distributing TiO_2 nanoparticles on individually dispersed SWCNT, Pt-TiO_2-SWCNT aerogels by depositing Pt particles on TiO_2-SWCNT aerogels, and TiO_2-Pt-SWCNT aerogels by depositing Pt particles on SWCNT aerogels followed by TiO_2 deposition. The SWCNT-TiO_2 aerogel degrades methylene blue in visible light faster than TiO_2 or SWCNTs alone. This is because of the high surface area and highly porous and stable network of the hybrid materials. Even after Pt particle deposition, TiO_2-SWCNT aerogels without Pt particles show higher photocatalytic activity than Pt coated aerogels, suggesting the potential utilization of the SWCNT aerogels as a substrate that provides cathodic sites and replaces noble metals in hybrid photocatalysts, solar cells, energy storage systems, and energy conversion systems.

Chapter 8

Conclusions

8.1 Conclusions

Microscopic images of TiO_2-CNT-Pt membranes showed well-aligned TiO_2-CNT-Pt tubes with 10 nm thick TiO_2, graphitic layers making up a carbon nanotube, and Pt nanoparticles within. Raman spectra of the TiO_2-CNT-Pt membranes showed a shifted TiO_2 E_g mode which indicates a stronger interaction between the TiO_2 and the CNTs. The photocatalytic activity of TiO_2-CNT-Pt for the photocatalytic degradation of methylene blue under visible light was significantly enhanced. The result is attributed to charge separation that reduces the recombination of e-h pairs and absorption of light in the visible region.

The locations of the oxidation and reduction sites were verified by photo-deposition of MnO_x and Ag. MnO_x was deposited on the outside of TiO_2-CNT-Pt and the Ag nanoparticles were deposited inside of TiO_2-CNT-Pt membrane. This experiment shows that the oxidation sites are on the outside of the TiO_2-CNT-Pt nanotubes and the reduction sites are within the TiO_2-CNT-Pt nanotubes. Moreover, the results demonstrate that the structure of the TiO_2-CNT-Pt membrane also has a high activity for the separation of oxidation and reduction species, hindering the back reaction of intermediates or final products. The unique design of the spatially separated channels keeps charge carriers and products from mixing each other. The inability of the TiO_2-CNT-Pt membrane to photodegrade methylene blue while sill on the AAO template is consistent with the assignment of the oxidation and reduction sites and indicates that there are a negligible number of pinholes between the TiO_2 and the CNTs.

The photoelectrochemical performance of the TiO_2-CNT-Pt membrane showed high photocurrent below 1.23 V RHE under both white and visible light. Even though pristine TiO_2 does not have any activity under visible light, the applied bias photon-to current efficiency (ABPE) of the TiO_2-CNT-Pt membrane is 1.45 % under white light and 0.83 % under visible light at 0.8 V versus RHE.

TiO_2-CNT membranes were synthesized with two different wall thicknesses, 10 nm and 50 nm. The 50 nm TiO_2-CNT membranes showed higher UV absorption than the 10 nm TiO_2-CNT membranes; however, thicker TiO_2 could not absorb more visible light. The photocatalytic activity of 10 nm TiO_2-CNT hybrids was greater than the 50 nm TiO_2-CNT hybrids for the photocatalytic degradation of methylene blue under visible light by hindering electron-hole recombination. For the experiments on the effect of bonding between TiO_2 and carbon, TiO_2-CNT-Pt-onestep showed higher photocatalytic activity than TiO_2-CNT-Pt-twostep under visible light. The lowest peak in the Raman spectrum, assigned to the E_g mode of anatase TiO_2, was shifted by 7 cm^{-1} compared with that of pristine TiO_2 and 4.5 cm^{-1} compared with that of the TiO_2-CNT-twostep, which implies that the TiO_2-CNT-onestep has more interaction between the TiO_2 and CNTs than that of the TiO_2-CNT-twostep. The photocatalytic activity of the TiO_2-CNT-Pt-onestep for the photocatalytic degradation of methylene blue under visible light was greater than that of the TiO_2-CNT-Pt-twostep, implying stronger bonding between the TiO_2 and carbon. The greater photochemical activity is related to the narrower bandgap that results when the TiO_2 and glucose are pyrolyzed together.

In chapter 6, TiO_2-SWCNT aerogels were developed with high surface area, fast charge separation, and stabile networks. In the synthesis process, SWCNT gel networks were prepared and then coated with TiO_2 using the sol-gel method. Scanning electron microscopy and transmission electron microscopy images showed that TiO_2-SWCNT aerogels had highly porous 3D networks of SWCNT aerogels with TiO_2 nanoparticles with a 9.3 nm average particle size. The Raman spectra of TiO_2-SWCNT aerogels series showed that the TiO_2 E_g mode of TiO_2-SWCNT aerogels was shifted by 6 cm^{-1}. There were negligible differences in the RBM mode, D-band, and G-band between the TiO_2-SWCNT aerogels and pristine SWCNT aerogels.

The TiO_2-SWCNT aerogels have a high specific surface area and porosity. In addition, the TiO_2-SWCNT aerogels were shown to be stable in water. The total volume change of the specimens after water contact was measured and the results showed that the volume of the SWCNT aerogels was significantly reduced after soaking in water while the volumes of the TiO_2-SWCNT aerogel series were reduced by a smaller amount, implying TiO_2 could help to maintain the networks of SWCNT aerogels. The photocatalytic degradation of methylene blue by the TiO_2-SWCNT aerogels was 25 μmol/h/g while the degradation of methylene blue by the TiO_2 P25 reference was negligible. Consequently, TiO_2 nanoparticles were distributed on well-dispersed SWCNT junctions, which causes high surface area and a stability of the networks in water. These characteristics of the TiO_2-SWCNT aerogels enhanced the photocatalytic activity under visible light irradiation.

TiO_2-SWCNT aerogels with added Pt particles are not more photochemically reactive than those without Pt. When the Pt is added after the TiO_2, the materials are less reactive than the Pt-free aerogels. When the Pt is added before the TiO_2, the materials are equally as reactive as the Pt-free aerogels. The results show that the SWCNTs themselves are effective cathodic sites and that Pt is not necessary. This suggests the potential utilization of the SWCNT aerogels as a substrate that provides cathodic sites and replaces noble metals in hybrid photocatalysts, solar cells, energy storage systems, and energy conversion systems.

8.2 Future direction

In chapter 5 and 6, the photochemical cell of TiO_2-CNT-Pt was discussed with various characterizations toward highly efficient photocatalytic and photoelectrochemical activity under visible light. In the Raman spectroscopy, even though the TiO_2-CNT-Pt shows obvious CNT peaks determined by D and G band, the intensity of D-band is still high, indicating there are plenty of sp^3 bondings caused by defects. Since the CNT was synthesized by using glucose as a carbon source and pyrolyzed at 600 °C to prohibit phase transformation of anatase TiO_2 to rutile, they are not perfect sp^2 bonded CNTs including many defects, which can be a trap site for recombination of charge carriers. To enhance photoactivity, it is necessary to synthesize better CNTs with less sp^3 bonding.

There are many strategies to make better CNTs and one of the methods is using hydrothermal treatment at a low temperature followed by a pyrolysis at a higher temperature. The reason why the CNT is not synthesized by hydrothermal treatment in the work is that the hydrothermal treatment could make firm graphitic layers on the top of the AAO template as well as inside of the template. As a result, the top of the AAO templates was covered by carbon aggregations hindering further deposition of Pt nanoparticles and more diffusion of dye molecules or water in performance test. To improve the limitations, it is necessary to find a proper way to scrap the surface of AAO templates after hydrothermal method. The pyrolysis temperature is also important to make graphitic layers and higher than 750 °C is required. In this work, 600 °C was chosen to synthesize anatase TiO_2 since higher pyrolysis temperature could make retile TiO_2 with larger particle size. However, if the quality of CNT is more important to get higher photocatalytic activity than TiO_2 phase, pyrolysis at higher temperature is a promising way to enhance the photocatalytic activity. Since there are various carbon sources, it would be an also good way to use different carbon sources to make better CNTs. In addition, alternative materials that can be annealed at a high temperature need to be developed to substitute TiO_2 in TiO_2-CNT-Pt system so that pyrolysis of carbon sources at a high temperature cannot affect the phase transformation of photocatalyst.

In the case of TiO_2-SWCNT aerogels at chapter 6 and 7, since the SWCNTs are pre-synthesized high purity SWCNTs and additional Pt coating does not affect enhancement of photocatalytic activity, we need to more focus on anodic side of the composite. Thus, it is desirable to study alternative photocatalysts to substitute TiO_2 to enhance photocatalytic activity under visible light.

References

1. Lehn, J.M., J.P. Sauvage, and R. Ziessel, *Photochemical Water Splitting Continuous Generation of Hydrogen and Oxygen by Irradiation of Aqueous Suspensions of Metal Loaded Strontium-Titanate.* Nouveau Journal De Chimie-New Journal of Chemistry, 1980. **4**(11): p. 623-627.
2. In, S., et al., *Effective visible light-activated B-Doped and B,N-Codoped TiO2 photocatalysts.* Journal of the American Chemical Society, 2007. **129**(45): p. 13790-+.
3. Fujishima, A., T.N. Rao, and D.A. Tryk, *TiO(2) photocatalysts and diamond electrodes.* Electrochimica Acta, 2000. **45**(28): p. 4683-4690.
4. Du, J., et al., *Hierarchically Ordered Macro-Mesoporous TiO2-Graphene Composite Films: Improved Mass Transfer, Reduced Charge Recombination, and Their Enhanced Photocatalytic Activities.* Acs Nano, 2011. **5**(1): p. 590-596.
5. Park, J.H., S. Kim, and A.J. Bard, *Novel carbon-doped TiO2 nanotube arrays with high aspect ratios for efficient solar water splitting.* Nano Letters, 2006. **6**(1): p. 24-28.
6. Liu, S.W., J.G. Yu, and M. Jaroniec, *Anatase TiO2 with Dominant High-Energy {001} Facets: Synthesis, Properties, and Applications.* Chemistry of Materials, 2011. **23**(18): p. 4085-4093.
7. Zheng, Q., et al., *Self-organized TiO2 nanotube array sensor for the determination of chemical oxygen demand.* Advanced Materials, 2008. **20**(5): p. 1044-+.
8. Roy, P., S. Berger, and P. Schmuki, *TiO2 Nanotubes: Synthesis and Applications.* Angewandte Chemie-International Edition, 2011. **50**(13): p. 2904-2939.
9. Yao, Y., et al., *Photoreactive TiO2/carbon nanotube composites: Synthesis and reactivity.* Environmental Science & Technology, 2008. **42**(13): p. 4952-4957.
10. Wang, M.Y., et al., *Inorganic-modified semiconductor TiO2 nanotube arrays for photocatalysis.* Energy & Environmental Science, 2014. **7**(7): p. 2182-2202.
11. Choi, W.Y., A. Termin, and M.R. Hoffmann, *The Role of Metal-Ion Dopants in Quantum-Sized Tio2 - Correlation between Photoreactivity and Charge-Carrier Recombination Dynamics.* Journal of Physical Chemistry, 1994. **98**(51): p. 13669-13679.
12. Zhao, L., et al., *One-Step Solvothermal Synthesis of a Carbon@TiO2 Dyade Structure Effectively Promoting Visible-Light Photocatalysis.* Advanced Materials, 2010. **22**(30): p. 3317-+.
13. Khan, S.U.M., M. Al-Shahry, and W.B. Ingler, *Efficient photochemical water splitting by a chemically modified n-TiO2 2.* Science, 2002. **297**(5590): p. 2243-2245.
14. Chen, D., et al., *Effects of boron doping on photocatalytic activity and microstructure of titanium dioxide nanoparticles.* Industrial & Engineering Chemistry Research, 2006. **45**(12): p. 4110-4116.
15. Li, D., et al., *Visible-light-driven photocatalysis on fluorine-doped TIO2 powders by the creation of surface oxygen vacancies.* Chemical Physics Letters, 2005. **401**(4-6): p. 579-584.
16. Ohno, T., et al., *Degradation of methylene blue on carbonate species-doped TiO2 photocatalysts under visible light.* Chemistry Letters, 2004. **33**(6): p. 750-751.
17. Long, M.C., et al., *Correlation of electronic structures and crystal structures with photocatalytic properties of undoped, N-doped and I-doped TiO2.* Chemical Physics Letters, 2006. **420**(1-3): p. 71-76.

18. Maeda, K. and K. Domen, *Photocatalytic Water Splitting: Recent Progress and Future Challenges.* Journal of Physical Chemistry Letters, 2010. **1**(18): p. 2655-2661.
19. Woan, K., G. Pyrgiotakis, and W. Sigmund, *Photocatalytic Carbon-Nanotube-TiO2 Composites.* Advanced Materials, 2009. **21**(21): p. 2233-2239.
20. Wen, Z.H., Q. Wang, and J.H. Li, *Template synthesis of aligned carbon nanotube arrays using glucose as a carbon source: Pt decoration of inner and outer nanotube surfaces for fuel-cell catalysts.* Advanced Functional Materials, 2008. **18**(6): p. 959-964.
21. Moisala, A., et al., *Thermal and electrical conductivity of single- and multi-walled carbon nanotube-epoxy composites.* Composites Science and Technology, 2006. **66**(10): p. 1285-1288.
22. Kim, K.H., Y. Oh, and M.F. Islam, *Mechanical and Thermal Management Characteristics of Ultrahigh Surface Area Single-Walled Carbon Nanotube Aerogels.* Advanced Functional Materials, 2013. **23**(3): p. 377-383.
23. Martel, R., et al., *Single- and multi-wall carbon nanotube field-effect transistors.* Applied Physics Letters, 1998. **73**(17): p. 2447-2449.
24. Islam, M.F., et al., *High weight fraction surfactant solubilization of single-wall carbon nanotubes in water.* Nano Letters, 2003. **3**(2): p. 269-273.
25. Bryning, M.B., et al., *Carbon nanotube aerogels.* Advanced Materials, 2007. **19**(5): p. 661-+.
26. Fujishima, A. and K. Honda, *Electrochemical Photolysis of Water at a Semiconductor Electrode.* Nature, 1972. **238**(5358): p. 37-+.
27. Sato, S. and J.M. White, *Photo-Decomposition of Water over P-Tio2 Catalysts.* Chemical Physics Letters, 1980. **72**(1): p. 83-86.
28. Domen, K., et al., *Photocatalytic Decomposition of Water-Vapor on an Nio-Srtio3 Catalyst.* Journal of the Chemical Society-Chemical Communications, 1980(12): p. 543-544.
29. Chen, X.B., et al., *Semiconductor-based Photocatalytic Hydrogen Generation.* Chemical Reviews, 2010. **110**(11): p. 6503-6570.
30. Kudo, A. and Y. Miseki, *Heterogeneous photocatalyst materials for water splitting.* Chemical Society Reviews, 2009. **38**(1): p. 253-278.
31. Maeda, K., *Photocatalytic water splitting using semiconductor particles: History and recent developments.* Journal of Photochemistry and Photobiology C-Photochemistry Reviews, 2011. **12**(4): p. 237-268.
32. Chen, H.M., et al., *Nano-architecture and material designs for water splitting photoelectrodes.* Chemical Society Reviews, 2012. **41**(17): p. 5654-5671.
33. Wang, C.C., Z.B. Zhang, and J.Y. Ying, *Photocatalytic decomposition of halogenated organics over nanocrystalline titania.* Nanostructured Materials, 1997. **9**(1-8): p. 583-586.
34. Anpo, M. and M. Takeuchi, *The design and development of highly reactive titanium oxide photocatalysts operating under visible light irradiation.* Journal of Catalysis, 2003. **216**(1-2): p. 505-516.
35. Ni, M., et al., *A review and recent developments in photocatalytic water-splitting using TiO2 for hydrogen production.* Renewable & Sustainable Energy Reviews, 2007. **11**(3): p. 401-425.
36. Wu, N.L. and M.S. Lee, *Enhanced TiO2 photocatalysis by Cu in hydrogen production from aqueous methanol solution.* International Journal of Hydrogen Energy, 2004. **29**(15): p. 1601-1605.
37. Li, F.B. and X.Z. Li, *The enhancement of photodegradation efficiency using Pt-TiO2 catalyst.* Chemosphere, 2002. **48**(10): p. 1103-1111.
38. Subramanian, V., E.E. Wolf, and P.V. Kamat, *Catalysis with TiO2/gold nanocomposites. Effect of metal particle size on the Fermi level equilibration.* Journal of the American Chemical Society, 2004. **126**(15): p. 4943-4950.
39. Nowotny, J., et al., *Solar-hydrogen: Environmentally safe fuel for the future.* International Journal of Hydrogen Energy, 2005. **30**(5): p. 521-544.

40. Bard, A.J. and M.A. Fox, *Artificial Photosynthesis - Solar Splitting of Water to Hydrogen and Oxygen.* Accounts of Chemical Research, 1995. **28**(3): p. 141-145.
41. Walter, M.G., et al., *Solar Water Splitting Cells.* Chemical Reviews, 2010. **110**(11): p. 6446-6473.
42. Kocha, S.S., et al., *Photoelectrochemical decomposition of water utilizing monolithic tandem cells.* Solar Energy Materials and Solar Cells, 1998. **52**(3-4): p. 389-397.
43. Khaselev, O., A. Bansal, and J.A. Turner, *High-efficiency integrated multijunction photovoltaic/electrolysis systems for hydrogen production.* International Journal of Hydrogen Energy, 2001. **26**(2): p. 127-132.
44. Licht, S., et al., *Over 18% solar energy conversion to generation of hydrogen fuel; theory and experiment for efficient solar water splitting (Reprinted from J. Phys. Chem. B, vol 104, pg 8920-8924, 2000).* International Journal of Hydrogen Energy, 2001. **26**(7): p. 653-659.
45. Gratzel, M., *Photoelectrochemical cells.* Nature, 2001. **414**(6861): p. 338-344.
46. Cesar, I., et al., *Translucent thin film Fe2O3 photoanodes for efficient water splitting by sunlight: Nanostructure-directing effect of Si-doping.* Journal of the American Chemical Society, 2006. **128**(14): p. 4582-4583.
47. Bolton, J.R., S.J. Strickler, and J.S. Connolly, *Limiting and Realizable Efficiencies of Solar Photolysis of Water.* Nature, 1985. **316**(6028): p. 495-500.
48. Turner, J.A., *A realizable renewable energy future.* Science, 1999. **285**(5428): p. 687-689.
49. Reece, S.Y., et al., *Wireless Solar Water Splitting Using Silicon-Based Semiconductors and Earth-Abundant Catalysts.* Science, 2011. **334**(6056): p. 645-648.
50. Wolcott, A., et al., *Photoelectrochemical Water Splitting Using Dense and Aligned TiO2 Nanorod Arrays.* Small, 2009. **5**(1): p. 104-111.
51. Liu, M.Z., N.D. Snapp, and H. Park, *Water photolysis with a cross-linked titanium dioxide nanowire anode.* Chemical Science, 2011. **2**(1): p. 80-87.
52. Mor, G.K., et al., *Enhanced photocleavage of water using titania nanotube arrays.* Nano Letters, 2005. **5**(1): p. 191-195.
53. Paulose, M., et al., *Anodic growth of highly ordered TiO2 nanotube arrays to 134 mu m in length.* Journal of Physical Chemistry B, 2006. **110**(33): p. 16179-16184.
54. Hartmann, P., et al., *Mesoporous TiO2: Comparison of Classical Sol-Gel and Nanoparticle Based Photoelectrodes for the Water Splitting Reaction.* Acs Nano, 2010. **4**(6): p. 3147-3154.
55. Chakrapani, V., J. Thangala, and M.K. Sunkara, *WO3 and W2N nanowire arrays for photoelectrochemical hydrogen production.* International Journal of Hydrogen Energy, 2009. **34**(22): p. 9050-9059.
56. Alexander, B.D., et al., *Metal oxide photoanodes for solar hydrogen production.* Journal of Materials Chemistry, 2008. **18**(20): p. 2298-2303.
57. Sivula, K., et al., *Photoelectrochemical Water Splitting with Mesoporous Hematite Prepared by a Solution-Based Colloidal Approach.* Journal of the American Chemical Society, 2010. **132**(21): p. 7436-7444.
58. Le Formal, F., M. Gratzel, and K. Sivula, *Controlling Photoactivity in Ultrathin Hematite Films for Solar Water-Splitting.* Advanced Functional Materials, 2010. **20**(7): p. 1099-1107.
59. Morrish, R., et al., *Activation of Hematite Nanorod Arrays for Photoelectrochemical Water Splitting.* Chemsuschem, 2011. **4**(4): p. 474-479.
60. Berglund, S.P., et al., *Photoelectrochemical Oxidation of Water Using Nanostructured BiVO4 Films.* Journal of Physical Chemistry C, 2011. **115**(9): p. 3794-3802.
61. Cristino, V., et al., *Efficient Photoelectrochemical Water Splitting by Anodically Grown WO3 Electrodes.* Langmuir, 2011. **27**(11): p. 7276-7284.
62. Su, J.Z., et al., *Vertically Aligned WO3 Nanowire Arrays Grown Directly on Transparent Conducting Oxide Coated Glass: Synthesis and Photoelectrochemical Properties.* Nano Letters, 2011. **11**(1): p. 203-208.

63. Mohapatra, S.K., et al., *Water Photooxidation by Smooth and Ultrathin alpha-Fe2O3 Nanotube Arrays.* Chemistry of Materials, 2009. **21**(14): p. 3048-3055.
64. Duret, A. and M. Gratzel, *Visible light-induced water oxidation on mesoscopic alpha-Fe2O3 films made by ultrasonic spray pyrolysis.* Journal of Physical Chemistry B, 2005. **109**(36): p. 17184-17191.
65. Su, J.Z., et al., *Aqueous Growth of Pyramidal-Shaped BiVO4 Nanowire Arrays and Structural Characterization: Application to Photoelectrochemical Water Splitting.* Crystal Growth & Design, 2010. **10**(2): p. 856-861.
66. Houas, A., et al., *Photocatalytic degradation pathway of methylene blue in water.* Applied Catalysis B-Environmental, 2001. **31**(2): p. 145-157.
67. Konstantinou, I.K. and T.A. Albanis, *TiO2-assisted photocatalytic degradation of azo dyes in aqueous solution: kinetic and mechanistic investigations - A review.* Applied Catalysis B-Environmental, 2004. **49**(1): p. 1-14.
68. Al-Degs, Y., et al., *Effect of carbon surface chemistry on the removal of reactive dyes from textile effluent.* Water Research, 2000. **34**(3): p. 927-935.
69. Meshko, V., et al., *Adsorption of basic dyes on granular acivated carbon and natural zeolite.* Water Research, 2001. **35**(14): p. 3357-3366.
70. Zhang, F.L., et al., *TiO2-assisted photodegradation of dye pollutants - II. Adsorption and degradation kinetics of eosin in TiO2 dispersions under visible light irradiation.* Applied Catalysis B-Environmental, 1998. **15**(1-2): p. 147-156.
71. Hoffmann, M.R., et al., *Environmental Applications of Semiconductor Photocatalysis.* Chemical Reviews, 1995. **95**(1): p. 69-96.
72. Obata, H., K. Kogasaka, and M. Koizumi, *Photochemical Reactions between Methylene Blue and Trimethylamine, Dimethylamine and Monomethylamine .3. The Behavior of Methylene Blue in the Presence of Oxygen.* Bulletin of the Chemical Society of Japan, 1959. **32**(2): p. 125-132.
73. Prevot, A.B., et al., *Photocatalytic degradation of acid Blue 80 in aqueous solutions containing TiO(2) suspensions.* Environmental Science & Technology, 2001. **35**(5): p. 971-976.
74. Tanaka, K., K. Padermpole, and T. Hisanaga, *Photocatalytic degradation of commercial azo dyes.* Water Research, 2000. **34**(1): p. 327-333.
75. Daneshvar, N., D. Salari, and A.R. Khataee, *Photocatalytic degradation of azo dye acid red 14 in water: investigation of the effect of operational parameters.* Journal of Photochemistry and Photobiology a-Chemistry, 2003. **157**(1): p. 111-116.
76. Liu, Y., et al., *Substrate-free, large-scale, free-standing and two-side oriented single crystal TiO2 nanorod array films with photocatalytic properties.* Chemical Communications, 2011. **47**(13): p. 3790-3792.
77. Wu, H.B., H.H. Hng, and X.W. Lou, *Direct Synthesis of Anatase TiO2 Nanowires with Enhanced Photocatalytic Activity.* Advanced Materials, 2012. **24**(19): p. 2567-2571.
78. Pan, J.H., et al., *Self-etching reconstruction of hierarchically mesoporous F-TiO(2) hollow microspherical photocatalyst for concurrent membrane water Purifications.* Journal of the American Chemical Society, 2008. **130**(34): p. 11256-+.
79. Zhang, Z.H., et al., *Plasmonic Gold Nanocrystals Coupled with Photonic Crystal Seamlessly on TiO2 Nanotube Photoelectrodes for Efficient Visible Light Photoelectrochemical Water Splitting.* Nano Letters, 2013. **13**(1): p. 14-20.
80. Karakitsou, K.E. and X.E. Verykios, *Effects of Altervalent Cation Doping of Tio2 on Its Performance as a Photocatalyst for Water Cleavage.* Journal of Physical Chemistry, 1993. **97**(6): p. 1184-1189.
81. Tada, H. and M. Tanaka, *Dependence of TiO2 photocatalytic activity upon its film thickness.* Langmuir, 1997. **13**(2): p. 360-364.
82. Rivera, A.P., K. Tanaka, and T. Hisanaga, *Photocatalytic Degradation of Pollutant over Tio2 in Different Crystal-Structures.* Applied Catalysis B-Environmental, 1993. **3**(1): p. 37-44.

83. Ding, Z., G.Q. Lu, and P.F. Greenfield, *Role of the crystallite phase of TiO(2) in heterogeneous photocatalysis for phenol oxidation in water.* Journal of Physical Chemistry B, 2000. **104**(19): p. 4815-4820.
84. Zhu, J.F., et al., *Characterization of Fe-TiO2 photocatalysts synthesized by hydrothermal method and their photocatalytic reactivity for photodegradation of XRG dye diluted in water.* Journal of Molecular Catalysis a-Chemical, 2004. **216**(1): p. 35-43.
85. Carp, O., C.L. Huisman, and A. Reller, *Photoinduced reactivity of titanium dioxide.* Progress in Solid State Chemistry, 2004. **32**(1-2): p. 33-177.
86. Augustynski, J., *The Role of the Surface Intermediates in the Photoelectrochemical Behavior of Anatase and Rutile Tio2.* Electrochimica Acta, 1993. **38**(1): p. 43-46.
87. Zhang, J., et al., *Importance of the relationship between surface phases and photocatalytic activity of TiO2.* Angewandte Chemie-International Edition, 2008. **47**(9): p. 1766-1769.
88. Chen, X.B. and C. Burda, *The electronic origin of the visible-light absorption properties of C-, N- and S-doped TiO2 nanomaterials.* Journal of the American Chemical Society, 2008. **130**(15): p. 5018-+.
89. Liu, G., et al., *Synergistic effects of B/N doping on the visible-light photocatalytic activity of mesoporous TiO2 (vol 47, pg 4516, 2008).* Angewandte Chemie-International Edition, 2008. **47**(29): p. 5277-5277.
90. Choi, J., H. Park, and M.R. Hoffmann, *Effects of Single Metal-Ion Doping on the Visible-Light Photoreactivity of TiO2.* Journal of Physical Chemistry C, 2010. **114**(2): p. 783-792.
91. Cowan, A.J., et al., *Water Splitting by Nanocrystalline TiO2 in a Complete Photoelectrochemical Cell Exhibits Efficiencies Limited by Charge Recombination.* Journal of Physical Chemistry C, 2010. **114**(9): p. 4208-4214.
92. Yang, X., et al., *Highly visible-light active C- and V-doped TiO2 for degradation of acetaldehyde.* Journal of Catalysis, 2007. **252**(2): p. 296-302.
93. Tachikawa, T., et al., *Photocatalytic oxidation reactivity of holes in the sulfur- and carbon-doped TiO(2) powders studied by time-resolved diffuse reflectance spectroscopy.* Journal of Physical Chemistry B, 2004. **108**(50): p. 19299-19306.
94. Asahi, R., et al., *Visible-light photocatalysis in nitrogen-doped titanium oxides.* Science, 2001. **293**(5528): p. 269-271.
95. Gole, J.L., et al., *Highly efficient formation of visible light tunable TiO2-xNx photocatalysts and their transformation at the nanoscale.* Journal of Physical Chemistry B, 2004. **108**(4): p. 1230-1240.
96. Mrowetz, M., et al., *Oxidative power of nitrogen-doped TiO2 photocatalysts under visible illumination.* Journal of Physical Chemistry B, 2004. **108**(45): p. 17269-17273.
97. Umebayashi, T., et al., *Visible light-induced degradation of methylene blue on S-doped TiO2.* Chemistry Letters, 2003. **32**(4): p. 330-331.
98. Wang, Y., et al., *A highly efficient visible-light-activated photocatalyst based on bismuth- and sulfur-codoped TiO(2).* Journal of Physical Chemistry C, 2008. **112**(17): p. 6620-6626.
99. Iketani, K., et al., *Sol-gel-derived VxTi1-xO2 films and their photocatalytic activities under visible light irradiation.* Materials Science and Engineering B-Solid State Materials for Advanced Technology, 2004. **108**(3): p. 187-193.
100. Klosek, S. and D. Raftery, *Visible light driven V-doped TiO2 photocatalyst and its photooxidation of ethanol.* Journal of Physical Chemistry B, 2001. **105**(14): p. 2815-2819.
101. Borgarello, E., et al., *Visible-Light Induced Water Cleavage in Colloidal Solutions of Chromium-Doped Titanium-Dioxide Particles.* Journal of the American Chemical Society, 1982. **104**(11): p. 2996-3002.
102. Anpo, M., et al., *Design and development of unique titanium oxide photocatalysts capable of operating under visible light irradiation by an advanced metal ion-*

implantation method. Science and Technology in Catalysis 1998, 1999. **121**: p. 305-310.

103. Pan, C.C. and J.C.S. Wu, *Visible-light response Cr-doped TiO2-N-X(X) photocatalysts.* Materials Chemistry and Physics, 2006. **100**(1): p. 102-107.
104. Niishiro, R., H. Kato, and A. Kudo, *Nickel and either tantalum or niobium-codoped TiO2 and SrTiO3 photocatalysts with visible-light response for H-2 or O-2 evolution from aqueous solutions.* Physical Chemistry Chemical Physics, 2005. **7**(10): p. 2241-2245.
105. Kim, D.H., et al., *Photocatalytic activity of Ni 8 wt%-doped TiO2 photocatalyst synthesized by mechanical alloying under visible light.* Journal of the American Ceramic Society, 2006. **89**(2): p. 515-518.
106. Zhang, X.W. and L.C. Lei, *One step preparation of visible-light responsive Fe-TiO2 coating photocatalysts by MOCVD.* Materials Letters, 2008. **62**(6-7): p. 895-897.
107. Nahar, S., K. Hasegawa, and S. Kagaya, *Photocatalytic degradation of phenol by visible light-responsive iron-doped TiO2 and spontaneous sedimentation of the TiO2 particles.* Chemosphere, 2006. **65**(11): p. 1976-1982.
108. Zhu, J.F., et al., *Fe(3+)-TiO(2) photocatalysts prepared by combining sol-gel method with hydrothermal treatment and their characterization.* Journal of Photochemistry and Photobiology a-Chemistry, 2006. **180**(1-2): p. 196-204.
109. Litter, M.I., *Heterogeneous photocatalysis - Transition metal ions in photocatalytic systems.* Applied Catalysis B-Environmental, 1999. **23**(2-3): p. 89-114.
110. Dvoranova, D., et al., *Investigations of metal-doped titanium dioxide photocatalysts.* Applied Catalysis B-Environmental, 2002. **37**(2): p. 91-105.
111. Hameed, A., M.A. Gondal, and Z.H. Yamani, *Effect of transition metal doping on photocatalytic activity of WO3 for water splitting under laser illumination: role of 3d-orbitals.* Catalysis Communications, 2004. **5**(11): p. 715-719.
112. Xu, A.W., Y. Gao, and H.Q. Liu, *The preparation, characterization, and their photocatalytic activities of rare-earth-doped TiO2 nanoparticles.* Journal of Catalysis, 2002. **207**(2): p. 151-157.
113. Di Paola, A., et al., *Preparation of polycrystalline TiO(2) photocatalysts impregnated with various transition metal ions: Characterization and photocatalytic activity for the degradation of 4-nitrophenol.* Journal of Physical Chemistry B, 2002. **106**(3): p. 637-645.
114. Wilke, K. and H.D. Breuer, *The influence of transition metal doping on the physical and photocatalytic properties of titania.* Journal of Photochemistry and Photobiology a-Chemistry, 1999. **121**(1): p. 49-53.
115. Xu, J.C., et al., *Doping metal ions only onto the catalyst surface.* Journal of Molecular Catalysis a-Chemical, 2004. **219**(2): p. 351-355.
116. Peng, S.Q., et al., *Effect of Be2+ doping TiO2 on its photocatalytic activity.* Chemical Physics Letters, 2004. **398**(1-3): p. 235-239.
117. Umebayashi, T., et al., *Band gap narrowing of titanium dioxide by sulfur doping.* Applied Physics Letters, 2002. **81**(3): p. 454-456.
118. Okada, M., et al., *Fabrication of multifunctional coating which combines low-e property and visible-light-responsive photocatalytic activity.* Thin Solid Films, 2003. **442**(1-2): p. 217-221.
119. Chen, S.Z., et al., *Investigation of nitrogen doped TiO2 photocatalytic films prepared by reactive magnetron sputtering.* Catalysis Communications, 2004. **5**(11): p. 677-680.
120. Hattori, A., et al., *A promoting effect of NH4F addition on the photocatalytic activity of sol-gel TiO2 films.* Chemistry Letters, 1998(8): p. 707-708.
121. Lindgren, T., et al., *Photoelectrochemical and optical properties of nitrogen doped titanium dioxide films prepared by reactive DC magnetron sputtering.* Journal of Physical Chemistry B, 2003. **107**(24): p. 5709-5716.
122. Torres, G.R., et al., *Photoelectrochemical study of nitrogen-doped titanium dioxide for water oxidation.* Journal of Physical Chemistry B, 2004. **108**(19): p. 5995-6003.

123. Tanguay, J.F., S.L. Suib, and R.W. Coughlin, *Dichloromethane Photodegradation Using Titanium Catalysts.* Journal of Catalysis, 1989. **117**(2): p. 335-347.
124. Matos, J., J. Laine, and J.M. Herrmann, *Synergy effect in the photocatalytic degradation of phenol on a suspended mixture of titania and activated carbon.* Applied Catalysis B-Environmental, 1998. **18**(3-4): p. 281-291.
125. Yang, N.L., et al., *Photocatalytic Properties of Graphdiyne and Graphene Modified TiO2: From Theory to Experiment.* Acs Nano, 2013. **7**(2): p. 1504-1512.
126. Kongkanand, A., R.M. Dominguez, and P.V. Kamat, *Single wall carbon nanotube scaffolds for photoelectrochemical solar cells. Capture and transport of photogenerated electrons.* Nano Letters, 2007. **7**(3): p. 676-680.
127. Cui, G.W., et al., *Rational design of carbon and TiO2 assembly materials: covered or strewn, which is better for photocatalysis?* Chemical Communications, 2013. **49**(57): p. 6415-6417.
128. Li, G.H. and K.A. Gray, *The solid-solid interface: Explaining the high and unique photocatalytic reactivity of TiO2-based nanocomposite materials.* Chemical Physics, 2007. **339**(1-3): p. 173-187.
129. Iijima, S., *Helical Microtubules of Graphitic Carbon.* Nature, 1991. **354**(6348): p. 56-58.
130. Coleman, J.N., et al., *Small but strong: A review of the mechanical properties of carbon nanotube-polymer composites.* Carbon, 2006. **44**(9): p. 1624-1652.
131. Bachtold, A., et al., *Logic circuits with carbon nanotube transistors.* Science, 2001. **294**(5545): p. 1317-1320.
132. Derycke, V., et al., *Carbon nanotube inter- and intramolecular logic gates.* Nano Letters, 2001. **1**(9): p. 453-456.
133. Cheung, C.L., et al., *Growth and fabrication with single-walled carbon nanotube probe microscopy tips.* Applied Physics Letters, 2000. **76**(21): p. 3136-3138.
134. Wilson, N.R., D.H. Cobden, and J.V. Macpherson, *Single-wall carbon nanotube conducting probe tips.* Journal of Physical Chemistry B, 2002. **106**(51): p. 13102-13105.
135. Akita, S., et al., *Carbon nanotube tips for a scanning probe microscope: their fabrication and properties.* Journal of Physics D-Applied Physics, 1999. **32**(9): p. 1044-1048.
136. Yenilmez, E., et al., *Wafer scale production of carbon nanotube scanning probe tips for atomic force microscopy.* Applied Physics Letters, 2002. **80**(12): p. 2225-2227.
137. Wise, K.E., et al., *Stable dispersion of single wall carbon nanotubes in polyimide: the role of noncovalent interactions.* Chemical Physics Letters, 2004. **391**(4-6): p. 207-211.
138. Bokobza, L., *Multiwall carbon nanotube elastomeric composites: A review.* Polymer, 2007. **48**(17): p. 4907-4920.
139. Iijima, S. and T. Ichihashi, *Single-Shell Carbon Nanotubes of 1-Nm Diameter.* Nature, 1993. **363**(6430): p. 603-605.
140. Dresselhaus, M.S., G. Dresselhaus, and R. Saito, *Carbon-Fibers Based on C-60 and Their Symmetry.* Physical Review B, 1992. **45**(11): p. 6234-6242.
141. Jang, S.R., R. Vittal, and K.J. Kim, *Incorporation of functionalized single-wall carbon nanotubes in dye-sensitized TiO2 solar cells.* Langmuir, 2004. **20**(22): p. 9807-9810.
142. Kongkanand, A. and P.V. Kamat, *Electron storage in single wall carbon nanotubes. Fermi level equilibration in semiconductor-SWCNT suspensions.* Acs Nano, 2007. **1**(1): p. 13-21.
143. Wang, W.D., et al., *Visible light photodegradation of phenol on MWNT-TiO2 composite catalysts prepared by a modified sol-gel method.* Journal of Molecular Catalysis a-Chemical, 2005. **235**(1-2): p. 194-199.
144. Ou, Y., et al., *MWNT-TiO2 : Ni composite catalyst: A new class of catalyst for photocatalytic H-2 evolution from water under visible light illumination.* Chemical Physics Letters, 2006. **429**(1-3): p. 199-203.

145. Gao, S.J., et al., *Photoinduced Superwetting Single-Walled Carbon Nanotube/TiO2 Ultrathin Network Films for Ultrafast Separation of Oil-in-Water Emulsions.* Acs Nano, 2014. **8**(6): p. 6344-6352.
146. Dang, X.N., et al., *Virus-templated self-assembled single-walled carbon nanotubes for highly efficient electron collection in photovoltaic devices.* Nature Nanotechnology, 2011. **6**(6): p. 377-384.
147. Yu, Y., et al., *Enhancement of adsorption and photocatalytic activity of TiO2 by using carbon nanotubes for the treatment of azo dye.* Applied Catalysis B-Environmental, 2005. **61**(1-2): p. 1-11.
148. Yu, Y., et al., *Enhancement of photocatalytic activity of mesoporous TiO2 by using carbon nanotubes.* Applied Catalysis a-General, 2005. **289**(2): p. 186-196.
149. Hutchison, J.L., et al., *Double-walled carbon nanotubes fabricated by a hydrogen arc discharge method.* Carbon, 2001. **39**(5): p. 761-770.
150. Saito, Y., T. Nakahira, and S. Uemura, *Growth conditions of double-walled carbon nanotubes in arc discharge.* Journal of Physical Chemistry B, 2003. **107**(4): p. 931-934.
151. Hiraoka, T., et al., *Selective synthesis of double-wall carbon nanotubes by CCVD of acetylene using zeolite supports.* Chemical Physics Letters, 2003. **382**(5-6): p. 679-685.
152. Darabont, A., et al., *Synthesis of carbon nanotubes by spray pyrolysis and their investigation by electron microscopy.* Journal of Optoelectronics and Advanced Materials, 2005. **7**(2): p. 631-636.
153. Bronikowski, M.J., et al., *Gas-phase production of carbon single-walled nanotubes from carbon monoxide via the HiPco process: A parametric study.* Journal of Vacuum Science & Technology A, 2001. **19**(4): p. 1800-1805.
154. Resasco, D.E., et al., *A scalable process for production of single-walled carbon nanotubes (SWNTs) by catalytic disproportionation of CO on a solid catalyst.* Journal of Nanoparticle Research, 2002. **4**(1-2): p. 131-136.
155. Zhang, Y. and S. Iijima, *Formation of single-wall carbon nanotubes by laser ablation of fullerenes at low temperature.* Applied Physics Letters, 1999. **75**(20): p. 3087-3089.
156. Scott, C.D., et al., *Growth mechanisms for single-wall carbon nanotubes in a laser-ablation process.* Applied Physics a-Materials Science & Processing, 2001. **72**(5): p. 573-580.
157. Falco, C., et al., *Hydrothermal Carbon from Biomass: Structural Differences between Hydrothermal and Pyrolyzed Carbons via C-13 Solid State NMR.* Langmuir, 2011. **27**(23): p. 14460-14471.
158. Sun, Z., et al., *Growth of Graphene from Solid Carbon Sources.* Nature, 2010. **468**: p. 549-552.
159. Subramanian, V., E. Wolf, and P.V. Kamat, *Semiconductor-metal composite nanostructures. To what extent do metal nanoparticles improve the photocatalytic activity of TiO2 films?* Journal of Physical Chemistry B, 2001. **105**(46): p. 11439-11446.
160. Jin, S. and F. Shiraishi, *Photocatalytic activities enhanced for decompositions of organic compounds over metal-photodepositing titanium dioxide.* Chemical Engineering Journal, 2004. **97**(2-3): p. 203-211.
161. Subramanian, V., E. Wolf, and P.V. Kamat, *Semiconductor-metal composite nanostructures. To what extent do metal nanoparticles improve the photocatalytic activity of TiO2 films?* Journal of Physical Chemistry B, 2001. **105**(46): p. 11439-11446.
162. Jakob, M., H. Levanon, and P.V. Kamat, *Charge distribution between UV-irradiated TiO(2) and gold nanoparticles: Determination of shift in the Fermi level.* Nano Letters, 2003. **3**(3): p. 353-358.

163. Tseng, I.H., W.C. Chang, and J.C.S. Wu, *Photoreduction of CO2 using sol-gel derived titania and titania-supported copper catalysts.* Applied Catalysis B-Environmental, 2002. **37**(1): p. 37-48.
164. Liu, S.X., et al., *A mechanism for enhanced photocatalytic activity of silver-loaded titanium dioxide.* Catalysis Today, 2004. **93-5**: p. 877-884.
165. Szabo-Bardos, E., H. Czili, and A. Horvath, *Photocatalytic oxidation of oxalic acid enhanced by silver deposition on a TiO2 surface.* Journal of Photochemistry and Photobiology a-Chemistry, 2003. **154**(2-3): p. 195-201.
166. Selli, E., et al., *A photocatalytic water splitting device for separate hydrogen and oxygen evolution.* Chemical Communications, 2007(47): p. 5022-5024.
167. Subramanian, V., E.E. Wolf, and P.V. Kamat, *Green emission to probe photoinduced charging events in ZnO-Au nanoparticles. Charge distribution and fermi-level equilibration.* Journal of Physical Chemistry B, 2003. **107**(30): p. 7479-7485.
168. Sakkas, V.A., et al., *Metolachlor photocatalytic degradation using TiO2 photocatalysts.* Applied Catalysis B-Environmental, 2004. **49**(3): p. 195-205.
169. Kitano, M., et al., *Photocatalytic water splitting using Pt-loaded visible light-responsive TiO2 thin film photocatalysts.* Catalysis Today, 2007. **120**(2): p. 133-138.
170. Matsuoka, M., et al., *Photocatalysis for new energy production - Recent advances in photocatalytic water splitting reactions for hydrogen production.* Catalysis Today, 2007. **122**(1-2): p. 51-61.
171. Hou, Y.D., et al., *Bioinspired molecular co-catalysts bonded to a silicon photocathode for solar hydrogen evolution.* Nature Materials, 2011. **10**(6): p. 434-438.
172. Munprom, R., P.A. Salvador, and G.S. Rohrer, *Polar Domains at the Surface of Centrosymmetric BiVO4.* Chemistry of Materials, 2014. **26**(9): p. 2774-2776.
173. Li, R.G., et al., *Spatial separation of photogenerated electrons and holes among {010} and {110} crystal facets of BiVO4.* Nature Communications, 2013. **4**.
174. Chu, S.Z., et al., *Synthesis and characterization of titania nanostructures on glass by Al anodization and sol-gel process.* Chemistry of Materials, 2002. **14**(1): p. 266-272.
175. Kang, T.S., et al., *Fabrication of Highly-Ordered TiO2 Nanotube Arrays and Their Use in Dye-Sensitized Solar Cells.* Nano Letters, 2009. **9**(2): p. 601-606.
176. Kyotani, T., B.K. Pradhan, and A. Tomita, *Synthesis of carbon nanotube composites in nanochannels of an anodic aluminum oxide film.* Bulletin of the Chemical Society of Japan, 1999. **72**(9): p. 1957-1970.
177. Brunauer, S., P.H. Emmett, and E. Teller, *Adsorption of gases in multimolecular layers.* Journal of the American Chemical Society, 1938. **60**: p. 309-319.
178. Bethune, D.S., et al., *Cobalt-Catalyzed Growth of Carbon Nanotubes with Single-Atomic-Layerwalls.* Nature, 1993. **363**(6430): p. 605-607.
179. Wang, X.C., et al., *Photocatalytic activity of a hierarchically macro/mesoporous titania.* Langmuir, 2005. **21**(6): p. 2552-2559.
180. Yang, Y.D., et al., *Electrophoresis coating of titanium dioxide on aligned carbon nanotubes for controlled syntheses of photoelectronic nanomaterials.* Advanced Materials, 2007. **19**(9): p. 1239-+.
181. Banerjee, S. and S.S. Wong, *Synthesis and characterization of carbon nanotube-nanocrystal heterostructures.* Nano Letters, 2002. **2**(3): p. 195-200.
182. Leary, R. and A. Westwood, *Carbonaceous nanomaterials for the enhancement of TiO2 photocatalysis.* Carbon, 2011. **49**(3): p. 741-772.
183. Zhang, Y.H., et al., *TiO2-Graphene Nanocomposites for Gas-Phase Photocatalytic Degradation of Volatile Aromatic Pollutant: Is TiO2-Graphene Truly Different from Other TiO2-Carbon Composite Materials?* Acs Nano, 2010. **4**(12): p. 7303-7314.
184. Elmalem, E., et al., *Growth of Photocatalytic CdSe-Pt Nanorods and Nanonets.* Advanced Materials, 2008. **20**(22): p. 4312-4317.
185. Soni, S.S., et al., *Visible-light photocatalysis in titania-based mesoporous thin films.* Advanced Materials, 2008. **20**(8): p. 1493-+.

186. An, C.H., S.N. Peng, and Y.G. Sun, *Facile Synthesis of Sunlight-Driven AgCl:Ag Plasmonic Nanophotocatalyst.* Advanced Materials, 2010. **22**(23): p. 2570-2574.
187. Lee, J.S., K.H. You, and C.B. Park, *Highly Photoactive, Low Bandgap TiO2 Nanoparticles Wrapped by Graphene.* Advanced Materials, 2012. **24**(8): p. 1084-1088.
188. Xing, M.Y., X. Li, and J.L. Zhang, *Synergistic effect on the visible light activity of Ti3+ doped TiO2 nanorods/boron doped graphene composite.* Scientific Reports, 2014. **4**.
189. Zhang, H., et al., *P25-Graphene Composite as a High Performance Photocatalyst.* Acs Nano, 2010. **4**(1): p. 380-386.
190. Long, M.C., et al., *Origin of Visible Light Photoactivity of Reduced Graphene Oxide/TiO2 by in Situ Hydrothermal Growth of Undergrown TiO2 with Graphene Oxide.* Journal of Physical Chemistry C, 2013. **117**(32): p. 16734-16741.
191. Chen, W., et al., *Enhanced Visible-Light Activity of Titania via Confinement inside Carbon Nanotubes.* Journal of the American Chemical Society, 2011. **133**(38): p. 14896-14899.
192. Yonemoto, B.T., G.S. Hutchings, and F. Jiao, *A General Synthetic Approach for Ordered Mesoporous Metal Sulfides.* Journal of the American Chemical Society, 2014. **136**(25): p. 8895-8898.
193. Gomez-Navarro, C., et al., *Electronic transport properties of individual chemically reduced graphene oxide sheets.* Nano Letters, 2007. **7**(11): p. 3499-3503.
194. Bersani, D., P.P. Lottici, and X.Z. Ding, *Phonon confinement effects in the Raman scattering by TiO2 nanocrystals.* Applied Physics Letters, 1998. **72**(1): p. 73-75.
195. Parker, J.C. and R.W. Siegel, *Calibration of the Raman-Spectrum to the Oxygen Stoichiometry of Nanophase Tio2.* Applied Physics Letters, 1990. **57**(9): p. 943-945.
196. Zhang, Z.B., et al., *Role of particle size in nanocrystalline TiO2-based photocatalysts.* Journal of Physical Chemistry B, 1998. **102**(52): p. 10871-10878.
197. Peigney, A., et al., *Specific surface area of carbon nanotubes and bundles of carbon nanotubes.* Carbon, 2001. **39**(4): p. 507-514.
198. Ebbesen, T.W., et al., *Electrical conductivity of individual carbon nanotubes.* Nature, 1996. **382**(6586): p. 54-56.
199. Berber, S., Y.K. Kwon, and D. Tomanek, *Unusually high thermal conductivity of carbon nanotubes.* Physical Review Letters, 2000. **84**(20): p. 4613-4616.
200. Treacy, M.M.J., T.W. Ebbesen, and J.M. Gibson, *Exceptionally high Young's modulus observed for individual carbon nanotubes.* Nature, 1996. **381**(6584): p. 678-680.
201. Kim, K.H., M. Vural, and M.F. Islam, *Single-Walled Carbon Nanotube Aerogel-Based Elastic Conductors.* Advanced Materials, 2011. **23**(25): p. 2865-+.
202. Brantley, S.L. and N.P. Mellott, *Surface area and porosity of primary silicate minerals.* American Mineralogist, 2000. **85**(11-12): p. 1767-1783.
203. Cinke, M., et al., *Pore structure of raw and purified HiPco single-walled carbon nanotubes.* Chemical Physics Letters, 2002. **365**(1-2): p. 69-74.